Unravelling the Electronic and Magnetic Properties of Quantum Materials: From Metal-Organic Frameworks to Frustrated Magnets

By

ANDREA ILICETO

A thesis submitted to
the University of Birmingham
for the degree of
DOCTOR OF PHILOSOPHY

A. J. Morris Group
School of Metallurgy and Materials
College of Engineering and Physical Sciences
University of Birmingham
September 2023

ABSTRACT

Quantum materials are expected to be the future of technology, with emerging IT relying on new materials capable of switchable and stimuli-responsive behaviour. Quantum mechanics governs the physical nature of all materials, able to describe how atoms and electrons behave and interact. At the macroscopic level, quantum effects are not normally visible and the system can be approximated by a classical description, however, in quantum materials, these effects remain noticeable and manifest over a large range of energy and length scales. This work presents a density-functional theory (DFT) study on two promising quantum materials: $CrCl_2(pym)$ $[pym = pyrimidine]$ and $Cu_4(OH)_6FBr$, candidate structures to host the S=2 Haldane phase and the quantum spin liquid phase respectively. This research also aims at the discovery of new quantum materials via structure prediction of $CrCl_2(pydz)$ $[pydz = pyridazine]$.

DFT struggles to account for the strong electron correlations found in quantum materials and, therefore, a Hubbard U correction is needed. Such an approach has been first applied to study the low-dimensional metal–organic magnet $CrCl_2(pym)$. DFT+U (U = 3 eV) geometry optimisation results found the presence of a Jahn-Teller distortion, confirming a Cr^{2+} oxidation state with crystal field splitting resulting in S = 2. Band-structure and density of states calculations showed a band gap of 1.2 eV. Despite $CrCl_2(pym)$ approaching the quasi-one-dimensional antiferromagnet limit with a magnetic exchange ratio $J_1/J_2 = 8.4$, the Haldane phase was not confirmed by experimental collaborators, most likely suppressed by superexchange interactions or single ion anisotropy.

Another focus of this work is the investigation of the quantum spin liquid candidate barlowite $[Cu_4(OH)_6FBr]$. Despite barlowite having an adequately small spin of $S = \frac{1}{2}$ to be a quantum spin liquid, such a quantum phase was not found, although non-collinear DFT calculations confirmed the frustrated magnetic nature of the system. Structural disorder is present in the system; DFT+U (U = 5 eV) geometry optimisations relaxed the system in

the $Pnma$ and $P6_3/mmc$ space groups. Band-structure calculations found a band gap of 0.56 eV, and a similar insulating nature was found for analogues containing different halides, namely claringbullite $[Cu_4(OH)_6FCl]$ and iodide $[Cu_4(OH)_6FI]$.

Building on the techniques fine tuned in modelling the systems presented above, a search for novel quantum materials was carried out starting from $CrCl_2(pym)$ in which Cr was exchanged with a series of transition metals (V, Fe, Co, Ni) to create new systems, discover trends and test for their properties. Furthermore, the search was expanded to include a different organic ligand, pyridazine. The novel $CrCl_2(pydz)$ structure was discovered by carrying out structure searching by means of the Wyckoff Alignment of Molecules (WAM) technique. Magnetic exchange results show that this material is quasi-one-dimensional, with $J_1/J_2 = 16.92$. This is a promising result, suggesting that the DFT tested requirements to host the S = 2 Haldane phase are met and this structure is ready to be physically synthesised and experimentally proven.

ACKNOWLEDGEMENTS

During my journey as a PhD student, I had the privilege of working with many amazing people, some of whom I would like to thank here. First and foremost, I would like to thank my supervisor, Andrew Morris, who has guided me throughout my research and has always been supportive and helpful in overcoming challenges. I would also like to express my sincere gratitude to Matthew Cliffe from the University of Nottingham and his PhD student Jem Pitcairn for their experimental contribution to this work, with whom I have published my first journal article. Furthermore, I would like to thank Lucy Clark from the department of Chemistry at the University of Birmingham for introducing me to the world of quantum spin liquids and for collaborating in my research.

On a separate note, I thank the School of Metallurgy and Materials for the welcoming work environment and the various members of the Morris group who helped me throughout my PhD, especially Wataru Sekine, Hrishit Banerjee, Jordan Dorrell, Chris Owen and Mario Ongkiko. I am also grateful to the CASTEP community for all their support and the c2x software developer Michael Rutter.

In addition, I would like to thank the Engineering and Physical Sciences Research Council (EPSRC) for their financial support throughout the years, as well as Sulis and BlueBEAR HPC platforms for their generous allocation of resources which have been used for the DFT calculations presented in this thesis.

Lastly, I would like to give a sincere thank you to my family for all their support and encouragement throughout all my studies, as well as to all the special people who have been dear to me during my PhD: despite distances often being far you have always made me feel close.

Contents

List of Figures

List of Tables

Chapter One

Introduction and Scientific Background

1.1 Overview

Modern technology is significantly driven by advances in engineering, materials applications and software development, driven by our current understanding of the world at the atomic level. One promising class of materials with innovative technological applications are quantum materials. Quantum materials are a class of materials in which quantum effects remain noticeable and manifest over a large range of energy and length scales, at times even at the macroscopic level. A classical description of such materials would not account for the various properties they exhibit, as their nature can only be described using quantum mechanics. Examples of quantum materials include superconductors, qubits, and quantum sensors [1].

One of the most common types of quantum materials are strongly correlated materials, which exhibit quantum mechanical properties driven by the strong electron-electron interactions. Quantum materials have opened the door to exotic states of matter, from topological insulators to quantum spin liquids [2]. Interesting magnetic properties often arise with such quantum materials, opening up a world of technological potential [3].

This thesis explores two of these exotic states, namely the Haldane phase using metal-organic magnets and the quantum spin liquid phase using minerals. This is a computational research using density-functional theory (DFT), a computational quantum mechanical modelling method. In this chapter, the scientific background relevant to this work is presented, along with an explanation of the motivation and research scope. Chapter two explains how DFT works and its applications relevant to the modelling of quantum materials. In chapter three, a DFT exploration of the Haldane phase candidate metal-organic framework $CrCl_2(pym)\,[pym = pyrimidine]$ is presented. In chapter four, the quantum spin liquid candidate Barlowite is studied to investigate its structural nature, electronic properties and magnetic frustrations. In chapter five, the understanding of the systems previously explored and the refined modelling approaches developed throughout this research are exploited to search for new quantum materials. A set of new 2D Metal-organic magnets based on the structure presented in chapter three have been investigated. The last chapter comprises of a summary of the work carried out along with an outlook on future developments.

1.2 Scientific background

The science governing the materials explored in this thesis is a combination of materials science, solid state physics and materials chemistry. Quantum mechanics forms the scientific basis of this work, and is at the core of the material properties explored as well as the computational approach used to study them.

1.2.1 Quantum materials: strongly correlated systems

Quantum materials are a class of compounds characterised by strong electron-electron interactions. Electron correlations govern the properties of these materials, and theories omitting this correlation interaction, such as Hartree-Fock theory, give qualitatively incorrect results. This class of materials showing strong interactions between electrons often include ions with narrow localised d or f open shells. The d or f orbitals are more localised and have a smaller volume than s or p orbitals, causing these electrons to be relatively closer to one another and experience strong Coulombic repulsion [4]. The crystal structure of these materials results in narrow bands stemming from these orbitals. Simple band-theory models are inadequate to describe these materials and often give wrong predictions in terms of electrical conductivity. Alternative models, such as the Hubbard model presented in chapter 2, have been developed to describe these materials, in which there is a competition between the on-site Coulomb interaction with electron delocalisation [5].

Strongly correlated materials can be classified under different families. The most common includes $4f$ and $5f$ electron compounds, showing either Kondo or heavy fermion behaviour. Fermionic quasi-particles, much heavier than the ones found in conventional metals, are often hosted by this family of materials. This family often exhibits non-Fermi liquid behaviour, and act as unconventional superconductors under low temperatures [6]. Examples include UPt_3, $CeAl_3$ and $YbRh_2Si_2$ [7, 8].

The second family of strongly correlated materials includes systems with partially filled d orbitals, such as many 3d, 4d and 5d compounds. High-temperature superconducting cuprates are the classic example, and other examples include manganites, titanates and ruthenates such as $LaMnO_3$, $LaTiO_3$ and Sr_2RuO_4 [9]. This class of materials exhibit, to different degrees, Mott behaviour. Mott insulators [10] are a class of materials that are expected to conduct but actually show insulating behaviours. These materials possess half-filled bands and, even when exposed to an electric field, are unable to conduct due to strong electron-electron interactions. The on site Coulombic repulsion between electrons is stronger than the “hopping” kinetic energy that would cause the electrons to conduct, so the electrons stay “pinned” in place and conduction does not take place. In addition to Mott behaviour, this class of correlated materials can also present spin and orbital frustration, such as in the quantum spin-liquid materials explored in chapter 4.

A third family of strongly correlated materials includes molecular crystals, such as C_{60} compounds, characterised by small inter-molecular hopping integrals resulting in narrow bands [11].

In real-world strongly correlated systems, multiple strongly correlated bands often coexist, which compete with other interactions besides the on-site Coulomb repulsion, such as electron–lattice coupling, crystal-field splitting, spin–orbit interaction, or magnetic exchange. It is therefore hard to pinpoint the real cause of an experimentally observed phenomenon due to the interplay of these interactions, especially when the correlation is strong. For instance, a conductive to insulator transition may be expected to arise from a Mott mechanism, but it could also be caused by lattice distortions reducing the symmetry, or both [4]. Computational simulations are the best tool scientists can deploy in such scenarios in order to disentangle the complexity of the system.

One famous example which scientists pondered for many years is the case of single layered ruthenates. It was unknown if the ordering arises from a purely electronic many-body super-exchange mechanism or if it arises from the electron–lattice interaction. It was recently discovered that such ordering arises from the interplay of super-exchange with Born–Mayer repulsion [12].

It is therefore clear that strongly correlated materials are a complex field of material science, not defined by a single observable quantity, but rather consisting of a class of materials in which the local Coulomb interaction must be explicitly taken into account, coherent with the Hubbard model. It is conclusive to consider the d and f orbitals electrons to play a fundamental role in strongly correlated materials, and in the next section we will explore their nature inside a crystal by looking at crystal field theory.

1.2.2 Crystal field theory

The materials presented in this research combine transition metals with ligands in a crystal setting. In this section, we will describe what happens to transition metal complexes due to the presence of such ligands.

From the moment we position an atom in a crystal and it forms bonds, there is a large number of Coulombic and magnetic interactions it experiences from adjacent atoms. The outer electrons are the ones responsible for forming bonds and giving the atom its magnetic moment. For simplicity, let us consider point charges with the classical Coulomb's interaction energy between the charges:

$$E \propto \frac{q_1 q_2}{r} \tag{1.1}$$

In transition metals, the d-orbital electrons play a major role in terms of the electronic and magnetic properties of the atom and these electrons interact strongly with adjacent atoms. The 3d orbitals have an Azimuthal quantum number $l = 2$ (d-orbitals) with magnetic quantum numbers m_l = -2, -1, 0, 1, 2 (in the $d_{z^2}, d_{x^2-y^2}, d_{xy}, d_{xz}, d_{yz}$ orientations).

For an isolated atom, these 3d orbitals are degenerate in energy. As we move inside a crystal, repulsion between the electrons in the d-orbitals and the ligands breaks the degeneracy. As shown in figure 1.1, the 3d orbitals are not spherically symmetrical, some lie on the x,y,z axes, like the d_{z^2} and $d_{x^2-y^2}$ orbitals, while others are in between the axes [13]. Therefore, some of the 3d orbitals point towards the ligands while others do not, meaning that some d-electrons will experience more opposition from the ligands than others, depending upon the geometry of the crystal. This is the reason why the degeneracy is broken, causing a splitting in the energy levels, known as crystal field splitting. The representation of this splitting is shown for a crystal with an octahedral geometry in figure 1.2.

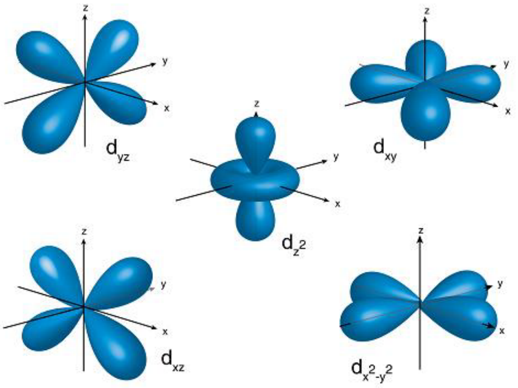

Figure 1.1: Schematic representation of the d-orbital shapes of an isolated hydrogen atom. The orbitals are a good representation of the probability of finding electrons in a given point in space, and 5 of them exist for the d-shell electrons. Figure from Chemistrytalk.org[14]

.

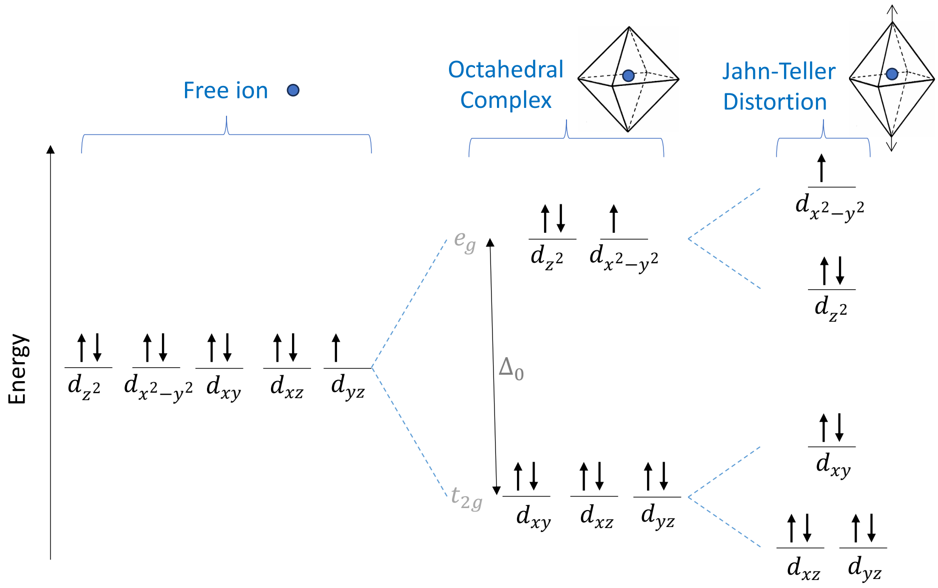

Figure 1.2: Schematic representation of the crystal field splitting in an octahedral complex and Jahn-Teller distortion. The orbitals that lie on the axis (e_g) point towards the ligands and are raised in energy, whereas the others t_{2g} are lowered in energy. The Jahn-Teller distortion for a 9 d-electron octahedral system results in a further decrease in degeneracy.

Electrons are filled following an arrangement which minimises the energy of the system. This means that in a crystal field, the first 3 electrons fill up the t_{2g} shells. The fourth electron can either fill up one of the e_g shells or pair with one of the t_{2g} electrons with opposite spin. The pairing with one of the previously half-filled t_{2g} costs energy, the spin pairing energy. If the crystal field splitting energy Δ_0 is more than the spin pairing energy, then the electron will fill up the t_{2g} shell, resulting in the "low spin" configuration, as is the case for strong-field ligands. On the other hand, if the crystal field splitting energy Δ_0 is rather small, less than the spin pairing energy, then the electron will fill up the e_g shell, resulting in the "high spin" configuration, as is the case for weak-field ligands [15]. A diagram summarising the high and low spin configurations is presented in figure 1.3. If these d-electrons are arranged in the e_g and t_{2g} d-orbitals in a non-symmetrical fashion, as depicted by the blue coloured configurations in figure 1.3, the system will experience a geometrical distortion, known as the Jahn-Teller distortion.

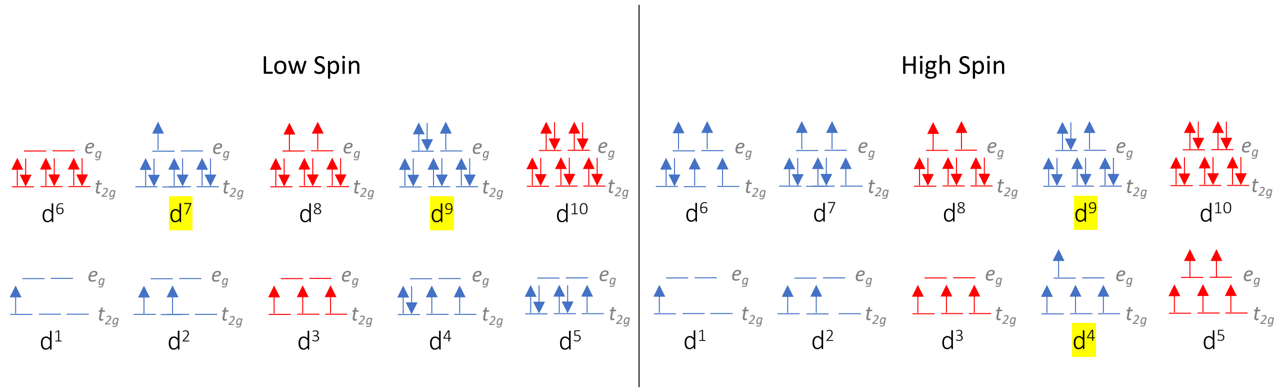

Figure 1.3: Representation of the d-orbitals of an octahedral complex undergoing crystal field splitting. Jahn-Teller distortion occurs when these d-orbitals are filled in a non-symmetrical manner. The symmetrical configurations have been shown in red, whereas the non-symmetrical ones in blue. The configurations with an asymmetrically filled e_g orbital are the ones experiencing the strongest Jahn-Teller distortion and have been highlighted in yellow.

1.2.3 The Jahn-Teller effect

The Jahn-Teller effect, common to octahedral complexes, is a geometric distortion of a non-linear molecular system that reduces its symmetry and energy. This results in unequally occupied orbitals being no longer degenerate, lowering the overall energy of the complex [16]. This therefore happens when the d-orbitals are not filled symmetrically.

The Jahn-Teller effects therefore cause the physical geometry of the system to stretch or compress. As this happens, the e_g and t_{2g} electrons are no longer degenerate. The new relative energies of these orbitals are shown in figure 1.2. When asymmetry is present in the t_{2g} orbital the Jahn-Teller effect will cause a weak distortion, whereas in the presence of e_g asymmetry, the Jahn-Teller effect will cause a strong distortion.

As the metal ion is placed in the crystal, the metal's orbitals overlap with the ligand's orbitals to form molecular orbitals. As ligand field theory predicts, some of the resulting covalent bonds will be of lower energy than the original atomic orbitals, called the bonding molecular orbitals; some will be of higher energy, the anti-bonding molecular orbitals; and some will be of the same energy, the non-bonding molecular orbitals [17].

The transition metals in many of these octahedral complex systems, and generally in strongly correlated materials, have partially filled d shells with unpaired electrons. These unpaired electrons, having angular momentum, result in the atom having an overall magnetic moment pointing in a specific direction. This leads to magnetic behaviours, which we will explore in the next section.

1.2.4 Magnetism in solids

Magnetism classically arises from the motion of electric charges, such as by a flow of electrons around a coil. With the development of quantum mechanics, it has been discovered that charged particles like electrons have an intrinsic spin angular momentum (μ_e), giving rise to a magnetic moment, meaning that each electron acts as a minuscule bar magnet [18].

The spin angular momentum of an electron around a nucleus is:

$$\mu_e = -\frac{e\hbar}{2m_e} \tag{1.2}$$

in which e is the electric charge of the electron and m_e is its mass. The magnitude of μ_e is referred to as a Bohr magneton (μ_B), which is often used as the unit for expressing the magnetic moment of an electron.

Furthermore, the electron "orbits" around a nucleus with orbital angular momentum $\vec{L}$, giving rise to a magnetic moment $\vec{\mu} = \gamma\vec{L}$, where γ is the gyromagnetic ratio. The combination of these, along with a very small contribution from the nucleus, results in the net magnetic moment of an atom.

For an electron around a nucleus, the magnitudes of orbital and spin angular momentum are quantised in terms of the spin (s) and orbital (l) angular momentum quantum numbers as follows:

$$\begin{aligned} |\vec{L}| &= \sqrt{l(l+1)}\hbar \\ |\vec{S}| &= \sqrt{s(s+1)}\hbar \end{aligned} \tag{1.3}$$

Note that $s = \frac{1}{2}$ and $l = 0, 1, 2, 3 ... n-1$ where n is the principal quantum number. Recall that l, sometimes referred to as the Azimuthal quantum number, is what is commonly used to describe the shapes of the orbitals of an electron orbiting a nucleus, such as the s,p,d or f orbital shapes.

The orbital and spin angular momentum are further quantised in different directions, depending upon the magnetic quantum number (m_l) and the spin quantum number ($m_s = \pm\frac{1}{2}$). Recall that (m_l) determines how many orbitals there are, of a given type, per energy level. For instance, for l=1 (p-orbitals) m_l = -1, 0, 1 (in the Px, Py, Pz orientations).

The sum of the spin angular momentum and orbital angular momentum results in the total angular momentum $\vec{J} = \vec{L} + \vec{S}$. The total magnetic dipole moment is [19]

$$\vec{\mu_j} = g_{\mathrm{J}}\, \mu_B\, \frac{\vec{J}}{\hbar} \tag{1.4}$$

where g_{J} is the Landé g-factor, a measure of the relative importance of orbital and spin angular momenta. This gives rise to the total effective magnetic moment of an atom, which is quantised quantity as follows:

$$|\mu_{\mathrm{eff}}| = g_{\mathrm{J}} \sqrt{J(J+1)}\, \mu_B \tag{1.5}$$

In spite of this, the orbital angular momentum does not substantially contribute to the magnetic field of an atom. The electrons in any filled shell move equally in any given direction and can be pictured to have a “cancelling out” effect in terms of the effective magnetic moment, on top of the fact that they come in spin up and spin down pairs. The majority of the effective magnetic moment in an atom therefore arises from the unpaired electrons in half-filled outer shells [18]. This is why atoms found near the sides of the periodic table with mostly filled electron shells are not magnetic, whereas the atoms towards the middle of the blocks, such as transition metals with half-filled electron shells, exhibit strong magnetic behaviour.

After having understood magnetism on a single-atom basis, we are ready to explore what happens when we combine atoms in crystal structures and understand how magnets are formed. Following the logic presented in the previous chapter, one might expect solids made up of atoms with unpaired electrons in half-filled outer shells to be magnetic, however, the magnetisation of the entire sample is usually zero. This is because different regions within the material normally have their magnetic moments pointing in different directions. These regions are called domains, and inside each domain the magnetic moments actually do point in a uniform direction. To magnetise a sample of material, an external magnetic field ($\vec{H}$) is applied. The domains aligned with this external field will grow, shrinking the adjacent domain which are not aligned in order to minimise the overall energy of the system. Once the magnetic moments of the atoms in the sample are aligned with the external magnetic field, the sample is magnetised. Some materials are easier to magnetise than others, which is dictated by the magnetic susceptibility of the material χ. The magnetisation ($\vec{M}$) is

$$\vec{M} = \chi \vec{H} \tag{1.6}$$

In ferromagnetic materials the uniform magnetic moment arrangement is stable and a magnet is formed, whereas in paramagnetic materials the magnetisation is not permanent and will dissipate once the external magnetic field is removed. Despite ferromagnetic materials, such as iron, acting as permanent magnets, they can lose their magnetisation due to an increase in temperature. Thermal energy causes the atoms to vibrate more and misalign, decreasing the magnetisation while increasing the internal entropy of the system. The temperature above which certain materials lose their permanent magnetic properties and undergo a phase change is known as Curie temperature for ferromagnetic materials and Néel temperature for anti-ferromagnetic materials [20]. Notice that as we transition from a non-magnetic state to a magnetic one in which the spins are aligned, the rotational symmetry of the system is broken during this phase transition. Whether a material acts as a ferromagnet, anti-ferromagnet or paramagnet is dependent upon the magnetic exchange interactions, which will be explored in the next section.

1.2.5 Magnetic exchange

The exchange interaction is a quantum mechanical phenomenon whereby individual magnetic moments will attempt to align all other magnetic moments of the system with themselves. This means that if the exchange interaction between the electron spins is larger than the thermal energy of the atoms involved, then ferromagnetism is seen, and the opposite case if for para-magnetism [21].

To understand magnetic exchange, let us first remind ourselves of the Pauli exclusion principle, which states that two identical fermions cannot occupy the same quantum state simultaneously. The wavefunction describing two electrons in the same quantum system may have the same spatial part or the same spin component, but not both. To understand this, let us take two particles with positions $\vec{r}_1$ and $\vec{r}_2$ occupying two different quantum states Ψ_A and Ψ_B respectively. The combined wavefunction solution for this system can be represented as $\Psi(\vec{r}_1, \vec{r}_2) = \Psi_A(\vec{r}_1)\,\Psi_B(\vec{r}_2)$. After the exchange of the two particles is carried out, we find $\Psi(\vec{r}_1, \vec{r}_2) = \Psi_A(\vec{r}_2)\,\Psi_B(\vec{r}_1)$. The probability distribution is identical before and after the exchange, being $|\Psi(\vec{r}_1, \vec{r}_2)|^2 = |\Psi(\vec{r}_2, \vec{r}_1)|^2$, which means that $\Psi(\vec{r}_1, \vec{r}_2) = \pm\Psi(\vec{r}_2, \vec{r}_1)$. This gives rise to two distinct classes of subatomic particles which show different behaviours under exchange: bosons, whose wavefunctions are symmetrical under exchange $\Psi(\vec{r}_1, \vec{r}_2) = \Psi(\vec{r}_2, \vec{r}_1)$, and fermions, whose wavefunctions are anti-symmetrical under exchange $\Psi(\vec{r}_1, \vec{r}_2) = -\Psi(\vec{r}_2, \vec{r}_1)$. Electrons are fermions, and the wavefunction of electrons is therefore always anti-symmetric, either having symmetrical spatial components and anti-symmetrical spins (in anti-ferromagnets), or anti-symmetrical spatial component and symmetrical spins (in ferromagnets) [22]. The wave function overlap of two electrons gives rise to the exchange integral J. The exchange energy between all the neighbouring magnetic moments of a system can be quantified using the Heisenberg model [23]:

$$\hat{H} = -J \sum_{ij} \vec{S}_i \cdot \vec{S}_j \tag{1.7}$$

where $\vec{S}_i$ and $\vec{S}_j$ represent neighbouring spins and the sign of J, the exchange integral, determines if the exchange is symmetric (ferromagnetic) or anti-symmetric (antiferromagnetic). There is a number of different mechanisms through which magnetic exchange can occur, and we will explore the two which are relevant to this thesis.

The first is direct exchange [24], in which the magnetic exchange interaction happens directly through neighbouring atoms. Because atoms are often too distant for the orbitals hosting the unpaired electron to overlap, this magnetic exchange is often too weak to be noticed. The second exchange mechanism is called superexchange, in which two next-to-nearest neighbour metals undergo exchange through a non-magnetic mediator [25]. If the mediator was also magnetic, then we would simply be faced with direct exchange. In the superexchange mechanism, the mediator's orbitals overlap with the metal's orbitals, therefore acting as a "medium" through which the magnetic interactions of the two metals are coupled, either ferromagnetically or anti-ferromagnetically, despite the metals being relatively far apart. Other exchange interactions include double exchange, the Dzyaloshinskii–Moriya interaction, the RKKY interaction and dipolar exchange [26]. When incoherent exchange interactions are present in a material simultaneously, they cause magnetic frustration, as will be explored in chapter 4.

1.3 Research motivation

The motivation behind this *ab initio* computational research is to understand, develop and optimise a new class of quantum materials with the potential of revolutionising the information technology (IT) world by exhibiting switchable and stimuli-responsive characteristics [27]. Quantum materials, such as strongly correlated materials, are growing in popularity thanks to their ability to achieve reversible metal–insulator transitions, a property of great use in the IT world [28]. These types of transitions of a material from a metal to an insulator, and even to a semiconductor, can be attained by altering a series of parameters such as pressure, temperature, or doping [29].

The 20^{th} century has been revolutionised by semiconductors which made computation and information technology a reality, while the big focus of the 21^{st} century is quantum materials, with great potential in transforming memory, sensing, information, energy, and related technologies [30], being the overall motivation behind this thesis. The limitations of classical band-based semiconductors [31], such as silicon, will require the IT world to look for alternatives with more complex physics, such as strongly correlated semiconductors. Technology has reached a need for novel materials that can compute and store information in new ways, and quantum materials are one of the most promising ways of achieving this goal. These novel materials exhibit non-trivial magnetic and electronic properties, such as colossal magnetoresistance (like manganese-based perovskite oxides) by coupling magnetism and electricity to form magnetoelectrics [32], quantum-spin liquids by exploiting topological properties [33] and high-temperature superconductivity to form qubits [34, 35]. The careful tuning of doping, delocalisation and correlation in these materials holds the potential of revolutionising the computing world, leading to spintronics [36] or even quantum computing [37].

1.3.1 The essentiality of DFT for technology and science

The discovery of new materials is often driven by experimentally synthesising them and later testing their properties. Known chemical trends and previous research are of great value in such an approach, but the trial-and-error aspect persists. This approach is somewhat inefficient in terms of money, time and laboratory equipment usage. One alternative, often used in conjunction with the experimental approach just mentioned, is the design of new materials *in silico*, such as using DFT [38]. For a novel unknown hypothesised material, DFT is able to predict a series of material properties without any experimental equipment, although the usage of appropriate computational resources, such as computer clusters, is needed. DFT allows for a series of properties to be computationally calculated, such as electronic structure, phonon modes or electrical conductivity. Furthermore, DFT can facilitate structure prediction and refinement of new materials as it can geometry optimise a system by relaxing its atoms to the lowest energy positions [39].

On top of this, laboratory experiments can measure properties, such as conductivity or magnetism, but give no explicit insight into why these results are seen or the quantum mechanics driving them. On the other hand, DFT applies quantum mechanics directly onto the system of study and outputs quantum mechanical results which no experiment can see explicitly, such as molecular orbital shapes [40]. In addition, different properties can be included or excluded in the computational model to see if they play a major role in the system of study or if they are relatively negligible. This helps to pinpoint the driving science behind the different observed properties. This approach gives insight into what modification must be made to materials in order to meet a set of criteria that solve technological problems. It is through deep understanding that progress is made in this field of science.

1.3.2 Research scope

The scope of this thesis is to investigate strongly correlated materials by focusing on two promising structures, the first being the $CrCl_2(pym)$ metal-organic magnet, a candidate structure for the S=2 Haldane phase, and the second being $Cu_4(OH)_6FBr$, a candidate structure for the quantum spin liquid phase. One of the goals for each of these structures is to attain an accurate structural lattice geometry by investigating the forces at play while relaxing their structures. Further goals consist of studying their electronic behaviour by generating band-structure plots and density of states diagrams, as well as solving for their molecular orbitals and charge density. On top of this, this study will focus towards understanding the type of magnetic interactions involved, the magnetic exchange mechanisms and any other physics specific to the system of interest.

After having developed and optimised a robust DFT+U approach suitable for studying strongly correlated materials, a second scope of this research consists in predicting novel unknown structures by computationally synthesising them based on the previously studied metal-organic magnet. The science governing these new theoretical structures is investigated, and the electronic and magnetic properties of these new quantum materials are discovered, opening new possibilities for the technological and scientific sectors.

Chapter Two

Electronic Structure Theory

Quantum mechanics is at the core of analysing crystal properties, such as energetics, structures at the atomic level, vibrational properties, electronic response properties, etc. To do this, the shared-source academic and commercial software package CASTEP [41] has been used throughout this research. In this chapter, the plane-wave DFT approach used throughout this research is carefully explained.

2.1 The many-body problem

In order to find the electronic structure of a system of N interacting electrons of charge e and mass m_e, and M nuclei of charge Z and mass m_I, the full many body Hamiltonian must be taken into account, which takes the following form [42]:

$$\begin{aligned}\hat{H} = &-\frac{\hbar^2}{2m_e}\sum_{i}^{N}\nabla_i^2 - \frac{\hbar^2}{2m_I}\sum_{I}^{M}\nabla_I^2 - \frac{1}{4\pi\varepsilon_0}\sum_{i}^{N}\sum_{I}^{M}\frac{Z_I e^2}{|\vec{r}_i - \vec{R}_i|} \\ &+ \frac{1}{8\pi\varepsilon_0}\sum_{i}^{N}\sum_{j\neq i}^{M}\frac{e^2}{|\vec{r}_i - \vec{r}_j|} + \frac{1}{8\pi\varepsilon_0}\sum_{I}^{M}\sum_{J\neq I}^{M}\frac{Z_I Z_J e^2}{|\vec{R}_i - \vec{R}_J|}\end{aligned} \tag{2.1}$$

The electronic positions are $\vec{r}_i$ while the atomic positions are $\vec{R}_i$. The first two terms of this equation are the kinetic energy of the electrons and the nuclei respectively. The next three terms account for the electron-nuclei interaction, the electron-electron interaction and the nuclei-nuclei interaction. To prevent counting a self-interaction of the electrons and nuclei with themselves, the i = j and I = J are not included in the last two double-sums. These two double-sums also include a front factor of 1/2 to prevent double counting. Also, spin-orbit coupling has not been included as it would require the wavefunctions to be represented by spinors, as later discussed in section 2.5.4.

Following equation 2.1, the explicit form of the Hamiltonian used in the many-body time-independent Schrödinger equation takes the form:

$$\hat{H}\Psi(\{\vec{R}_I\},\{\vec{r}_i\}) = E\Psi(\{\vec{R}_I\},\{\vec{r}_i\}) \tag{2.2}$$

For a system containing more than a few electrons, this equation cannot be exactly solved because an analytical solution cannot be found and it is too complex to be solved computationally, therefore, approximations must be made. Two approaches have been developed over the years, focusing on the electron density or on the wavefunction, each with its own advantages and disadvantages.

Wavefunction approaches use an explicit form of the wavefunction from which observables are then calculated. These methods include perturbational approaches, such as Moller-Plesset and diagrammatic methods, as well as variational approaches, including Hartree-Fock or the configuration interaction method. These methods are often very computationally expensive but offer accurate results.

Density-based approaches, on the other hand, focus on the electronic density instead of the explicit wavefunction, which is not explicitly calculated. These methods are often less computationally demanding and still offer relatively accurate results, such as the Thomas-Fermi approximation and density-functional theory. Before diving into density-based methods, the more classical wave-function approach is examined.

In order to simplify the problem at hand and decrease degrees of freedom, a series of approximations can be used, the main one being the Born-Oppenheimer approximation. Since nuclei are about 2,000 times heavier than electrons, they can be assumed to be fixed in place relative to the electrons. Of course this is not strictly representative of reality, not only because the nuclei are not indeed static, but also because there is always an inherent uncertainty in the position of the nuclei according to Heisenberg's Uncertainty Principle. However, as nuclei are orders of magnitude larger than electrons, their wavefunction is relatively localised and therefore such an approximation can be implemented provided that temperature is not taken into account. Such a static approximation of nuclei, known as the adiabatic approximation, allows for the decoupling of the motion of the electrons and nuclei. This simplifies the third term of equation 2.1 to a simple external potential term. A new Hamiltonian can therefore be defined for the electrons only. Note that nuclei are static and Hartree atomic units [43] ($e = m_e = \hbar = \frac{1}{4\pi\varepsilon_0} = 1$) have been used.

$$\hat{H}_{elec} = -\frac{1}{2}\sum_{i}^{N}\nabla_i^2 - \sum_{i}^{N}\sum_{I}^{M}\frac{1}{|\vec{r}_i - \vec{R}_I|} + \frac{1}{2}\sum_{i}^{N}\sum_{j\neq i}^{M}\frac{1}{|\vec{r}_i - \vec{r}_j|} + V_{nn} \tag{2.3}$$

The V_{nn} accounts for the Coulomb interaction between the static nuclei, which has been included for completeness in the electronic Hamilotnian presented above. Such an equation therefore leads us in finding the potential energy surface minima, reaching the electronic ground state. Finding these local minima can be done using computational iterative approaches, as later explained. This becomes a powerful tool at our disposal. For instance, by treating the nuclei classically, their positions can be shifted towards the minimum of the potential energy surface, therefore relaxing the structure. More on these approaches will be later explained.

2.2 Hartree-Fock theory

The Hartree approach, detailed in Ref[44], considers the wavefunction as a product of single particle wavefunctions, as if the electrons were independent. This approximation therefore decouples the electrons leading to a series of single particle equations of the following form:

$$-\frac{1}{2}\ \nabla_i^2\psi_i(r) + V_i(r)\psi_i(r) = \varepsilon_i\psi_i(r) \tag{2.4}$$

The problem with such an approximation is the lack of particle exchange symmetry. In order to take into account an antisymmetric particle exchange nature, the many body wavefunction is described by a Slater determinant consisting of the N orthogonal single particle wavefunctions. This is a smart solution to impose antisymmetric exchange, as swapping two rows or columns results in a sign flip.

$$\Psi(\vec{r}) = \frac{1}{\sqrt{N!}} \begin{vmatrix} \psi_1(\vec{r}_1) & \psi_2(\vec{r}_1) & \cdots & \psi_n(\vec{r}_1) & \\ \psi_1(\vec{r}_2) & \psi_2(\vec{r}_2) & \cdots & \psi_n(\vec{r}_2) & \\ \vdots & \vdots & \vdots & \ddots & \vdots \\ \psi_1(\vec{r}_n) & \psi_2(\vec{r}_n) & \cdots & \psi_n(\vec{r}_n) & \end{vmatrix} \tag{2.5}$$

This is the Hartree-Fock theory, and works by implementing the variational principle of quantum mechanics. This means that the ground state energy E_0 of our system will always be less than or equal to the expectation value $\tilde{E}$:

$$\tilde{E} = \langle\Psi|\hat{H}_e|\Psi\rangle \geq E_0 \tag{2.6}$$

The expectation value can be calculated using Ψ described by the Slater determinant presented in 2.5.

The mathematics can be simplified exploiting the following property held by the Slater determinant, $\int \psi_i^* \psi_j \, d\vec{r} = \delta_{ij}$, resulting in the following expectation value:

$$\begin{aligned}\tilde{E} = & -\frac{1}{2}\sum_i \int \psi_i^* \nabla_i^2 \psi_i \, d\vec{r} + \frac{1}{2}\iint \frac{\rho(\vec{r'})\rho(\vec{r})}{|\vec{r}-\vec{r'}|} \, d\vec{r}d\vec{r'} \\ & -\frac{1}{2}\sum_{ij} \iint \frac{\psi_i^*(\vec{r})\psi_j(\vec{r})\psi_j^*(\vec{r'})\psi_i(\vec{r'})}{|\vec{r}-\vec{r'}|} \, d\vec{r'}d\vec{r} - \sum_I Z_I \int \frac{\rho(\vec{r})}{|\vec{r}-\vec{R_I}|} \, d\vec{r}\end{aligned} \tag{2.7}$$

For the first time, in equation 2.7 we come across the electron density:

$$\rho(\vec{r}) = \sum_{i=1}^{N} |\psi_i(r)|^2 \tag{2.8}$$

Now that we have an equation for the expectation value of energy, we can implement variational calculus techniques to minimise $\tilde{E}$.

This leads to a system of N Hartree-Fock single particle eigenvalue equations shown in 2.9, each electron having its own equation. This system of equations has to be solved self-consistently through an iterative process since the output also forms part of the input. Once a desired convergence is reached, the Hartree energy is found, as later explained in section 2.4.2.

$$\left[-\frac{1}{2}\nabla_i^2 + \int \frac{\rho(\vec{r'})}{|\vec{r}-\vec{r'}|} \, d\vec{r'} + \hat{V_n}\right] \psi_i(\vec{r}) - \sum_j \psi_i(\vec{r}) \int \frac{\psi_j^*(\vec{r'})\psi_i(\vec{r'})}{|\vec{r}-\vec{r'}|} \, d\vec{r'} = \epsilon_i \psi_i(\vec{r}) \tag{2.9}$$

There are four terms in 2.9: electron's kinetic energy, Hartree potential accounting for the electron's Coulombic interaction with the electron density, the electron-nuclei Coulomb "external" potential and the Fock-exchange purely arising from quantum mechanics.

These terms make up the Hartree-Fock approach, which can be summarised in equation 2.10:

$$E_{HF} = T + E_H + E_{ext} + E_X \tag{2.10}$$

After iteratively solving the system of Hartree-Fock equations, an E_{HF} is found, which approximates the true ground-state energy E_0. The difference between E_{HF} and the true ground-state energy E_0 is the correlation energy. To some extent, the Hartree-Fock approach takes into account electron correlation, found in the electron exchange term describing the correlation between electrons with parallel spin. However, it does not take into account other forms of correlation such as Coulomb correlation, accounting for the correlation between the spatial position of electrons due to their Coulomb repulsion. The term correlation energy can be intuitively thought of as a measure of how much the movement of one electron is influenced by the presence of all other electrons. As previously explained, the Hartree-Fock approach approximates the anti-symmetric wavefunction by a single Slater determinant. However, a single determinant is generally not sufficient to express exact wavefunctions, and such an approximation does not adequately take into account correlation. Although not being a dominant term, correlation energy plays an essential role when working with strongly correlated materials, meaning that the Hartree-Fock approach is inadequate for such systems. It is therefore important to find an alternative computational method which does account for correlation, one of the most promising being DFT, which will be explored in the following section.

2.3 Density-functional theory

Density-functional theory is one of the most used *ab initio* computational approaches in materials science. It differs from Hartree-Fock by working with the electron density instead of the explicit wavefunction. The fundamentals of DFT are described by the Hohenberg-Kohn Theorems presented below, proving that the electron density determines all the ground state properties of a system. An outline of DFT is presented below and details can be found in Ref [45, 46].

2.3.1 Hohenberg-Kohn theorems

Hohenberg-Kohn Theorem 1

The external potential $V_{ext}(\vec{r})$, arising from the presence of the fixed nuclei, is uniquely determined by the ground state density $\rho_0(\vec{r})$, up to a constant [47]. This means that the external potential is a functional of only the electron density. To understand why this is the case, let us assume the opposite: one ground state charge density $\rho_0(\vec{r})$ for two separate external potentials $V_1(\vec{r})$ and $V_2(\vec{r})$ differing by more than a constant, with two different Hamiltonians and wave-functions and with energies $E_1 = \left\langle \Psi_1|\hat{H}_1|\Psi_1 \right\rangle$ and $E_2 = \left\langle \Psi_2|\hat{H}_2|\Psi_2 \right\rangle$. Applying the variational principle of quantum mechanics, we find the following:

$$\begin{aligned}
&E_1 < \left\langle \Psi_2|\hat{H}_1|\Psi_2 \right\rangle = \left\langle \Psi_2|\hat{H}_2|\Psi_2 \right\rangle - \left\langle \Psi_2|\hat{H}_2 - \hat{H}_1|\Psi_2 \right\rangle = E_1 - \int \rho_0(\vec{r})\,[V_2(\vec{r}) - V_1(\vec{r})]\,d\vec{r} \\
&E_2 < \left\langle \Psi_1|\hat{H}_2|\Psi_1 \right\rangle = \left\langle \Psi_1|\hat{H}_1|\Psi_1 \right\rangle - \left\langle \Psi_1|\hat{H}_1 - \hat{H}_2|\Psi_1 \right\rangle = E_2 - \int \rho_0(\vec{r})\,[V_1(\vec{r}) - V_2(\vec{r})]\,d\vec{r} \\
&\therefore E_1 + E_2 < E_1 + E_2
\end{aligned} \tag{2.11}$$

Assuming that E_1 and E_2 are non-degenerate, $E_1 + E_2 < E_1 + E_2$ is clearly absurd, meaning that, $\rho_0(\vec{r})$ uniquely determines the external potential.

Hohenberg-Kohn Theorem 2

For any external potential $V_{ext}(\vec{r})$ there exists a functional for the energy in terms of density $E[\rho]$. The density which minimises this functional is the ground-state density $\rho_0(\vec{r})$; and the minimum of this functional is the ground-state energy [47]. To understand this, let us take two densities: the ground-state density $\rho_0(\vec{r})$ and another non-ground state density $\rho'(\vec{r})$. As the first theorem states, each of these will uniquely correspond to a Hamiltonian. Applying the variational principle, we find:

$$E[\rho'] = \left\langle \Psi'[\rho'] \,|\hat{H}|\Psi'[\rho'] \right\rangle > \left\langle \Psi_0[\rho_0] \,|\hat{H}|\Psi_0[\rho_0] \right\rangle = E[\rho_0] \tag{2.12}$$

Combining these two theorems proves that there exists a single functional $F_{HK}[\rho]$ which simplifies the complexity of the many-body problem down to a simple energy minimisation calculation, in which the energy is:

$$E[\rho] = \int \rho(\vec{r}) V_{ext}(\vec{r}) \, d\vec{r} + F_{HK}[\rho] \tag{2.13}$$

This is a very powerful approach which would revolutionise *ab initio* calculations, but the exact form of the functional $F_{HK}[\rho]$ is unknown to this day. However, as we will next explore, the mystery of this functional was not enough to take DFT to a dead-end thanks to the studies of Walter Kohn and Lu Jeu Sham.

2.3.2 Kohn-Sham approach

Since the functional $F_{HK}[\rho]$ is unknown and approximations of it have not shown much success, especially due to the inability to account for kinetic energy, the Kohn-Sham (KS) approach uses a fictitious set of non-interacting KS electrons in a KS potential V_{KS}. The Kohn-Sham energy is [48]:

$$E_{KS}\left[\rho, \Psi\right] = T\left[\Psi\right] + E_H\left[\Psi\right] + E_{ext}\left[\rho\right] + E_{xc}\left[\rho\right] \tag{2.14}$$

This is an exact equation, as all unknowns are gathered into the exchange correlation E_{xc} functional:

$$E_{xc} = \Delta E_{ee} + \Delta T \tag{2.15}$$

The E_{xc} term arises from the electrons, which, in reality, do interact. Electrons experience an exchange energy caused by the Pauli repulsion, omitted in the Hartree term, as well as a correlation energy caused by the repulsion between them. In addition, this term accounts for the fact that the kinetic energy calculated is a non-interacting kinetic energy of the KS particles and corrects for this.

In order to achieve the Kohn-Sham equations, the Kohn-Sham energy E_{KS} is minimised with respect to variations in $\{\Psi_i^*(\vec{r})\}$ as shown in equation 2.16, with $\int \Psi_i^*(\vec{r})\,\Psi_j(\vec{r})\,d\vec{r} = \delta_{ij}$. This results in the following [45]:

$$\frac{\delta E_{KS}}{\delta \Psi_i^*(\vec{r})} = \frac{\delta T}{\delta \Psi_i^*(\vec{r})} + \left[\frac{\delta E_{ext}}{\delta \rho(\vec{r})} + \frac{\delta E_H}{\delta \rho(\vec{r})} + \frac{\delta E_{xc}}{\delta \rho(\vec{r})}\right] \frac{d\rho(\vec{r})}{d\Psi_i^*(\vec{r})} \tag{2.16}$$

with the 5 terms being evaluated as follows:

$$
\begin{aligned}
&\frac{\delta T}{\delta \Psi_i^*(\vec{r}\,)} = -\frac{1}{2}\,\nabla^2\,\Psi_i(\vec{r}\,) \\
&\frac{\delta E_{ext}}{\delta \rho(\vec{r}\,)} = V_{ext}\,(\vec{r}\,) \\
&\frac{\delta E_H}{\delta \rho(\vec{r}\,)} = \frac{1}{2}\int \frac{\rho(\vec{r'}\,)}{|\vec{r}-\vec{r'}|}\,d\vec{r'} = V_H(\vec{r}\,) \\
&\frac{\delta E_{xc}}{\delta \rho(\vec{r}\,)} = V_{xc}(\vec{r}\,) \\
&\frac{d\rho(\vec{r})}{d\Psi_i^*(\vec{r}\,)} = \frac{d}{d\Psi_i^*(\vec{r}\,)}\left[\sum_i \Psi_i^*(\vec{r}\,)\Psi_i(\vec{r}\,)\right] = \Psi_i(\vec{r}\,)
\end{aligned}
\tag{2.17}
$$

resulting in the following single particle Kohn-Sham equations [48]:

$$
\begin{aligned}
\left(-\frac{1}{2}\,\nabla^2 + V_{KS}\right)\Psi_i(\vec{r}\,) = \varepsilon_i \Psi_i(\vec{r}\,) \\
V_{KS}(\vec{r}\,) = V_{ext}(\vec{r}\,) + V_H(\vec{r}\,) + V_{xc}(\vec{r}\,)
\end{aligned}
\tag{2.18}
$$

Each of the Kohn-Sham equations has a kinetic energy term and a Kohn-Sham potential (V_{KS}) term. The Kohn-Sham potential encapsulates the following three terms: an external potential term due to the interaction with the "static" atomic nuclei, a Hartree potential term due to the interaction with the average electromagnetic field and an exchange-correlation potential term described in 2.15. Just as in the Hartree-Fock approach, these equations have to be solved self consistently, in which the electron density, initially given as an input, is calculated by the code until convergence. Details on carrying out DFT calculations are presented in section 2.4.

In equation 2.18, ε_i is a Lagrange multiplier introduced as an orthonormality constraint. From this Kohn-Sham system of non-interacting electrons, the total energy is $E_{non-int} = \sum_i \varepsilon_i$. However, if we wish to derive the energy of the real system of interacting electrons we have to remember to subtract the Hartree energy since it is double counted and adjust the exchange correlation energy. Therefore, for a system of interacting electrons, the true total energy is

$$E_{KS} = \sum_i \varepsilon_i - \frac{1}{2}\iint \frac{\rho(\vec{r'})\rho(\vec{r})}{|\vec{r} - \vec{r'}|}\, d\vec{r} d\vec{r'} - \int \rho(\vec{r}) V_{xc}(\vec{r})\, d\vec{r} + E_{xc}\left[\rho(\vec{r})\right] \tag{2.19}$$

After having calculated the Kohn-Sham equations, we will now shift our focus on the exchange-correlation functional. Despite knowing that the accurate form of this functional exists, it has yet to be discovered.

2.3.3 Exchange-Correlation Functionals

Since the exchange correlation functional is unknown, over the years different approximations have been created. The most basic of these is the local density approximation, taking the E_{xc} to be a local functional of the density as follows [49]:

$$E_{xc}^{LDA}[\rho(\vec{r})] = \int \rho(\vec{r})\, \epsilon_{xc}\left(\rho(\vec{r})\right) d\vec{r} \tag{2.20}$$

where ϵ_{xc} is the exchange-correlation energy for a homogeneous electron gas of density ρ. Using a homogeneous electron gas approach to model a solid is a crude approximation which is reasonable for potentials which do not change rapidly. The advantage of this is that the exchange part of the exchange correlation energy can be calculated analytically while the correlation part can be calculated using quantum Monte Carlo simulations [50].

This E_{xc}^{LDA} functional paved the way for a series of more advanced functionals. A popular class of functionals are the generalised-gradient approximation (GGA) functionals, which account for the inhomogeneity of the density by including its first derivative. Amongst many within this family, the functional mostly used throughout the research presented in the chapters to follow is the Perdew-Burke-Ernzerhof (PBE) functional [51]. More complex functionals are becoming more popular, such as the SCAN meta-GGA functional, which also includes the kinetic energy density and higher density derivatives. However, no significant improvement has been seen using the SCAN meta-GGA functional with the strongly correlated materials dealt with throughout this research. The SCAN functional was found to present the same problems as other more simple and less computationally expensive functionals, such as the need for a Hubbard U correction, as explained in section 2.5.2, and therefore presents no significant benefit of using it. This is not to say that PBE does not have its own drawback: PBE under-binds the atoms in a cell and, just like LDA, PBE underestimates the band-gap of semiconductors and insulators [52]. One attempt to improve on this band-gap problem is the creation of Hybrid functionals, in which they incorporate a part of Hartree–Fock exchange.[53]. HSE is one functional under this Hybrid family, which has been used throughout this research.

2.4 Practical aspects of DFT

In materials science we usually focus on solids, whose constituents are often arranged in a periodic ordered structure forming a crystal lattice that tessellates across the entire structure. The most convenient way to apply DFT to such systems is to use planewaves as the basis set with pseudo-potentials [54]. This requires the system to be modelled as ordered periodic crystals, and the use of periodic boundary conditions allows the usage of a relatively small unit cell that DFT can work on. Common to solid state physics research, reciprocal space is used instead of the real space throughout calculations.

2.4.1 Plane-wave DFT and pseudo-potentials

If the nuclei are arranged in a periodically repeating pattern, their potential acting on the electrons must also be periodic, along with the density and the magnitude of the wavefunction. According to Bloch's theorem [55], the Kohn-Sham eigenfunctions can be described as:

$$\psi_{n\vec{k}}(\vec{r}) = e^{i\vec{k}\cdot\vec{r}}\ u_{n\vec{k}}(\vec{r}) \tag{2.21}$$

with $\vec{k}$ representing the wavevector and n the band number. The lattice, with lattice vector $\vec{R}$, has the same periodicity as the Bloch functions, $u_{n\vec{k}}(\vec{r})$. The Kohn-Sham wavefunctions for a crystal of volume Ω_s can therefore be written as:

$$\psi_{n\vec{k}}(\vec{r}) = \frac{1}{\sqrt{\Omega_s}}\sum_{G} c_{n\vec{k}}(\vec{G})\ e^{i(\vec{G}+\vec{k})\cdot\vec{r}} \tag{2.22}$$

where $\vec{G}$ are the reciprocal lattice vectors. The number of these reciprocal lattice vectors is infinite, however DFT calculations only need to include as many of these as needed to converge specific parameters of interest. This is set by specifying a cut-off energy: $E_{cut} = \frac{1}{2}|\vec{k}+\vec{G}|^2$. Following this approach, the charge density can be found by integrating over the first Brillouin Zone (BZ) and is expressed as [48, 56]:

$$\rho(\vec{r}) = \sum_{n}\int_{BZ}\frac{1}{\Omega_s}|u_{n\vec{k}}(\vec{r})|^2 d\vec{k} \tag{2.23}$$

Once the charge density is known, it can be placed back into the Hamiltonian and the various quantities of interest can be derived. Using a finite number of $\vec{G}$ reciprocal lattice vectors means that the higher $\vec{G}$ vectors above the cut-off energy are not included in our calculations. This is a problem when the wavefunction is varying very quickly as these large G components describe such regions of space. To overcome this, the Coulomb potential near each nucleus can be replaced with a modified, weaker potential, known as a pseudopotential. The pseudopotential is an effective potential which eliminates the atomic core states while maintaining the orthogonality of the system and results in an accurate representation of the valence electrons, which are described by pseudo-wavefunctions. In essence, the atoms' nuclei and core electrons are considered as simple ions.

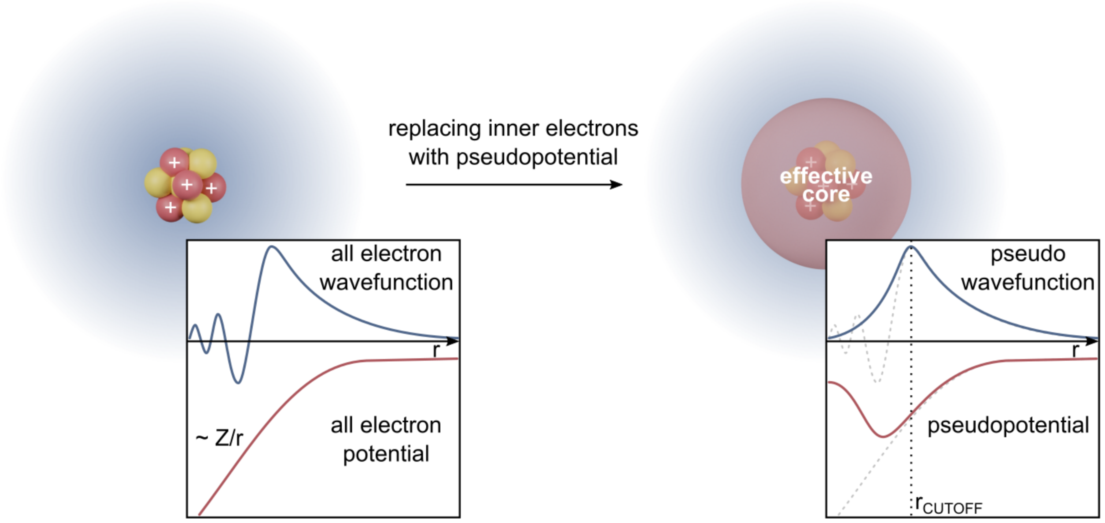

Figure 2.1: Visual representation demonstrating the idea of a pseudo-potential. A cut-off radius (r_{CUTOFF}) is chosen after which the pseudo-wavefunction matches the true full-potential wavefunction. Figure created by Edvin Fako [57].

Depending on the type of research, the atomic core states are often not of great interest since they do not affect the chemical, mechanical or electronic properties very much, meaning that pseudo-potentials are a convenient and suitable choice. Of course, if the research is focusing on the core states, such as in core level spectroscopy like near edge x-ray absorption spectroscopy studies, making use of such pseudo-potentials would not be a suitable approach.

Although plane-wave DFT is found successful in modelling many crystal structures, some systems require a better description of van der Waals interactions than what standard DFT alone provides. Dispersion corrections are applied to achieve this. There are five common procedures for implementing dispersion corrections: non-local correlation functionals [58], empirical atom–atom dispersion potentials [59], the Becke-Johnson exchange-dipole model [60], the Tkatchenko-Scheffler van der Waals method [61] and, finally, the many-body dispersion method [62]. In this thesis, the many-body dispersion (MBD^*) correction has been used because it is not highly computationally demanding, yet outperforms other methods, since it goes beyond the pairwise-additive treatment of dispersion taken by many of them. The van der Waals dispersion energy in MBD^* is calculated using the ground-state electron density and includes both short range and long range electrostatic screening effects. This is to account for the polarisation effects experienced by atoms exposed to a dynamic electric field created by the surrounding atoms of the molecule. MBD^* calculates the dynamic response of a system by modelling it via a set of dipole-coupled quantum harmonic oscillators [63]. The correlation energy is expressed as:

$$E_c = \frac{1}{2} \sum_{p=1}^{3N} (\bar{\omega}_p - \omega_p) \tag{2.24}$$

where N is the number of quantum harmonic oscillators used, $\bar{\omega}_p$ are the frequencies of the interacting (dipole-coupled) system and ω_p are the frequencies of the non-interacting system. The energy difference between the interacting and non-interacting oscillators is therefore used to calculate the van der Waals interaction energies of the system. This is only an introduction of the basic ideas, however a complete explanation with detailed implementation schemes can be found in Ref [64–67]. Dispersion corrections are a very active field of development in the DFT world and new clever schemes are under development with promising results [68].

2.4.2 DFT applications

There are a number of different uses for which DFT has been applied throughout this research. The main ones consist of single-point energy calculations, geometry optimisations, band-structure and density of states (DOS) calculations. Out of these, single-point energy calculations form the foundations upon which all other types are built upon.

Single-point calculations consist of applying the DFT formalism presented above to a crystalline system in order to find the ground state total energy of the system. This is done self-consistently, in the following manner: first an initial guess of an input electron density is made. Then, it is used to calculate the effective potential of the system. At this point, the Kohn-Sham equations are solved and a new output density is calculated according to equation 2.23. If the input and output densities are within a predefined margin of error, the ground state energy of the system is found. If the input and output densities are not within the margin of error, the output density is used to generate a new input density, as explained in the following paragraph, and a new self consistent field (SCF) cycle begins.

Looking at this process in more detail, there are a number of different self-consistent electronic minimisation methods available which may somewhat deviate from the theoretical scheme presented above, the most popular being density mixing [69–71]. In this approach, the new charge density at the end of an SCF cycle is mixed with the initial one and the process is repeated until convergence. This mixing can be done following different schemes: linear mixing, Kerker mixing, Kerker-Broyden mixing, and Kerker-Pulay mixing. The most robust method found to work with the materials in this research is the Kerker-preconditioned Broyden mixing scheme, in which the output density is mixed with densities from a number of previous iterations, using a quasi-Newton relaxation method [72].

An alternative scheme to density mixing is the ensemble density functional method (EDFT)[73], directly minimising the total energy of the system. The wavefunctions of the electrons described using a plane-wave basis set and the expansion coefficients are modified in order to minimise the net energy of the system. This means that the density is reconstructed whenever the wavefunctions or occupancies change, which happens during the energy minimisation process. More specifically, each SCF cycle consists of a number of wavefunction updates, each one followed by an update of the occupancies. This approach is therefore based on an all-bands wavefunction search, followed by the self-consistent updating of occupancies in the case of metals.

Once the ground state total energy of a system has been reached, a series of properties of the system can be found. For example, forces acting on the atoms can be calculated using the first derivative of the total energy with respect to the nuclear atomic coordinates. The calculation of forces allows the optimisation of the geometry of a system, as discussed in the following paragraph. Additionally, second derivatives of the energy with respect to volume, parameters of the unit cell, and the fractional coordinates of the atoms can respectively output the bulk modulus, the elastic constants and vibrational properties [74].

The second type of calculations worth exploring are geometry optimisations. A geometry optimisation consists of an iterative process in which the total energy of the system is minimised by adjusting the coordinates of the atoms and the cell parameters. This is achieved by locating minima and saddle points on the potential energy surface and therefore reducing the magnitude of calculated forces and stresses until they fall under a predefined tolerance.

Two common methods for carrying out geometry optimisations are BFGS [75] and damped molecular dynamics [76]. In this thesis, the BFGS approach has been adopted because it allows for both the cell lattice vectors and the internal coordinates of the atoms to be optimised, whereas the CASTEP damped molecular dynamics method keeps the cell parameters unchanged. The BFGS approach makes use of an initial Hessian which is recursively updated during the optimisation. The Hessian is a square matrix of second-order partial derivatives, and is used to find the minima of the potential energy surface. A development on this approach is the limited-memory BFGS algorithm (LBFGS) [77] which uses a restricted number of Hessian updates to construct the new Hessian.

The last type of DFT calculations carried out throughout this work are band-structure and density of states calculations. Band structure calculations use the ground-state electron charge density to compute the electronic energies with respect to k-vectors, along high symmetry directions in the Brillouin zone. Following the DFT formalism presented earlier in this chapter, the band-structure is calculated using Kohn-Sham states, not the true electron orbitals. Despite this being a good approximation, it may lead to scenarios in which the ground state energy and its derived properties are accurate, like forces, but the band-structure is less precise. For instance, scenarios arise in which the band gap is miscalculated in band structure plots due to the integer nature of electrons causing a derivative discontinuity of the total energy as a function of the total number of electrons [78]. On top of this, the band gap can be further miscalculated due to the self-interaction error which arises in the occupied states in standard DFT, and in the unoccupied states in the Hartree-Fock approach. Despite having to carefully scrutinise band-structure results for the presence of inaccuracies, a number of useful properties can be deduced from these calculations, from visualising energy band gaps to investigating directions with relatively flat, dispersionless bands. Even the nature of bands can often be inferred, as narrow bands of d and f states are easily distinguished from free electron like bands that correspond to s and p orbitals. These results are often most useful when combined with density of states plots. Density of states calculations compute the number of electron states per unit volume per unit energy, or, in other words, the number of different states at a particular energy level that electrons are allowed to occupy. Bulk properties such as specific heat or paramagnetic susceptibility depend on the density of states of the material. In this research, the projected density of states (PDOS) has been used instead of the total DOS, which is obtained by projecting the DOS onto local orbitals at each atomic site. This has been done using the OptaDOS [79] code.

2.5 Modelling strongly correlated quantum materials

Working with strongly-correlated materials is challenging because they tend to present properties typical of atomic/molecular physics despite being in a crystal structure. These types of materials present strong interactions between electrons and often include ions with narrow localised d or f open shells. For instance, $3d$ electron compounds with partially filled d states are a common type of strongly-correlated materials, later presented in this thesis. In general, d or f orbitals are smaller than s or p orbitals, meaning that electrons in d or f orbitals are in close proximity and the Coulomb interactions are much stronger [80]. DFT, which fundamentally works with a fictitious set of non-interacting Kohn-Sham electrons, struggles to account for the strong electron correlations, and therefore corrections or alternative approaches beyond Kohn-Sham DFT are needed when working with quantum materials. The most common model to describe the nature of strongly correlated materials is the Hubbard model, explored in the following section.

2.5.1 The Hubbard model

Electrons in crystals present both an itinerant delocalised nature, predominant in metals, and a localised atom-bound nature, predominant in insulators. In the case of the Hubbard model [81, 82], the first term favours delocalisation (metal) whereas the second term favours localisation (insulator). Electrons in strongly correlated materials present both of these behaviours, which can be combined to form the Hubbard Model [83, 84]:

$$\hat{H} = -t \sum_{\langle i,j \rangle,\sigma} (\hat{c}^{\dagger}_{i\sigma}\hat{c}_{j\sigma} + \hat{c}^{\dagger}_{j\sigma}\hat{c}_{i\sigma}) + U \sum_{i} \hat{n}_{i\uparrow}\hat{n}_{i\downarrow} \tag{2.25}$$

Two terms are present in this equation: a kinetic energy term, allowing for hopping of electrons between lattice sites, and a potential energy term, reflecting on-site interaction.

To start, the first term, corresponding to the hopping term, is examined. In this term we find the hopping integral t which calibrates the strength of this term. To calculate the energy of an electron with spin σ undergoing quantum tunnelling and hopping from one lattice site i to its neighbouring site j, the Hubbard model creates an electron in the new site while removing it from the old one, done via the use of pairs of creation and annihilation operators denoted as $\hat{c}^{\dagger}_{i\sigma}\hat{c}_{j\sigma}$ and $\hat{c}^{\dagger}_{j\sigma}\hat{c}_{i\sigma}$.

Let us now examine the second term, the on-site interaction term. U is the electronic repulsion term, or, in other words, the energy for having two electrons, one spin up and the other spin down, at lattice site i. The $\hat{n}_i$ is the spin dependent electron number operator, meaning that it can be either 0 if no electron of that spin is present or 1 if it is. This means that when two electrons (spin up and down) are present at site i $E = U$, otherwise this term is equal to zero.

Strongly correlated materials present unexpected electronic properties caused by a competition between hopping integrals, leading to electron delocalisation, and on-site Coulomb interaction, generating atomic-like behaviour [85]. In the physical world, such peculiar quantum effects can often be affected by perturbations in external parameters, such as changes in temperature or pressure. For instance, these physical changes modify the ratio of the Coulomb repulsion U to the hopping t, resulting in metal-insulator transitions, as seen in Mott insulators. According to band theory, electrical conduction happens when an electric field is applied to a system with semi-filled overlapping bands. However, there is a class of materials, known as Mott insulators [86], which do not conduct, despite meeting the conduction criteria, due to the strong repulsion between electrons. In these types of materials, the energy cost of finding the “conducting” electron next to another electron as it conducts is very high and outweighs the electric field, and, therefore, no conduction takes place.

2.5.2 DFT+U

DFT struggles to account for the strong Coulomb repulsion between f or d electrons, and Anisimov *et al.* [87] introduced the idea of implementing a correction, a Hubbard U term, to overcome this shortcoming.

DFT+U explicitly accounts for the on-site Coulomb interactions of the f or d orbital electrons by adding a Hubbard repulsion energy term to the normal DFT energy. The Hubbard parameter is defined as the cost to place two electrons at the same site. This Hubbard parameter [88], in terms of Coulomb energy, can be calculated as follows: $U = E(d^{n+1}) + E(d^{n-1}) - 2E(d^{n})$. Applying such approach to the common LDA functional [87]:

$$E_{LDA+U}[\rho(\vec{r})] = E_{LDA}[\rho(\vec{r})] + E_{Hub}\left[n_{im\sigma}\right] - E_{dc}\left[n_{im\sigma}\right] \tag{2.26}$$

where $n_{im\sigma}$ are the atomic-orbital occupations at site i with quantum number m and spin σ. E_{LDA} also accounts (at least partially, in some averaged way) for the interaction of these electrons, therefore, to prevent double-counting, a double-counting energy term $E_{dc}\left[n_{im\sigma}\right]$ is subtracted. This equation takes the following explicit form:

$$E_{LDA+U} = E_{LDA} + \sum_{i}\left[\frac{1}{2}\sum_{m\sigma\neq m'\sigma'} U\left\langle \hat{n}_{im\sigma}\right\rangle\left\langle \hat{n}_{im'\sigma'}\right\rangle + \frac{1}{2}\sum_{m\sigma\neq m'\sigma'}(U-J)\left\langle \hat{n}_{im\sigma}\right\rangle\left\langle \hat{n}_{im'\sigma'}\right\rangle\right] \tag{2.27}$$

The parameters U and J are the screened on-site Coulomb and exchange interactions which are inputs of the equation. Choosing appropriate values can be done semi-empirically with the help of experimental data or self-consistently. Experimental analysis on the conductivity of the system being modelled can assist in the selection of appropriate Hubbard U values.

2.5.3 Dynamical mean-field theory

DFT+U has shown wide success in modelling strongly correlated systems, and more advanced approaches going beyond DFT are also seeing great progress in recent years. One of the most promising methods is dynamical mean-field theory (DMFT) [89]. Such an approach turns a DFT single particle approach into a quasi-particle one, in which the motion of a single particle is used to capture all of the interactions the particle experiences. To do this, Green's functions are used in which the one electron Green's function is:

$$G(\vec{r},t;\vec{r'},t') = -i\left\langle 0 \middle| T\left[\hat{\psi}(\vec{r},t),\ \hat{\psi}^{\dagger}(\vec{r'},t')\right] \middle| 0 \right\rangle \tag{2.28}$$

where $|0>$ is the ground state wavefunction. T is the time ordering operator in which chronological events inside the square brackets are ordered from right to left. $\hat{\psi}^{\dagger}$ and $\hat{\psi}$ are the electron creation and annihilation operators. Therefore, this function calculates the propagation amplitude of an electron which is created at (r',t') and annihilated at (r,t).

Although such Green's function is adequate to describe one electron, to include interactions we use an Anderson impurity model, outlined in Ref [90–92].

The Green's function for the lattice is

$$G(\vec{k},\omega) = \frac{1}{\omega - \epsilon_{\vec{k}} - \sum(\omega)} \tag{2.29}$$

Being a mean-field theory, this Green function of a lattice site is assumed to be equal to the mean Green function of the overall lattice. In the equation above, we come across $\sum(\omega)$. This term, known as the self-energy, encapsulates all of the effects of electron interactions and links the interacting Green's function G with the non-interacting one G_0 through the following equation: $G^{-1} = G_0^{-1} - \sum$.

In reality, a simple lattice model is not adequate to model real systems, and DFT can actually be incorporated with DMFT to create a DFT+DMFT free energy functional using the local Green's function and the electron density. By minimising this free energy functional, the ground state energy of the system can be found. Such functional is:

$$\Gamma[\rho(\vec{r}), G_{loc}] = T[\rho(\vec{r}), G_{loc}] + \int V_{ext}(\vec{r})\, \rho(\vec{r}) d\vec{r} + E_H + E_{XC}[\rho(\vec{r}), G_{loc}] \tag{2.30}$$

It is worth noticing that the kinetic energy T and exchange correlation E_{xc} do not just depend on the electron's density, as in DFT, but also on the Green's function. A new exchange correlation term is therefore seen in this equation, which adds the DMFT correlation on top of the DFT exchange-correlation term. The details of DFT+DMFT are rather complex and only the basic ideas have been introduced. For more information, please see Ref [93–95].

This DFT+DMFT approach along with other “beyond DFT” models are undergoing fast development and showing promising results, although they are over the scope of the DFT research presented in this thesis.

2.5.4 Non-collinear spin-polarised relativistic DFT

In quantum materials, electronic spin plays a major role in determining their properties. The DFT formalisms presented above allow for spin polarised calculations. The wavefunction can be explicitly written as $\Psi_i(\mathbf{x}) = \phi_i(\vec{r})\chi_i(\sigma)$, with $\Psi_i(\mathbf{x})$ forming a complete spin-orbital which is a function of $\mathbf{x} = (\vec{r}, \sigma)$, whilst $\phi(\vec{r})$ and $\chi(\sigma)$ are only the spatial and spin components of the wavefunction respectively. The Kohn-Sham equations therefore take the form [45]

$$\left(-\frac{1}{2}\nabla^2 + V_{KS}(\mathbf{x})\right)\Psi_i(\mathbf{x}) = \varepsilon_i\Psi_i(\mathbf{x}) \tag{2.31}$$

This approach therefore allows spin to be implemented in our DFT calculations, however, it does not account for spin-orbit coupling effects. Despite not being essential for modelling most materials, spin-orbit coupling is important when working with systems hosting non-collinear magnetic moments, such as quantum-spin liquids. To carry out non-collinear spin-polarised DFT calculations, fully relativistic pseudo-potentials are required. A set of single-particle Dirac-type equations are implemented in the DFT code, referred to as the Dirac-Kohn-Sham equations. Relativistic DFT is a complex topic, branching more into the field of relativistic physics than materials science. Detailed explanations of spin-polarised relativistic DFT and its implementation can be found in Ref [96–99]. From the development of relativistic pseudo-potentials to the implementation of more effective ways to account for relativistic effects, this field of research is still under improvement.

Relativistic DFT is an advancement of DFT currently under implementation in many DFT software packages and results are not as robust as often desired. To this note, it is still under evaluation within CASTEP and therefore sample calculations based on the well known kagome antiferromagnetic metal Mn_3Sn [100] have been carried out. Also, a system closer to the Barlowite kagome frustrated-spin material presented in chapter four is tested, with chemical formula Cu_3O, following a similar structural arrangement as Mn_3Sn. In collaboration with the CASTEP development and visualisation team, non collinear spin calculations have been carried out using fully relativistic pseudopotentials from the CASTEP SOC19 pseudopotential library. A non collinear input spin arrangement has been set to aid these calculations. After the run has been completed, a post-processing visualisation file has been created using the c2x [101] package, in which CASTEP's spin integrals are recalculated, saving the magnetic moments as "forces". These moments are then visualised using the XCrySDen [102] crystalline and molecular structure visualisation program, which presents them as arrows.

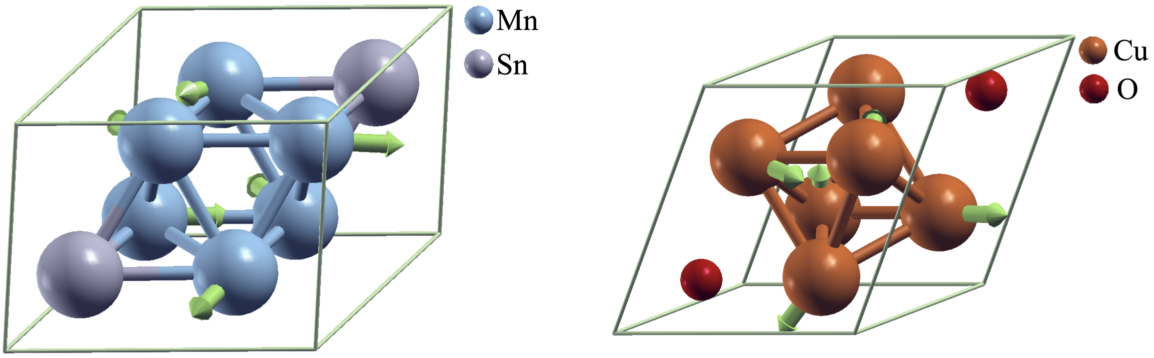

(a) Mn_3Sn

(b) Cu_3O

Figure 2.2: Non collinear spin-polarised relativistic DFT results of Mn_3Sn and Cu_3O. CASTEP 22.11 has been used with the LDA exchange correlation functional and SOC19 relativistic pseudopotentials. The green arrows point along the direction of the magnetic moments around each metal atom.

Non collinear DFT results have been achieved using the LDA exchange correlation functional and SOC19 relativistic pseudopotentials. The magnetic moments in figure 2.2a are mostly coplanar and point towards different directions. This is in agreement with experimental results carried out on Mn_3Sn by Reichlova *et al.* [100] in which magnetic imaging techniques were used based on a laser induced local thermal gradient combined with the detection of the anomalous Nernst effect. The experimental findings have shown that the magnetic moments point either away or towards an adjacent atom, similar to our DFT results. However, no magnetic moment is found to point towards Sn atoms, which is experimentally expected for two Mn moments.

As for Cu_3O, no scientific literature has been found for comparison, however, since the system is in a kagome lattice, non-collinear magnetic moments are expected. This is indeed seen in figure 2.2b, with the spins actually being less co-planar than the Mn_3Sn structure.

These are promising test results, showing that the latest implementations of spin-orbit coupling in CASTEP 22.11 do achieve non-collinear spin textures in an overall good agreement with experiment. This new developments on relativistic DFT will play a key role in the study of frustrated magnetism of chapter 4.

Chapter Three

Exploration of the 2D Metal-Organic Magnet $CrCl_2$(pym)

The work presented in this chapter has been published in the following article:

"Low-Dimensional Metal–Organic Magnets as a Route toward the S=2 Haldane Phase"
Jem Pitcairn, Andrea Iliceto, Laura Cañadillas-Delgado, Oscar Fabelo, Cheng Liu, Christian Balz, Andreas Weilhard, Stephen P. Argent, Andrew J. Morris, and Matthew J. Cliffe.
Journal of the American Chemical Society **2023** 145(3), 1783–1792

3.1 The nature and scope of the research

Coordination frameworks often create low-dimensional structures and can therefore act as a template to search for topological phases of matter, exotic states or quantum-magnetic phases. This is because the weak coupling through relatively large ligands decreases the dimensionality of the material to achieve 1D or 2D quantum phases. This research aims at investigating $CrCl_2(pym)$, a novel quasi-1D S = 2 antiferromagnetic metal organic magnet.

This material is an ideal candidate for recreating the S=2 Haldane phase, which has still not been physically seen in any material. First-principles DFT+U calculations aim at exploring the electronic and magnetic properties of this material. In addition, through the use of appropriate supercells, magnetic exchange pathways involved are investigated.

3.1.1 The Haldane Phase

The Haldane phase is the prototypical example of topological matter and was awarded the Physics Nobel Prize in 2016. It is a topological phase of matter in which a Haldane gap opens due to the breaking of either time-reversal symmetry or inversion symmetry. The Haldane phase requires a system to have an antiferromagnetic nearest neighbour spin arrangement, and for each spin to arise from an even number of unpaired electrons, or in other words, to have integer spins (S=1,2,3...). Famous examples of the S=1 Haldane phase materials are NENP and NINO [103], which have played a key role in the topological materials world. However, only the S=1 Haldane phase has been detected so far because the Haldane gap Δ, the characteristic energy gap in the excitation spectrum of a Haldane phase, decreases significantly relative to the intrachain exchange J_1. For S=1 $\Delta/J_1 = 0.41$ but for S=2 $\Delta/J_1 = 0.087$, making the gap much harder to detect due to the presence of single-ion anisotropy and non-Heisenberg exchange interactions [104].

The Haldane phase can be described using the following magnetic Hamiltonian:

$$H = J \sum_i \left(\vec{S}_i \cdot \vec{S}_{i+1} + D \left(S_i^z \right)^2 \right) \tag{3.1}$$

where J is the Heisenberg exchange and D is the single-ion anisotropy. The ground state of the antiferromagnetic S=1 Haldane phase is a disordered state, which has symmetry-protected fourfold-degenerate edge states caused by the fractional spin excitations [105]. A schematic representation of the S=1 and S=2 antiferromagnetic 1D Haldane system is shown in figure 3.1.

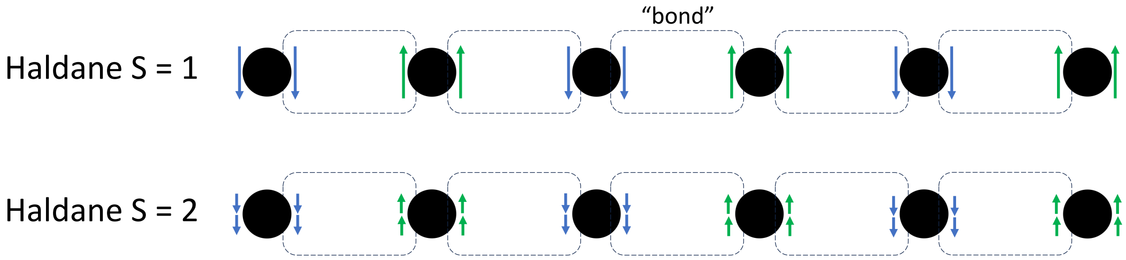

Figure 3.1: Representation of the antiferromagnetic spin arrangements for the S=1 and S=2 Haldane phase. Note that each arrow represents the unpaired S=1/2 electrons giving rise to the net magnetic moment of each atom.

Common to many topological insulators, the edge states are different from the bulk states. It is visible from figure 3.1 that "free" S=1/2 spins appear at each end of the chain. To recreate such an S=2 Haldane system, metal-organic coordination frameworks are a feasible and convenient choice. It has been chosen to use metal-chloride pyrimidine frameworks, with two possible choices of metals containing 4 unpaired electrons to meet the S=2 spin state, either Cr^{2+} or Fe^{2+}. Since iron has a significant spin-orbit component it is not ideal for this goal, and therefore chromium, which has a smaller atomic number and therefore presents weaker spin-orbit coupling [106], has been selected, resulting in the creation of $CrCl_2(pym)$.

3.2 The structure of $CrCl_2$(pym)

The literature on strongly-correlated semiconductors has shown that ligand-centred radicals created by exploiting the redox properties of the transition metal result in strong coupling between the metal and ligand charge [107], which allows for the transfer of spin and charge between metal centres throughout the strongly-correlated metal-organic coordination framework [108]. One very interesting publication by K. S. Pedersen *et al.* [109] has shown that bonding $CrCl_2$ with pyrazine generates $CrCl_2(pyz)_2$ which is a ferromagnet with powerful magnetic coupling between the Cr and (pyz). By replacing the pyrazine with pyrimidine and by carefully adjusting the electronic and magnetic nature of such material, a novel switchable strongly-correlated semiconductor is achieved, holding great technology potential and forming the foundations of this research [107].

This research focuses on a new strongly correlated metal-organic framework $CrCl_2(C_4N_2H_4)$. The material of interest is a metal-organic framework (MOF) made up by a chain of pyrimidine structures linked by metal atoms surrounded by 4 chlorine atoms each, as shown in figure 3.2. Such metal-organic materials are modular, meaning that the pyrimidine structures can be functionalised without altering the overall topology, as the synthesis is ruled by directional coordination bonds [110]. This is a great advantage of strongly-correlated coordination frameworks (SCCFs) over more generic strongly-correlated semiconductors, as the topological nature and electronic interactions cannot be simply decoupled due to the non-directional Coulombic and van der Waals interactions present, posing difficulties in the physical creation of such materials [111, 112].

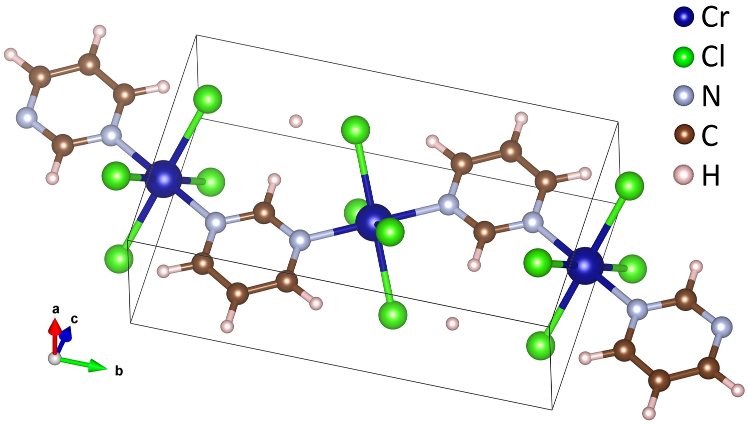

Figure 3.2: Structural visualisation of the $CrCl_2(C_4N_2H_4)$ strongly-correlated metal-organic coordination framework. The structure has been visualised with VESTA [113].

3.3 Achieving an accurate geometry

As this research is computationally based, the structure of the system of interest needs to be representative of reality in order to achieve results applicable to the physical world. A large effort must be placed experimentally to provide a good starting point for the computational simulation. We began by looking at the geometrical nature of $CrCl_2(C_4N_2H_4)$, a 1D chain material synthesised by the Cliffe group, a materials chemistry group at the University of Nottingham. More specifically, to support the computation structural research, Matthew J Cliffe and Jem Pitcairn offered experimental collaboration by physically synthesising the framework by reacting $CrCl_2$ with pyrimidine using vapour diffusion which resulted in the formation of single crystals suitable for X-ray diffraction measurements.

In order to gain a clear experimental understanding of the structure, two types of experimental analysis were carried out by collaborators: a) average structure calculations such as Bragg diffraction, and b) local structure calculations, such as NMR, pair distribution function and Raman. Single crystal X-ray diffraction results showed that the system crystallises in a monoclinic space group $P2_1/m$ with two formula units in the unit cell, as seen in figure 3.2. However, the presence of inaccuracies in experimental structure analysis had to be taken into account. In order to overcome these last, a geometry optimisation was carried out by means of a computational iterative approach, in which the atoms and unit cell parameters are spatially shifted to minimise the total energy of the structure, following the approach previously presented in section 2.4.2 [41].

3.3.1 Simulation parameters and convergence testing

Before starting any type of DFT calculations on a new system, it is essential to find the appropriate number of k-points and the cut-off energy required to accurately model the structure of interest [114]. Convergence testing has been carried out for this purpose.

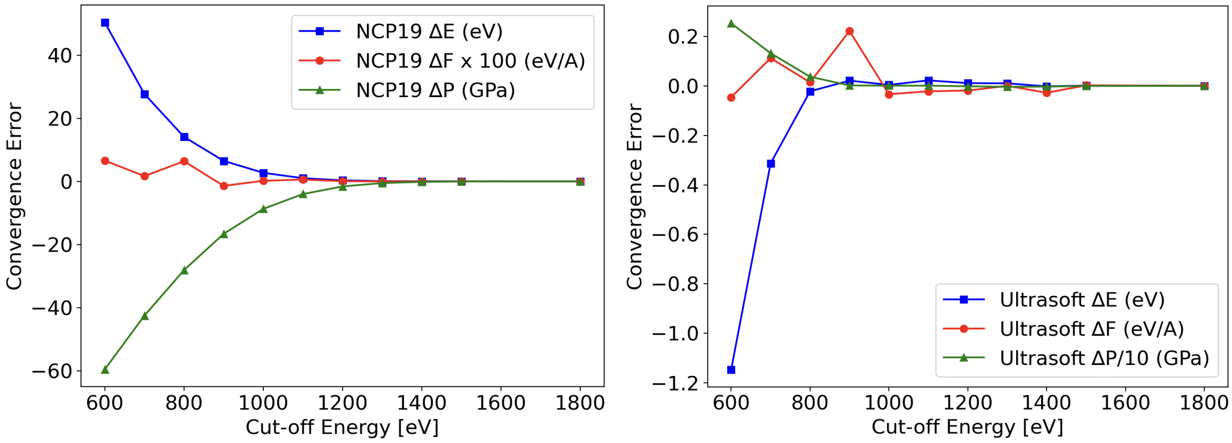

(a) NCP19 pseudo-potentials used

(b) Ultrasoft pseudo-potentials used

Figure 3.3: Cut-off energy convergence testing has been carried out with respect to the following 3 quantities: total energy, forces and pressure. Convergence testing has been done using both norm-conserving (NCP19) pseudo-potentials and ultrasoft pseudo-potentials. A converged value of 1100 eV suitable for both pseudo-potentials has been decided upon.

The choice of pseudo-potential is important as the cut-off energy convergence is directly affected by it. In order to use both generalised gradient approximations functionals (like PBE) and hybrid functionals (like HSE), the choice of using both norm-conserving pseudo-potentials as well as ultrasoft pseudo-potentials has been made [115]. Norm-conserving pseudo-potentials usually need a higher cut-off energy compared to ultrasoft pseudo-potentials. It is important to be able to also use HSE functionals for comparison as PBE tends to underestimate semiconductor band-gaps and usually leads to slightly long bond lengths [116, 117]. Convergence testing results have shown that an appropriate cut-off energy is 1100 eV, suitable for both norm-conserving and ultrasoft pseudo-potentials. Next, k-points convergence testing has been carried out.

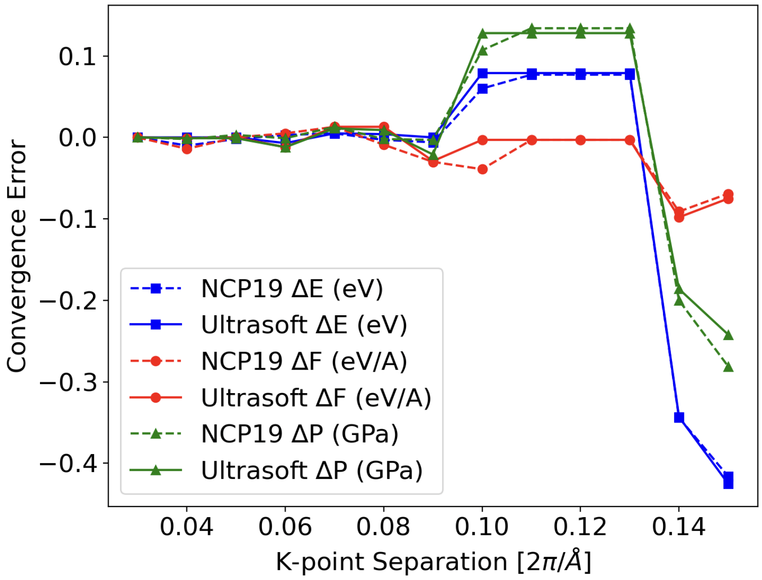

Figure 3.4: K-point spacing convergence testing using norm-conserving (NCP19) pseudo-potentials and ultrasoft pseudo-potentials. The k-point separation refers to the maximum k-point spacing in a Monkhorst-Pack k-point grid. A converged value of 0.05 $2\pi/\text{Å}$ has been selected to be an appropriately converged k-point separation.

As figure 3.4 shows, the convergence of k-points is independent of the pseudo-potential used. Acknowledging the presence of numerical approximations, like basis-set size, integral evaluation cutoffs, numerical approximations, and iterative schemes tolerances, the NCP19 results appear to match with the ultrasoft ones. A k-point spacing of 0.05 $2\pi/\text{Å}$ has been selected to be an appropriately converged k-point separation, and has been used in the calculations throughout the rest of this chapter.

Using an appropriate number of k-points and a suitable cut-off energy is crucial to model the system computationally. However, this specific material poses further issues: common to many 2D strongly-correlated metal-organic coordination frameworks [107], the large distance between the layers, when stacked on top of each other, poses a challenge in DFT calculations as the van der Waals forces between these layers are hard to account for [118]. To overcome this obstacle, van der Waals dispersion corrections are implemented in the DFT code. The many-body dispersion (MBD*) correction of Tkatchenko et al. [65] has been selected as it goes beyond the pairwise-additive treatment of earlier DFT-D methods, in which the n-body contributions to the dispersion energy is taken into account up to the number of atoms, along with the polarisation screening contributions to infinite order [119]. The details of the physics behind this dispersion correction are discussed in section 2.4.1. This DFT-D method is used throughout this computational investigation.

3.3.2 Geometry optimisation

As previously stated, to achieve an accurate cell, the geometry of the system has to be optimised. A computational process is therefore carried out in which the nuclear coordinates and lattice vectors are shifted in order to minimise the total energy of the system [120]. This process works on the fundamental principle that, in nature, atoms are positioned in local energy minima. This is a very powerful approach, allowing the geometry of the lattice to be refined in order to reach a more accurate and stable structure in which the forces between the atoms are minimised and reach equilibrium [121].

As we are dealing with a 1-D chain type structure, the structure stretches along the pyrimidine direction and becomes very large, posing a computational problem. We therefore implement periodic boundary conditions, choosing to include two chromium atoms and two pyrimidine rings in the DFT unit cell. Having two chromium atoms allows to take into account the spin texture of the 1-D MOF, whether to have the chromium atoms in a ferromagnetic (FM) or anti-ferromagnetic (AFM) arrangement along the cell.

Multiple geometry optimisations have been carried out using different parameters. Both ultrasoft and norm-conserving pseudo-potentials have been used. Different Hubbard U values have also been used, as later explained. The results of these geometry optimisation are summarised in table 3.1.

	U Value [eV]	Volume [Å³]	Density [amu/Å³]	Lattice Parameters [Å]			Cell Angles			Integrated |S Density| [ħ/2]	Cr-Cl Bond Lengths [Å]			
				a	b	c	α	β	γ		Cr atom 1		Cr atom 2	
Experimental		312.75	1.30	3.67	12.10	7.06	90.0	94.2	90.0		2.40	2.76	2.40	2.76
Ultrasoft Pseudo-potential	0	297.68	1.36	3.53	11.87	7.10	90.0	88.7	89.6	7.9	2.56	2.40	2.61	2.38
	2	312.45	1.30	3.72	12.05	7.03	90.0	97.2	89.6	8.7	2.39	2.87	2.40	2.86
	3	313.33	1.30	3.73	12.10	7.00	90.0	97.4	89.5	8.7	2.41	2.87	2.42	2.86
	4	316.06	1.28	3.77	12.10	6.97	90.0	97.5	89.5	8.8	2.42	2.88	2.42	2.88
Norm Conserving Pseudo-potential	0	255.35	1.59	3.24	11.75	6.70	90.0	91.0	89.9	7.3	2.38	2.39	2.40	2.38
	3	272.08	1.49	3.46	11.90	6.64	89.9	97.8	89.7	8.7	2.39	2.73	2.40	2.72
	4	272.03	1.49	3.47	11.90	6.64	89.9	97.8	89.7	8.7	2.40	2.73	2.40	2.73
	5	273.86	1.48	3.47	11.90	6.68	89.8	97.8	89.7	8.8	2.40	2.75	2.41	2.75
	6	275.83	1.47	3.50	12.00	6.65	89.9	98.2	89.7	8.9	2.42	2.76	2.43	2.76
	10	283.03	1.43	3.53	12.10	6.72	89.9	98.6	89.8	9.3	2.46	2.82	2.47	2.82

Table 3.1: Summary of PBE+U+MBD* geometry optimisation results using two different pseudo-potentials and a range of Hubbard U values. Ultrasoft pseudo-potentials have been used as well as NCP19 Vanderbilt (ONCVPSP) "on-the-fly" optimised norm-conserving pseudo-potentials. A cut-off energy of 1100 eV has been used with a k-point spacing of 0.05 $2\pi/\text{Å}$ and a Gaussian smearing scheme with a 0.2 eV smearing width. The Broyden density-mixing scheme has been used throughout the optimisations.

Starting by analysing the results where no Hubbard U correction is present (where U = 0 eV), table 3.1 shows that the volume and density of the experimental cell matches better with the ultrasoft pseudo-potentials optimisation. Looking at the optimised lattice parameters, an 8.95% length difference is seen along the *a* direction between the ultrasoft optimised structure and the norm-conserving optimised structure. This is unexpected, as the mere selection of pseudo-potentials should not bring such discrepancies. When comparing the ultrasoft and the norm-conserving optimised structures, the norm-conserving one deviates the most from the experimental results in terms of lattice parameters, volume and density. As shown in figure 3.3, a higher cut-off energy is needed for norm-conserving pseudo-potentials. This could suggest that the calculations are not fully converged. At 1100eV, forces present a convergence error of 6×10^{-3} eV/Å. Such an error is relatively small and is unlikely the cause of the discrepancies presented in the optimised structures, however, no other obvious reason has been found for this odd behaviour.

The bond lengths between the two Cr atoms with the Cl ions surrounding each atom does not match in either case, as the structures lost their tilt in the beta direction and became much more symmetrical. This is a problem, since this MOF is expected to have a spatially degenerate electronic ground state which will therefore lead to a geometrical distortion that removes that degeneracy [16], resulting in the Jahn-Teller effect [122]. The two geometry optimisations so far examined are therefore not capturing this physics of the system, and therefore further corrections must be introduced in the DFT inputs. In order to attain the Jahn-Teller effect, a Hubbard U [123] correction must be included in the geometry optimisation, as explained in the following section.

3.3.3 The Jahn-Teller effect and Hubbard U correction

As previously explored in chapter 1, the Jahn-Teller effect is a geometric distortion of a non-linear molecular system, such as the one we are dealing with, that reduces its overall symmetry and lowers its energy [122]. This effect is directly dependent upon the electronic state of this MOF, and causes each Cr atom to have two long bonds and two short bonds with the four Cl atoms surrounding it. This distortion of the chromium octahedra is common in octahedral complexes [124], and is an essential property to capture in our optimised cell. In order to do this, a Hubbard U correction is needed [125]. This comes as no surprise, since we are dealing with strongly correlated materials with partially filled d orbitals [107].

As explained in more detail in chapter 2, DFT+U adds a Hubbard-like term to the on-site Coulomb interactions of the localised electrons [123]. This is because the localised orbitals in the band-gap, in our case the localised d-states, are incorrectly calculated to be too close to the Fermi level. The Hubbard U correction moves these states away from the Fermi energy. In other words, a Hubbard term is added to the Hamiltonian in order to account for the on-site Coulomb interactions of these d-orbital electrons, resulting in a more accurate band gap and preventing the inaccurate delocalisation of these electrons [126].

DFT+U geometry optimisations have been carried out for a U value between 2 eV to 10 eV. Hubbard U values above 5 eV are out of the expected range of a suitable U correction for this material, however, they have been included to achieve a more comprehensive understanding. These results have been included in table 3.1, and one can notice how the effect of Hubbard U increases the volume of the cell and therefore decreases its density. Comparing the different geometry optimisations, the closest ones to experimental results in terms of volume and density are the ultrasoft DFT+U calculations with a Hubbard U correction of U = 2 eV to 3 eV. This is in agreement with other studies that suggested to use a U of 2.1 eV [127] and 3.5 eV [128] for similar systems.

Adding a Hubbard U correction in the geometry optimisation process has resulted in optimised structures which successfully show the presence of Jahn-Teller distortions. The geometry optimisations using norm-conserving pseudo-potentials result in structures which are in closer agreement with the experimental Cr-Cl bond lengths, with the stretched Cr-Cl bond presenting only a 0.01Å difference for U = 5 eV, resulting in almost a perfect match. This cell, however, presents a large volume difference with the experimental cell of -12.4%, far too large to be acceptable.

In conclusion, the best geometry optimised structure has been achieved using ultrasoft pseudopotentials with a Hubbard U correction of U=3eV. This structure exhibits the Jahn-Teller effect with the stretched Cr-Cl bond showing a relatively small 4.0% bond length difference compared to the experimental cell, but most importantly, the volume matches very well with the experimental cell with only a 0.19% difference and the density is found to be the same at this level of accuracy. The lattice parameters and cell angles found using ultrasoft pseudopotentials also match better with the experimental cell compared to the norm-conserving results. This best optimised structure has been used for the remained of this research.

3.4 Investigating electronic and magnetic properties

After having achieved a geometry optimised unit cell, the electronic and magnetic properties of this material can be explored. To this goal, the science behind the electron arrangement in this MOF must be investigated.

In our crystal system, chromium is coordinated by four Cl^- ligands and two N atoms from the pyrimidine ligands, which forms a distorted $CrCl_4N_2$ octahedron. Chromium, with an electron configuration of [Ar] $3d^5 4s^1$, is a transition metal normally containing 24 electrons, however, the presence of the Jahn-Teller distortion in the chromium octahedra suggests that we are dealing with Cr^{2+} ion [129]. This can be inferred since the high spin state electron configuration of Cr^{2+} is non symmetrical, as later explained and depicted in figure 3.5. Having a non symmetrical spin system causes the elongation along one of the directions of the crystal referred as the Jahn-Teller distortion [130]. Note that if chromium was either not oxidised and had its 24 original electrons or only lost one electron, the $4s^1$ electron, the d-orbital would be symmetrically filled and no Jahn-Teller distortion would be seen.

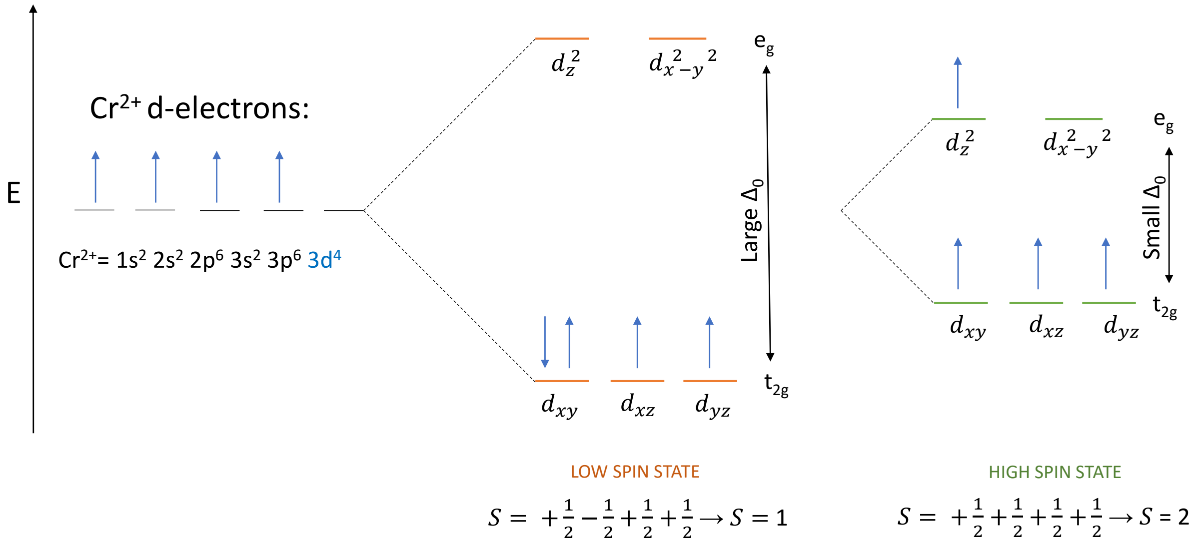

Figure 3.5: Diagram of crystal field splitting in octahedral complexes for Cr^{2+}

The Cr^{2+} oxidation state is in agreement with single crystal x-ray diffraction results and powder x-ray diffraction after a 1-month exposure to air. These experimental results have been measured by experimental collaborators and their analysis and interpretation is beyond the scope of this research.

3.4.1 Crystal field splitting and spin states

After having concluded that our central metal ion is in the 2+ oxidation state, the electronic configuration for this ion is simply $Cr^{2+} : [Ar]3d^4$. When the ligands approach the chromium ions, the degeneracy of the chromium's d-subshell is broken because of the static electric field. The d-electrons found closer to the ligands will reach a higher energy since they would naturally repel and, therefore, splitting of the d-orbital is seen [131]. This splitting is affected by the period of the metal ion, 4 in our case, the charge of the metal ion, 2+ in our case, and the field strength of the complex's ligands [132].

CASTEP has been used to computationally explore these theoretical notions. Table 3.2 shows that the difference in number of spin up and down electrons is very close to the theoretical result of 4. Since electrons are fermions with a spin = 1/2 each, we are expecting a net spin of S=2 in the high spin state. With this said, looking at the individual electron occupancies in the d-suborbitals makes less sense, as CASTEP is projecting the electron density onto these non-eigenstates [41]. It would be more accurate to use Kohn–Sham states, but even by doing so the Kohn–Sham equations describe fictitious non-interacting particles, letting the Exchange-Correlation functional deal with the quantum mechanical correlation effects [133]. More advanced approaches such as dynamical mean-field theory[93] offer better solutions to account for correlations and may lead to more accurate projections onto the d-states, which could be an extension to this research.

D Orbitals		Cr$_1$ d-electron occupancies		Cr$_2$ d-electron occupancies	
		Spin Up	Spin Down	Spin Up	Spin Down
e$_g$	d_{z^2}	0.983	0.017	0.982	0.018
	$d_{x^2-y^2}$	0.793	0.063	0.797	0.063
t$_{2g}$	d_{xy}	0.943	0.032	0.942	0.031
	d_{xz}	0.900	0.063	0.898	0.064
	d_{yz}	0.630	0.092	0.630	0.094
Net electrons (Up-Down)		3.98 e$^-$		3.98 e$^-$	
Spin:		~2		~2	

Table 3.2: DFT results for the high spin state d-electron occupancies for each of the two chromium ions in $CrCl_2(pym)$. As can be seen, a spin of 2 is seen, correctly matching theoretical expectations for Cr^{2+}.

3.4.2 Band structure and density of states

In order to gain an insight on the behaviour of the electrons of the system, the band-structure and density of states have been calculated. As previously explained in section 1.2.1, the electron correlations are driving many of the properties observed in strongly correlated systems, and these are not easily captures by DFT, hence, this representation has limitations. However, band-structure and density of state calculations still offer an excellent model with respect to many physical properties, including electrical conductivity and optical absorption. The path along the cell chosen for the band structure calculation is shown in figure 3.6. The high symmetry points of the unit cell have been included in this path.

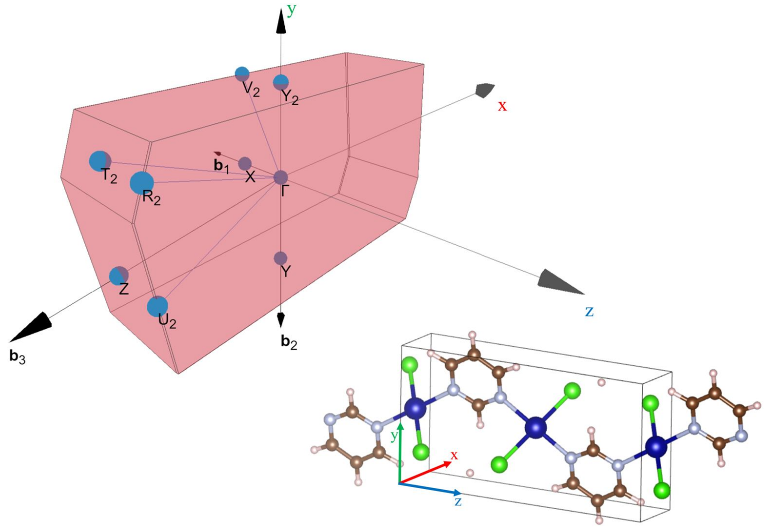

Figure 3.6: Visualisation of k-point path taken to calculate the band structure of $CrCl_2(pym)$, incorporating its high symmetry points. The selected path is: $\Gamma - X;\ Y - \Gamma - Z;\ R_2 - \ \Gamma - T_2;\ U_2 - \ \Gamma - V_2$. Image generated using SeeK-path [134].

The electronic band structure and projected density of states have been calculated using two different functionals, PBE and HSE06, along with a Hubbard U correction of 3 eV. Results have been presented in figure 3.7.

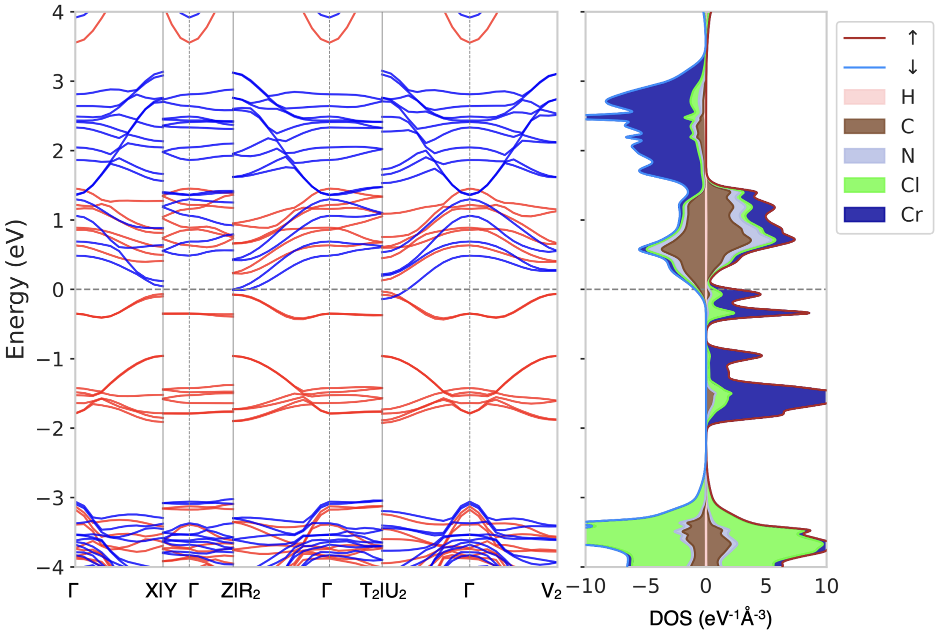

(a) FM PBE

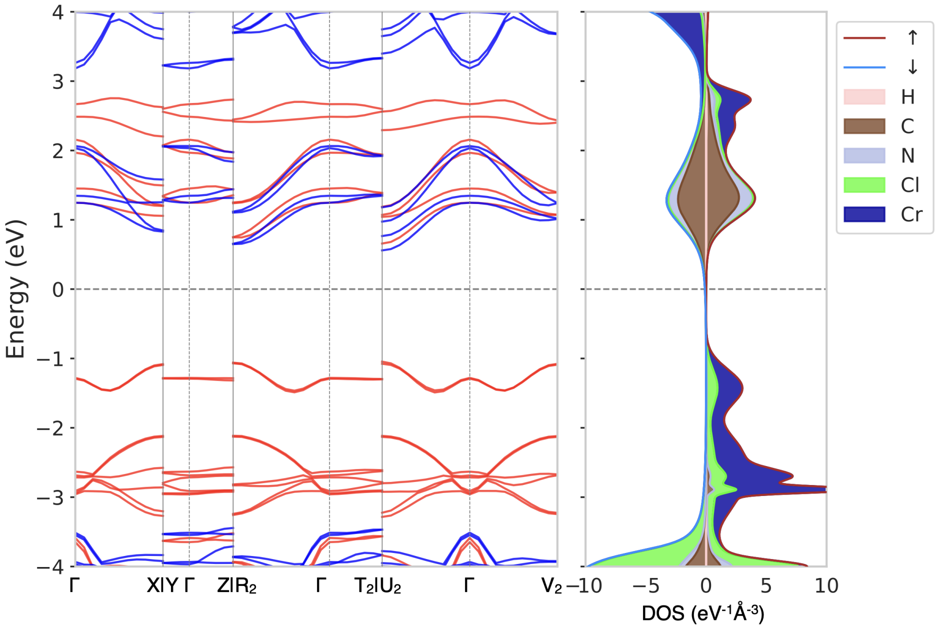

(b) FM HSE

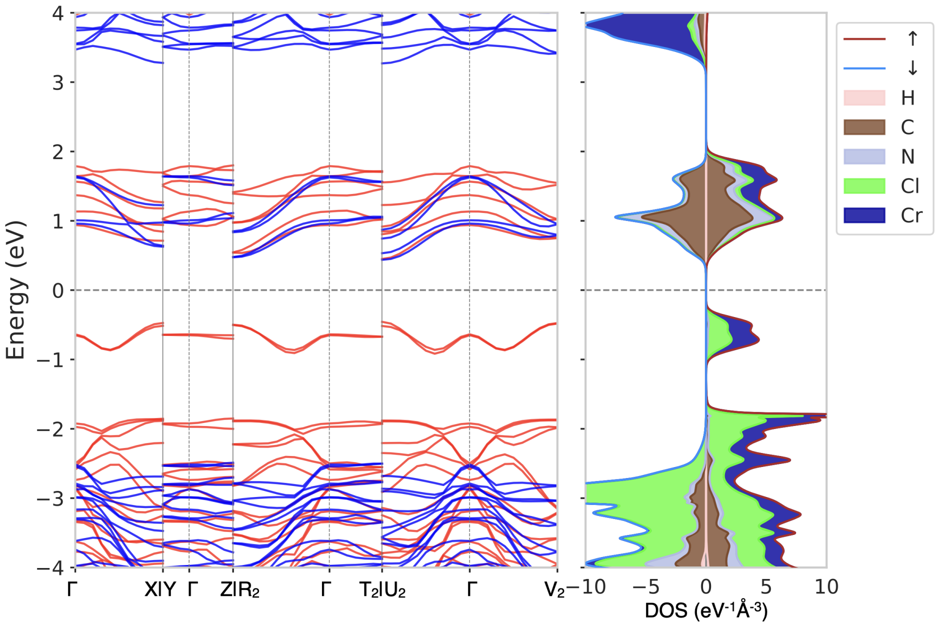

(c) FM PBE + U (U = 3 eV)

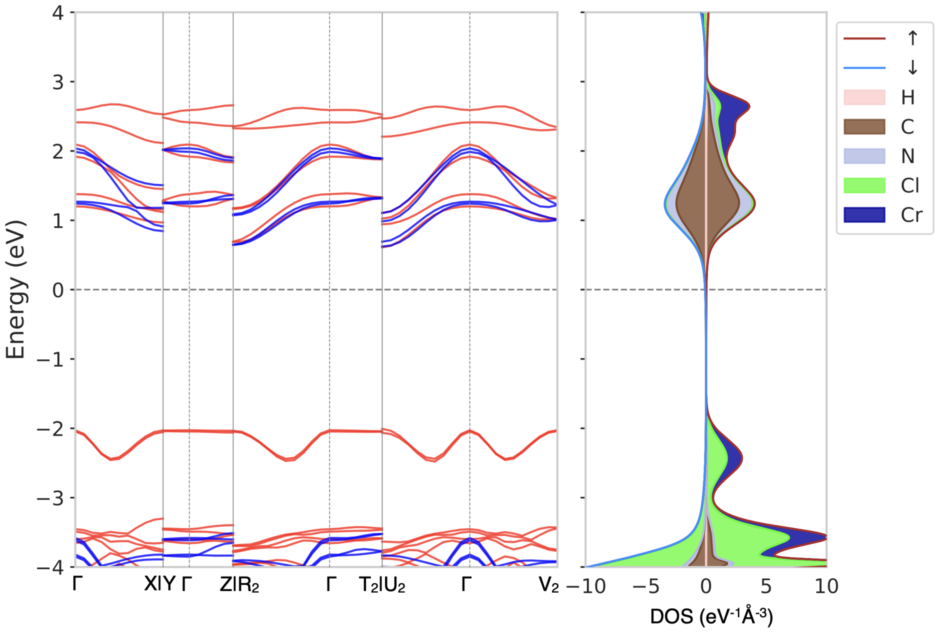

(d) FM HSE+U (U=3eV)

Figure 3.7: Band structure and density of states of $CrCl_2(pym)$ for the ferromagnetic configuration. The Fermi energy has been placed at the origin and is shown by the dashed line. The projected density of states has been decomposed onto the respective atomic species.

Comparing these graphs, it is easy to see that the overall shapes of the bands are relatively similar, but the bands are found at different energies with respect to the Fermi energy placed at the origin. PBE, being a GGA functional, tends to underestimate the band gap. Being aware of this problem, calculations have been carried out using the HSE06 functional which, being a non-local exchange-correlation functional, does not experience the same band-gap issues as PBE. HSE06 is a hybrid functional based on a screened Coulomb potential [135]. Such a functional is expected to find a more accurate band-gap compared to PBE by implementing a more correct treatment of the quantum mechanical exchange interactions, although it is more computationally expensive. However, provided the inclusion of a Hubbard U correction, PBE can also perform adequately well when applied to such systems, suggesting that HSE is not of great necessity. Ideally both the exchange and correlation parts of the exchange-correlation functional are as accurate as they can be, but adding a Hubbard U to alter the correlation interactions can indirectly compensate for the lower accuracy exchange interactions.

As previously mentioned, hybrid functionals like HSE06 are significantly more computationally expensive. This resulted in carrying out HSE calculations using only 1 k-point to sample the Brillouin zone. This means that, unfortunately, the HSE results are not fully converged. Also, finding a convergence error would require the use of more k-points, which is not feasible given the available computational resources, hence the error is unknown. However, the cut-off energy of 1100 eV has not been decreased and has been shown to be converged even when using the HSE06 functional. Being aware of these factors, the HSE results have still been presented as they act as a valuable comparison to the better converged PBE results.

Comparing the band structure of figures 3.7a and 3.7c and of figures 3.7b and figure 3.7d, it is clear that the Hubbard U correction is opening up the band gap as theoretically expected [136]. Furthermore, comparing the PBE and HSE density of states, the HSE PDOS shows a smoother contour. This must not be confused with any property of the material, since this effect is merely caused by the use of fewer k-points for HSE calculations due to their computationally expensive nature.

The presence of dispersion along $U_2 - \Gamma - V_2$ can be inferred from the curvature of the spin up band just below the Fermi level, while it is more localised in the $Y - \Gamma - Z$ region as it appears more flat. Overall, band structure suggests that the material exhibits semiconducting characteristics, with a band gap of around 1.2 eV when a Hubbard U correction of 3 eV is used. The semiconducting nature comes from the electrons belonging to one spin, say the spin-up electrons, while a large gap of 3.3 eV is present for the other spin electrons. The large energy difference between the spin up and spin down bands demonstrates that such material is ferromagnetic and suggests the likely possibility that the system would be able to offer spin-polarised carriers [137] when exposed to thermal, optical or electrical gating excitations [138, 139]. Furthermore, the projected density of states (PDOS) suggests that the nature of the conducting electrons around the Fermi level are Cr and Cl based, meaning that the organic linker (pym) is not directly involved in the conduction band.

Although higher in energy, the anti-ferromagnetic configuration can also be explored and presents slightly different characteristics, as shown in figure 3.8. Still, a semiconducting nature is characteristic of the material also with a band gap around 1.2 eV, however, as the spin up and down bands overlap, no distinction exists between the spin type in regard to conductivity. An interesting characteristic when comparing the FM and AFM DOS is their similarity. The organic linker components are again seen above the Fermi level and the down spin channel has moved up to match the spin up conduction band, just below the Fermi energy.

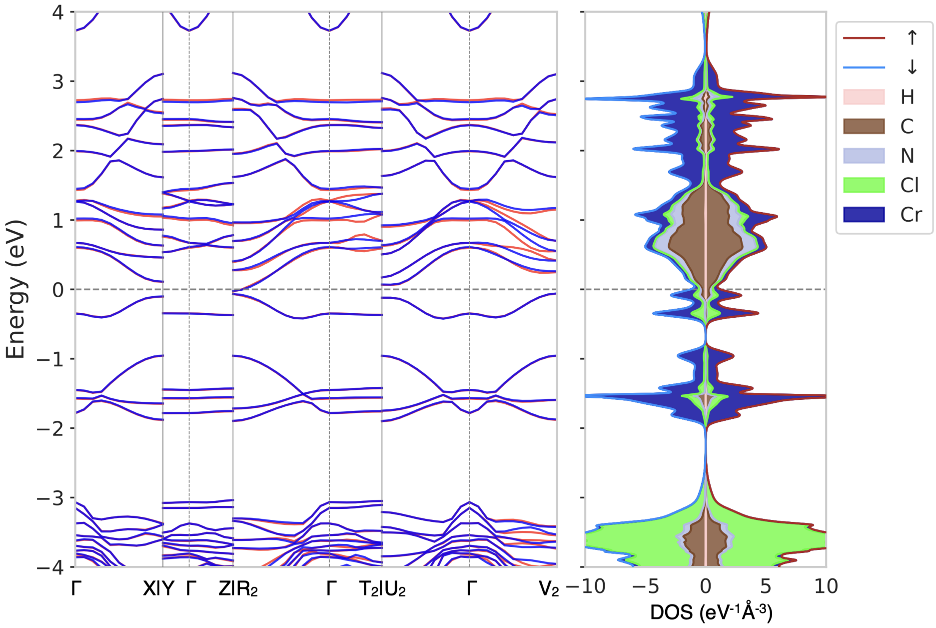

(a) AFM PBE

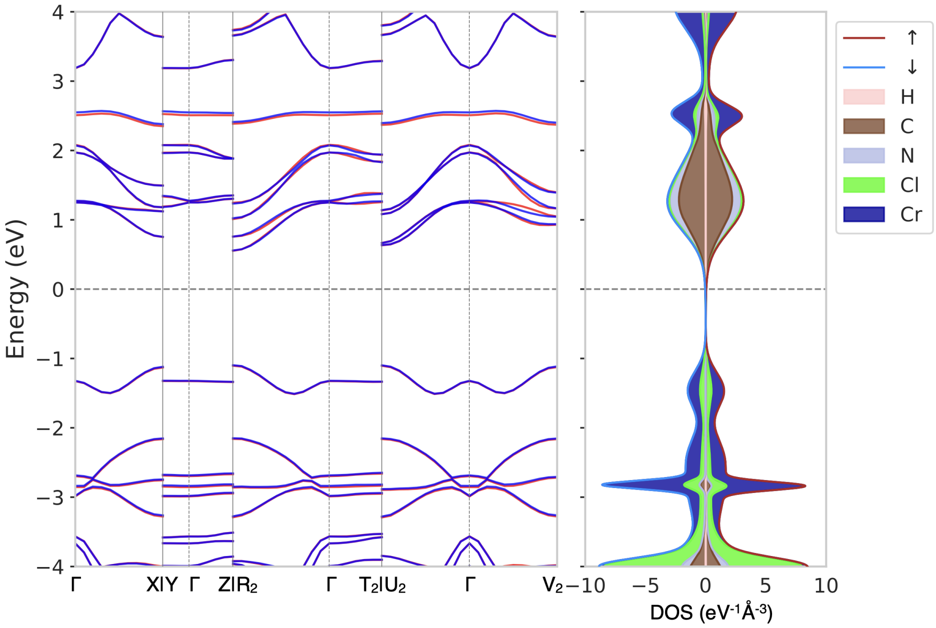

(b) AFM HSE

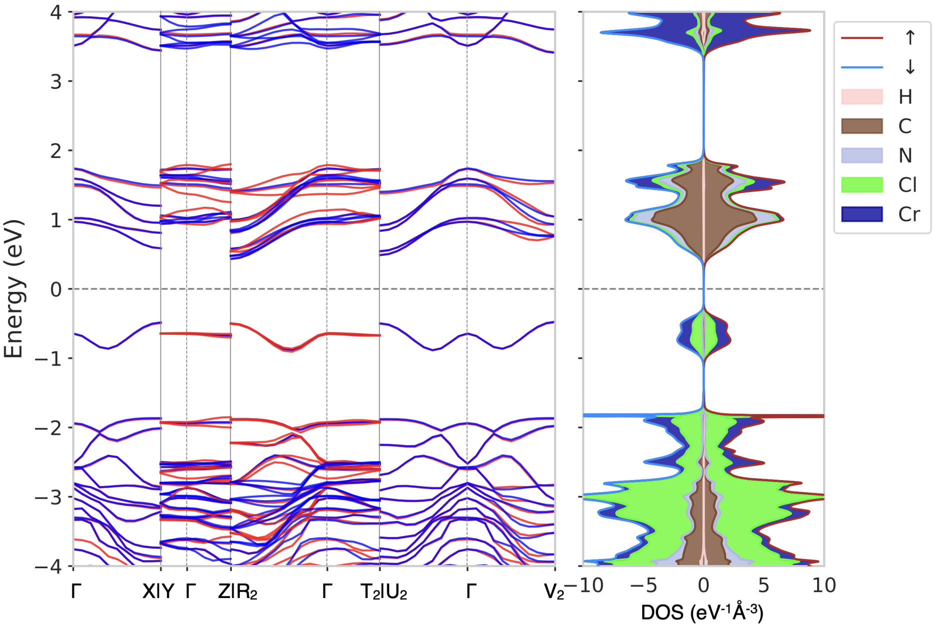

(c) AFM PBE + U (U = 3 eV)

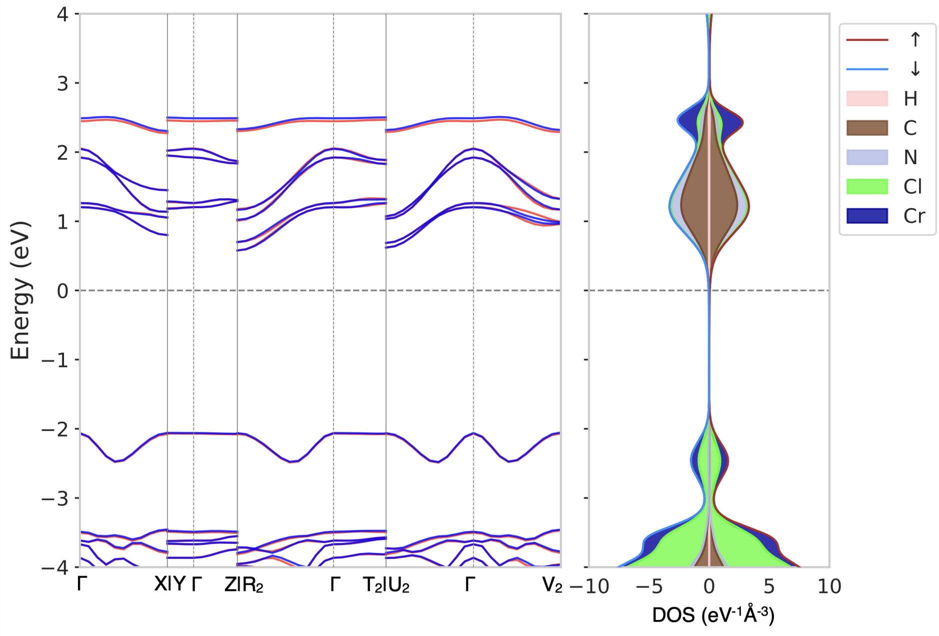

(d) AFM HSE+U (U=3eV)

Figure 3.8: Band structure and density of states of $CrCl_2(pym)$ for the anti-ferromagnetic configuration.

Although this AFM configuration is 1.88 meV higher in energy when comparing the PBE U = 3 eV results, meaning that such system actually exhibits a ferromagnetic nature, the magnetic relations with Cr ions of adjacent layers in the bulk material have not been explored. This type of coordination framework forms, in nature, a 3D structure, with layers of chromium atoms stacked on top of each other and connected via the chlorides. These layers are adjacent to other identical ones, as shown in figure 3.9. In order to analyse magnetism on this larger scale, a $2 \times 2 \times 1$ supercell of the original structure has been developed. This is essential in order to increase the degree of freedom in regards to magnetism. Working with a unit cell containing two Cr^{2+} ions can only be used to model ferromagnetic or antiferromagnetic configurations along the direction of these two chromium ions. Different magnetic configuration in the different directions cannot be modelled. A supercell overcomes this problem, as seen in the next section.

3.5 Magnetic exchange

As introduced in chapter 1, different types of magnetic exchange interaction exist. Let us now focus on the superexchange interactions [140], which refer to strong coupling between two next-to-nearest neighbour cations, Cr in our case, through a non-magnetic anion, like Cl or the pyrimidine [141]. Superexchange has not been traditionally explored in nitrogen heterocycle halides. Heterocycle halides are cyclic compounds which contain atoms from at least two different elements in the organic ring, C and N in our case, combined with a halide, Cl in our case. However, our system comes with large organic linkers that offer long, weak superexchange pathways between the Cr ions at low temperature. From heat capacity experimental results carried out by experimental collaborators, a temperature of $T_N = 20.0(3)K$ has been found to bring the system into a Néel ground state with long-range magnetic order. This experimental result demonstrated that the framework exhibits significant magnetic low dimensionality [142, 143].

To examine the magnetic exchange computationally, a $2 \times 2 \times 1$ supercell has been made to include the exchange directions of interest. The three shortest Cr-Cr distances represent the three exchange directions: J_1 along the chloride bridge, J_2 through the pym ligand and J_3 between layers.

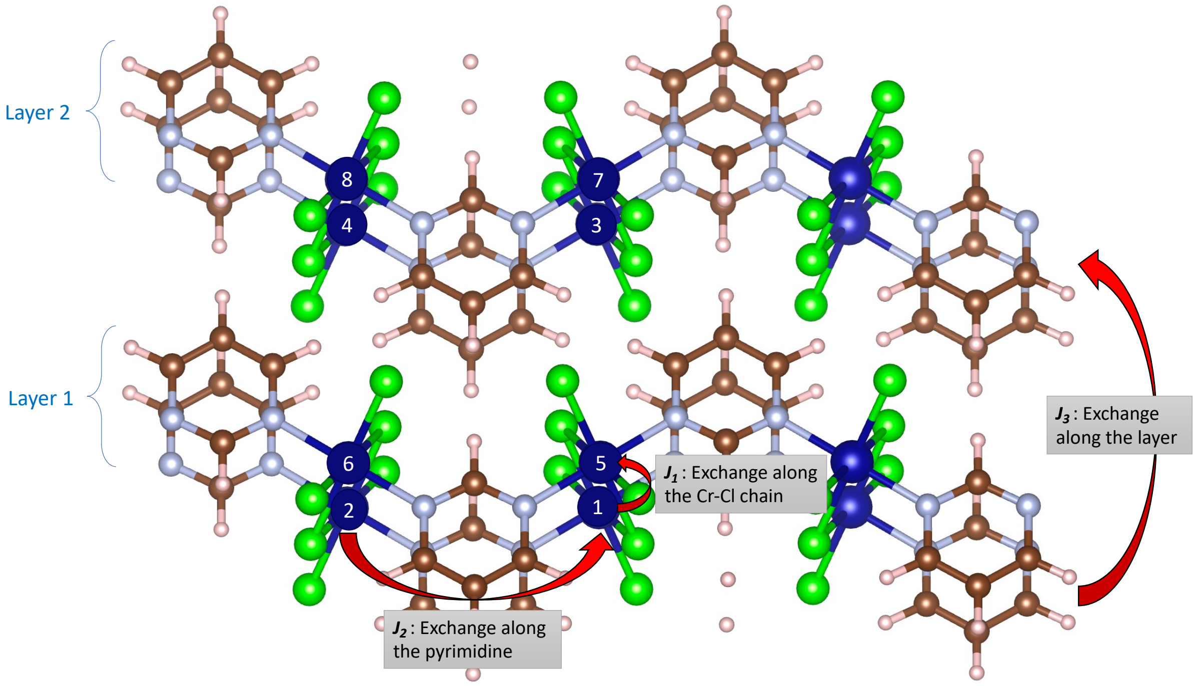

Figure 3.9: Visualisation of the super-cell that has been used to investigate the exchange interactions. These exchange interactions have been calculated along the chromium direction, chloride direction and layer direction, as well as their combinations. Chromium atoms have been numbered for reference purposes when interpreting table 3.3.

The J_n consist of the Heisenberg exchange energy for the three nearest neighbours and are a self-consistent set of the exchange interactions. Using symmetry, a set of 8 different spin configurations were used to calculate the J_n values along the three different directions. Table 3.3 presents these 8 FM or AFM configurations, covering the possible combinations that J_1, J_2 and J_3 could have.

Spin on each Cr^{2+}								Magnetic Exchange		
Cr 1	Cr 2	Cr 3	Cr 4	Cr 5	Cr 6	Cr 7	Cr 8	J_1	J_2	J_3
up	up	up	up	up	up	up	up	FM	FM	FM
up	down	down	up	down	up	up	down	AFM	AFM	AFM
up	down	up	down	up	down	up	down	FM	AFM	FM
up	up	up	up	down	down	down	down	AFM	FM	FM
up	up	down	down	up	up	down	down	FM	FM	AFM
up	down	up	down	down	up	down	up	AFM	AFM	FM
up	down	down	up	up	down	down	up	FM	AFM	AFM
up	up	down	down	down	down	up	up	AFM	FM	AFM

Table 3.3: Report of the 8 different Cr spin configurations implemented on the supercell, used to calculate magnetic exchange interactions. Each row represents each configuration.

DFT+U was used to calculate the ground state energy of each configuration at different U values and a multidimensional linear regression was used to fit these energies.

$$E = \sum_{n=1}^{3} J_n \, s_n + fit\; constant \tag{3.2}$$

Equation 3.2 was used to fit the energies of the 8 different configurations to output the magnetic exchange values along the three different J_n directions. For a given configuration, the E term represents the energy difference between the given configuration and the lowest energy one. The s_n term represents the nature of the exchange interaction along that J_n direction, which can be either 1 (for AFM) or 0 (for FM) as we are carrying out collinear spin-polarised DFT calculations. Along each of the three J_n directions, each of the three s_n terms can therefore be described by $s_n = \vec{s}_i \cdot \vec{s}_{i+1}$, with positions i and $i+1$ being nearest-neighbours, following a Heisenberg model approach as explained in section 1.2.5.

The results are compared with the experimental ones. Inelastic neutron scattering was carried out by our experimental collaborators on a powder sample at 1.7 K and 25 K. Both computational and experimental results are shown in figure 3.10.

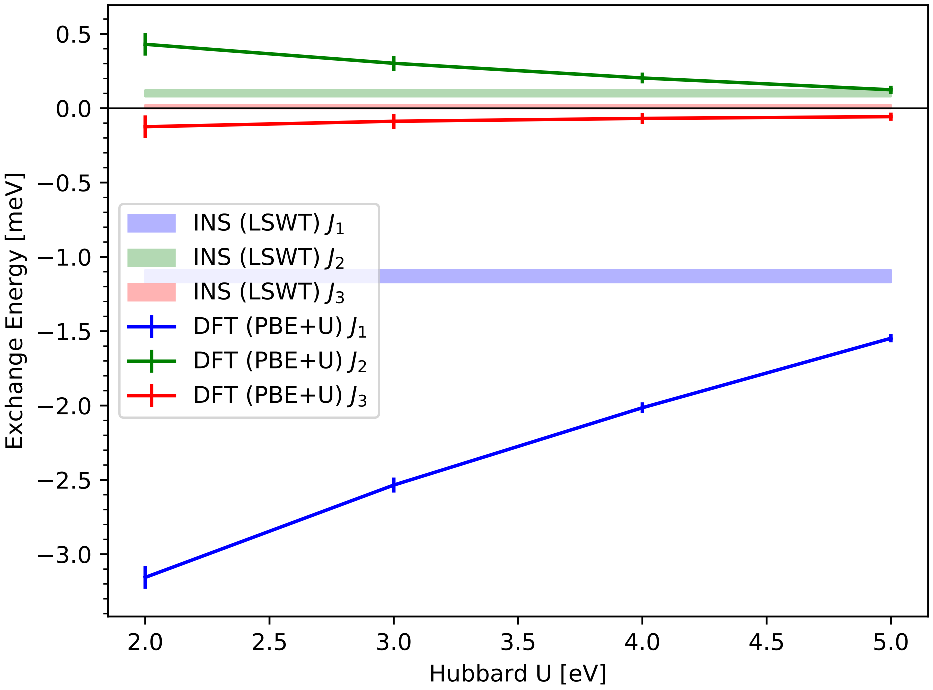

Figure 3.10: Magnetic exchange interactions J_n along the three shortest Cr-Cr distances with respect to the Hubbard U value. The figure presents both the DFT results calculated with PBE+U and MBD*, as well as the powder inelastic neutron spectroscopy (INS) experimental results fitted using linear spin wave theory (LSWT).

When comparing experimental data with DFT results, it is essential to keep in mind that that DFT carries out calculations on static crystals (at 0 K). This may account for some DFT and experimental differences seen in figure 3.10, along with the presence of computational and experimental errors. For instance, structural inaccuracies may be present both computationally and experimentally. In fact, structural inaccuracies can arise computationally during the geometry optimisation process, for instance by using GGA functionals which often lead to slightly long bond lengths as previously explained. Experimentally, the grown crystals may have defects, which have not been taken into account in DFT calculations.

With a Hubbard U of $U = 3$ eV, the J_n interactions are $\mathrm{J}_1 = -2.53\,\mathrm{meV}$, $\mathrm{J}_2 = 0.30\,\mathrm{meV}$, $\mathrm{J}_3 = -0.09\,\mathrm{meV}$. When compared to experimental results, the J_2 and J_3 exchange energies are in good qualitative agreement, while a greater discrepancy is found in J_1. The experimental values are $\mathrm{J}_1 = -1.13(4)\,\mathrm{meV}$, $\mathrm{J}_2 = 0.10(2)\,\mathrm{meV}$, $\mathrm{J}_3 = 0.01(0)\,\mathrm{meV}$. As Hubbard U is increased, DFT results tend to approach the experimental ones in the tested range, since J_n of smaller magnitude were calculated experimentally. Hubbard U makes the system more localised, causing the exchange energy to tend towards.

The sign of the exchange interactions suggests the nature of the interaction being ferromagnetic (positive) or antiferromagnetic (negative). It is therefore very easy to tell that J_1 is AFM while J_2 is FM. J_3 is very close to zero and results between experiment and DFT do not agree. However, further experimental investigations were carried out to test this discrepancy and the ground state determined by powder neutron scattering confirms a FM arrangement. Moreover, the ratio $J_1/J_2 = 8.4$ for our DFT results is close to $J_1/J_2 = 11(2)$ of our experimental results. These values are near the conventional "threshold" value of $J_1/J_2 \geq 10$, suggesting that the system is approaching the quasi-one-dimensional limit [144]. This is because the magnetic interactions mainly appear in the J_1 direction, clearly prevailing over the others, therefore primarily being one-dimensional. This approaches the regime in which the physics of the material is well described by a 1D Hamiltonian, and is therefore considered quasi-one-dimensional [145].

3.5.1 Exploring the supercell's electronic nature

The band structure and density of states of the supercell have been calculated and shown in figure 3.11. As expected, an antiferromagnetic nature is seen, as the up spin channel is symmetrical with the spin down. This is in agreement with the AFM J_1 being the dominant term and prevailing over the others. Figure 3.11 has been calculated using the full magnetic ground-state of the system, with AFM J_1 and FM J_2 and J_3. This was not possible using smaller calculation cells, hence previous band-structure results may be less accurate.

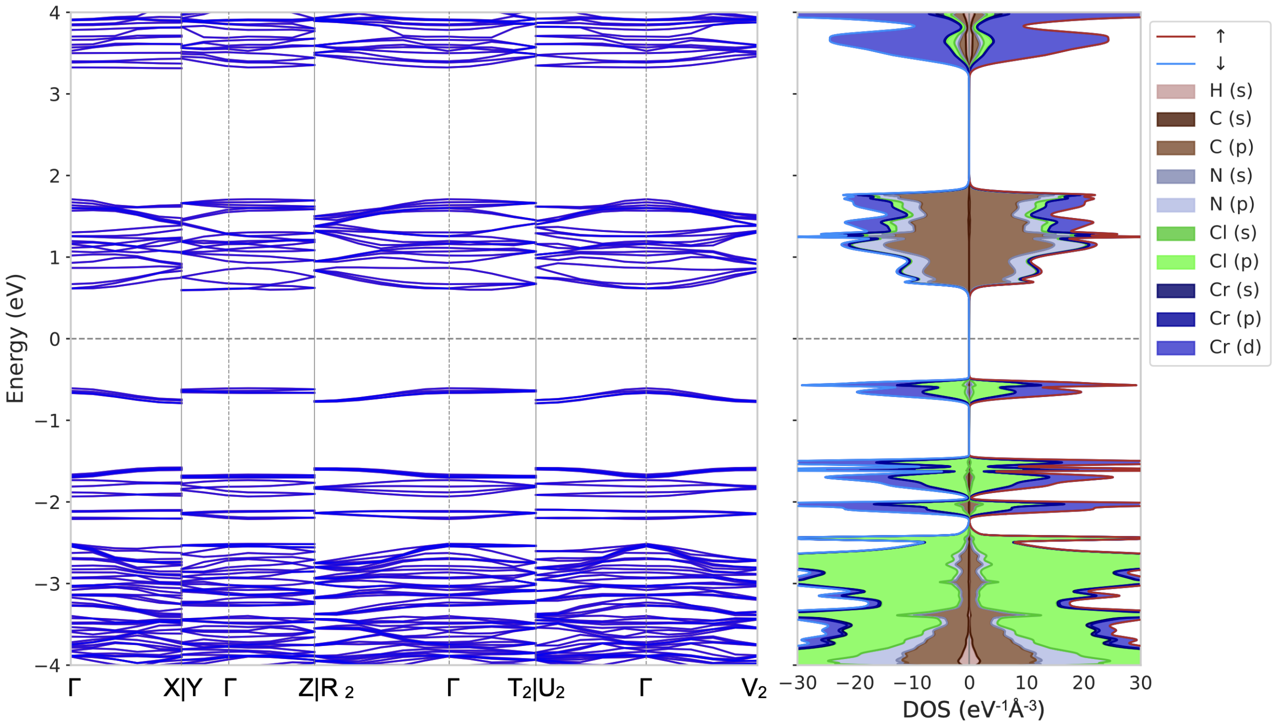

Figure 3.11: PBE+U+MBD* (U=3eV) electronic band structure and projected density of states of the $2 \times 2 \times 1$ supercell. The Fermi energy has been placed at the origin and is shown by the dashed line. The projected density of states has been decomposed onto the atomic species and their respective angular momentum channels.

As expected, the overall behaviour is similar to the unit cell band structures and density of states, with the Cr and Cl ions forming the highest occupied crystal orbitals, while the (pym) is involved in the lowest unoccupied crystal orbitals. As shown in figure 3.11, a band gap of ~ 1.2 eV is present.

To further examine the science of this framework and to gain a clearer understanding into the nature of the electron configuration of the system, the Kohn-Sham orbitals have been calculated and visualised. The highest occupied crystal band and lowest unoccupied crystal band have been calculated at the Gamma point and presented in figure 3.12.

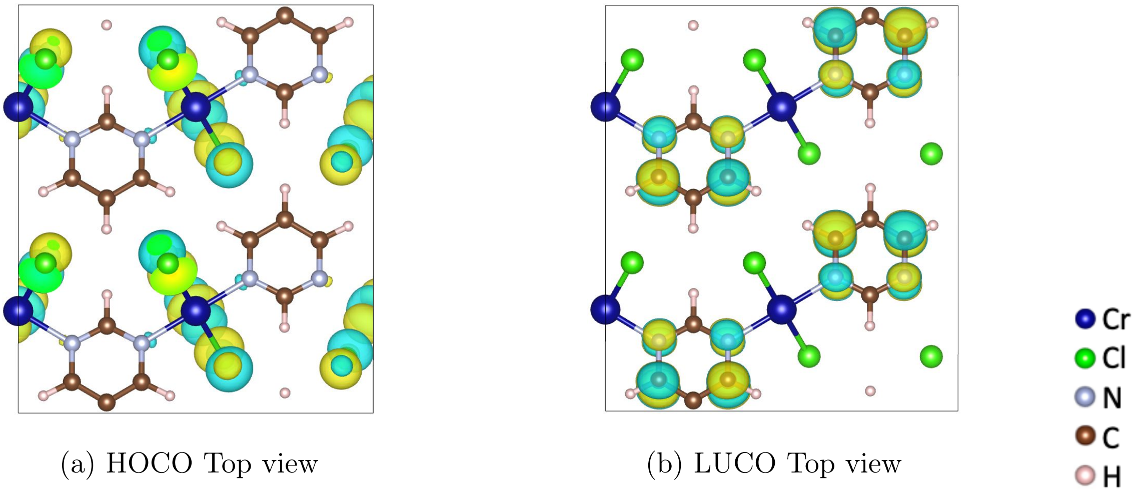

(a) HOCO Top view

(b) LUCO Top view

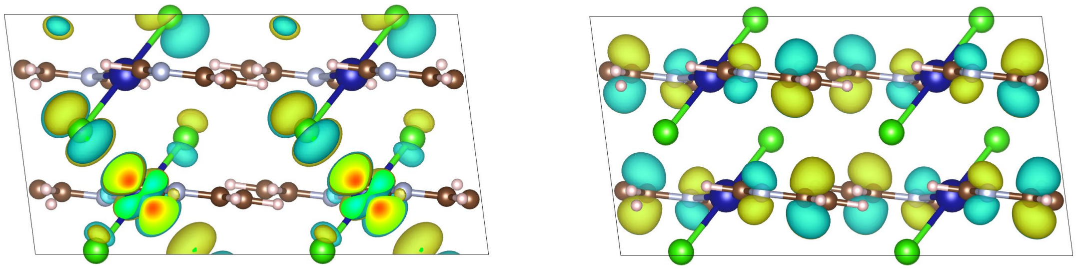

(c) HOCO Side view

(d) LUCO Side view

Figure 3.12: Graphical visualisation of the Kohn-Sham orbitals of the 2 × 2 × 1 supercell calculated at the Gamma point using the DFT package CASTEP with the PBE exchange-correlation functional. Post processing to visualise the highest occupied crystal orbital (HOCO) and lowest unoccupied crystal orbital (LUCO) has been carried out using c2x [101]. The yellow and blue colours are representative of the phase of the wavefunction.

The highest occupied band is found around the metallic ions of the system. This is in agreement with figure 3.11, since the PDOS shows that the highest occupied band right below the Fermi energy is composed of Cr and Cl. The highest occupied Kohn-Sham orbital resembles a d_{z^2} atomic orbital centred on the Cr atoms and a p orbital around the Cl. On the other hand, the lowest unoccupied Kohn-Sham orbital is found around the organic linkers. This also matches with figure 3.11 as the Kohn-Sham states right above the Fermi energy are C, N and H based. The lowest unoccupied Kohn-Sham orbital more closely resembles π molecular orbitals, with an anti-bonding nature similar to the Benzene π_5^* anti-bonding molecular orbital type [146]. After having looked at the frontier orbitals, the spin density has also been calculated and shown in figure 3.13.

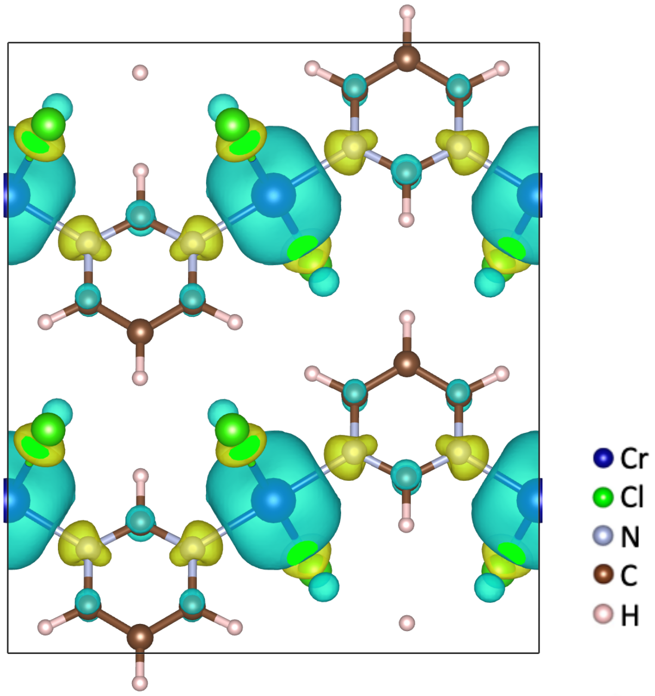

Figure 3.13: Graphical visualisation of the spin density of the $2 \times 2 \times 1$ supercell calculated at the Gamma point using the DFT package CASTEP along with c2x [101]. An appropriate isosurface level of $0.015\,\mathrm{e}\,\text{Å}^{-3}$ has been set and shows the overall spin density nature of the system. The blue and yellow colours represent the sign of the spin density, corresponding to the spin up or spin down.

Analysing the isosurface colours of figure 3.13, a ferromagnetic arrangement between the chromium ions is seen along the chromium-pyrimidine direction (J_2 direction). Furthermore, a ferromagnetic arrangement is also present between the chromium ions of adjacent layers (along the J_3 direction). These findings confirm are in agreement with experimental results presented in figure 3.10.

The majority of the spin density is located around the chromium and chloride ions. This is expected in metal-organic magnetic materials, as this accounts for the long-range weak magnetisation of the system. On the other hand, the centre of the organic rings act as nodes, resulting in a spin system with weak long-range interactions, typical of quantum materials [147].

The spin density is not only valuable to understand the spin nature of the system, but also in making comparisons with similar systems to gain a better understanding of the scientific properties it holds. A similar system, useful for comparing and understanding scientific properties, is the S=2 Heisenberg antiferromagnet $CrCl_2$ investigated by M. B. Stone *et al.* [148], which is a material of similar structure and magnetic behaviour. The interesting difference, however, lies in the Jahn-Teller distortion. In $CrCl_2$ the Jahn-Teller distortion does not lie in the spin-chain plane while in $CrCl_2(pym)$ it does. In other words, in $CrCl_2(pym)$ each J_n interaction is weakened due to the lengthened bonds caused by the distortion, but in $CrCl_2$ the only weakened interactions are J_2 and J_3, but not J_1. This is clearly seen in, for instance, $\mathrm{J_2} = -0.12(7)\,\mathrm{meV}$ for $CrCl_2$ which is an order of magnitude weaker than $\mathrm{J_1} = -1.1(1)\,\mathrm{meV}$. Following this logic, in the $CrCl_2(pym)$ all the J_n should be weakened, but this is not the case. DFT+U (U=3eV) gave a $CrCl_2(pym)$ $\mathrm{J_1} = -2.53\,\mathrm{meV}$ which is an order of magnitude greater than $\mathrm{J_2} = 0.30\,\mathrm{meV}$. These values are surprisingly qualitatively similar to those published for $CrCl_2$, as if the extra Jahn-Teller distortion is not felt. The most likely explanation for this unexpected behaviour is an enhancement in direct exchange in $CrCl_2$ through the presence of the magnetic d_z^2 orbital within the spin chain.

3.6 Conclusions

The properties of the new coordination polymer $CrCl_2(pym)$ have been reported in this thesis chapter. The presence of Jahn-Teller distortion suggests that chromium takes the Cr^{2+} oxidation state in this material, with d-orbitals splitting between the e_g and t_{2g} bands, resulting in S = 2. With the use of a $2 \times 2 \times 1$ supercell, the magnetic ground state of the system has been achieved. The supercell's band structure and density of states have shown a band gap of 1.2 eV using the BPE exchange-correlation functional in combination with a Hubbard U correction of 3 eV and MBD* dispersion correction.

With the use of a supercell, it has been demonstrated that $CrCl_2(pym)$ is an antiferromagnet approaching the quasi-one-dimensional limit with a magnetic ratio $J_1/J_2 = 8.4$. Magnetic exchange interactions are in qualitative agreement with experimental inelastic neutron scattering results and have shown antiferromagnetically correlated $CrCl_2$ spin chains, which are ferromagnetically correlated with adjacent layers through van der Waals forces and ferromagnetically correlated across the organic linkers. The supercell's PDOS suggests that the highest occupied band is primarily of chromium and chloride nature, supported by the visualisation of the HOCO which resembles a d_{z^2} atomic orbital centred on the Cr atoms and a p orbital around the Cl. On the other hand, the lowest unoccupied band arises primarily from the pyrimidine.

In summary, the analysis of this coordination polymer has confirmed its validity to be a good candidate for recreating the S=2 Haldane phase. However, despite the many advancements brought forward by this computational research to aid experimental collaborators in the recreation of the Haldane phase, this topological phase of matter has still not been achieved in the physical world. It is likely that with such a large J_2 superexchange, the ratio $J_1/J_2 = 8.4$ found with DFT+U is too small, and, in combination with the large single ion anisotropy found experimentally, the S = 2 Haldane phase is suppressed. The proximity of $CrCl_2(pym)$ to the Haldane region has however been experimentally confirmed with inelastic neutron scattering results. Therefore, careful adjustments of the magnetic properties of the system, such as superexchange and single-ion anisotropy, are likely to lead us to the S = 2 Haldane phase. More in general, looking at this work from a wider perspective, low-dimensional materials with a small band gap and strong magnetic superexchange are of great importance in developing next-generation materials that may revolutionise the IT world. The study of $CrCl_2(pym)$ has contributed to this active field of research by exemplifying the various properties that such a class of materials may hold, and by deepening our understanding of the science governing such properties.

Chapter Four

Exploring Barlowite: A Frustrated $S = \frac{1}{2}$ Kagome Antiferromagnet

4.1 Introduction

As we have seen in the previous chapters, topology, electron correlations and magnetism all play a key role in quantum materials and give rise to unconventional states of matter governed by quantum mechanics. As later explained, the interplay between symmetry and magnetism can lead to magnetic frustration and result in quantum spin liquids [149]. Understanding and harnessing materials hosting these properties has the potential to revolutionise fields such as data storage, spintronics, quantum computing and beyond. In this chapter, the structural, electronic and magnetic properties of the frustrated $S = \frac{1}{2}$ kagome antiferromagnet Barlowite are explored [150].

4.1.1 Magnetic frustration and the quantum spin liquid phase

Frustrated magnets are a class of materials in which the magnetic moments interact through competing exchange interactions resulting in a state of frustration where the magnetic moments cannot simultaneously satisfy all the interactions within the lattice. This frustration arises from the geometric arrangement of magnetic ions, leading to intricate magnetic ground states with rich and exotic properties. Frustrated magnets can even be found in nature, and one of the first examples to have gained interest are a class of minerals known as the Jarosites [151]. These minerals are classical frustrated antiferromagnets with a general formula $AM_3(OH)_6(SO_4)_2$, structured into kagome layers. A kagome lattice consists of corner-sharing triangles. A schematic representation of a kagome lattice along with frustrated magnetism is shown in figure 4.1.

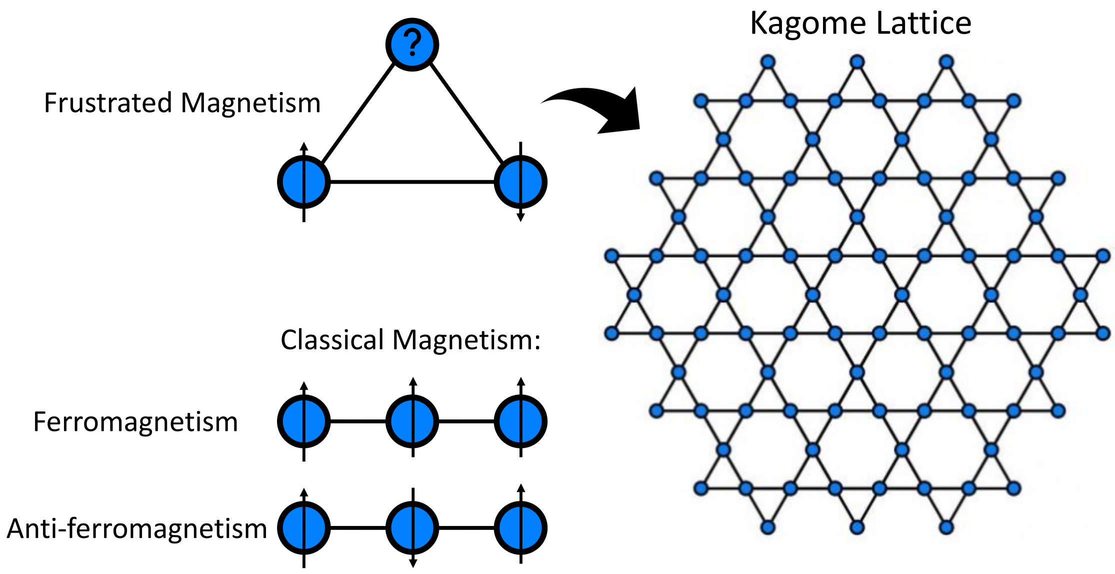

Figure 4.1: Schematic representation of kagome lattice which leads to frustrated magnetism. For a system governed by antiferromagnetic interactions, such antiferromagnetic arrangement cannot be satisfied in a triangular geometry, leading to magnetic frustration. For reference, a diagram of classical ferromagnetism and anti-ferromagnetism is included. The arrows represent magnetic moments.

Conventional magnetism exhibits long-range ordering of the spins, causing the magnetic moments to align in a ferromagnetic or antiferromagnetic ordering. On the other hand, in kagome structures the magnetic moments continue to thermally fluctuate even at low temperatures and a disorder persists [152]. The fluctuations are correlated because the overall system always tends to a lowest energy configuration, often depicted as an Ising antiferromagnetic ground state.

Under certain conditions, frustrated magnets can result in the formation of fluid-like states of matter, referred to as "spin liquids", in which the constituent spins are highly correlated but still fluctuate strongly down to a temperature of absolute zero [153]. Spin liquids can be either classical, such as in Jarosites minerals with $S > \frac{1}{2}$, or quantum. In the classical regime, fluctuations are governed by thermal energy leading the spins to rotate randomly with time. As the temperature is decreased and the energy $k_B T$ becomes small, the spins either order or freeze. On the contrary, for quantum spin liquids (with $S = \frac{1}{2}$) the magnetic moments do not freeze but zero-point motions persist, caused by Heisenberg's uncertainty principle, even at T = 0 K. In such a state, the spins are highly entangled and the systems can be described as a superposition state in which the spins point simultaneously in many different directions [153]. In other words, quantum spin liquids are characterised by quantum superpositional states formed by entangled pairs of magnetic moments.

These materials have garnered significant attention in the materials science sector due to their vast application potential. Frustrated magnets offer the possibility of developing novel magnetic memory devices with enhanced stability, reduced power consumption, and increased storage density [154]. Their unique magnetic states and the ability to manipulate spin textures can lead to the development of spintronic devices that exploit the spin degree of freedom to store and process information [155]. In addition, the intricate spin arrangements and the presence of exotic quasiparticles in frustrated magnets make them good potential candidates for realising topologically protected qubits. Frustrated magnets may provide crucial insights into the development of robust quantum systems, capable of performing complex computations with increased efficiency and reliability. Scientists are now testing magnetic skyrmions, small swirling topological magnetic excitations with particle-like properties that arise in frustrated materials, as a possible route for next generation memory devices [156].

4.1.2 Research scope

The search for these quantum spin liquid materials has been a challenge for many years without great success. Experimentally, achieving a quantum spin liquid phase requires very precise conditions, and maintaining a system in such a spin-liquid state while carrying out experiments makes it notoriously difficult to confirm their existence and pinpoint their exact nature [157]. Computationally, the requirement of non-collinear spin treatment is demanding for many DFT packages. Although materials showing traits of this quantum spin liquid behaviour have been found, the most famous example being the copper-based mineral Herbertsmithite [158], the search for quantum spin liquids continues.

In this research, the mineral barlowite has been selected as a quantum spin liquid candidate, with chemical formula $Cu_4(OH)_6FBr$. Barlowite meets all the theoretical requirements for exhibiting a quantum spin liquid nature: it is a frustrated magnet with $S = \frac{1}{2}$, an adequately small spin for quantum fluctuations caused by the uncertainty principle to produce visible zero-point motion of the spins at T=0K [159]. However, the ground state structure of barlowite has brought dispute in the scientific community, and one of the scopes of this research consists of gaining a better understanding of its structure and exploring its geometry at different temperatures and degrees of symmetry. In collaboration with an experimental team, this research aims at gaining a better understanding of the geometry of the proposed barlowite structures and at exploring the electronic properties of this material. Learning how the electronic properties change along the halide series, when other halides take the place of bromine to form new minerals, is an important scope of research, key in discovering trends for future structure prediction. In addition, the magnetic nature of the system is investigated by looking at the magnetic exchange pathways. Finally, gaining a better understanding of the frustrated magnetism this structure holds is also an important goal, especially since the true nature of this putative quantum spin liquid state is still under debate for barlowite.

4.2 Exploring the structure of barlowite

Barlowite, $Cu_4(OH)_6FBr$, is a mineral with hexagonal structure at room temperature, formed with Cu^{2+} based distorted kagome layers. More specifically, the kagome layers are formed by equilateral triangles of Cu^{2+} ions which are bound together by hydroxide anions. A second Cu^{2+} is present between the kagome layers, which is disordered with 3 possible occupation sites. Between the kagome layers the Br^- and F^- ions are also located. A schematic representation of barlowite is shown in figure 4.2.

The ground state structure of Barlowite has been in question for many years, as rival proposed structures have been presented through different studies. The difficulty in determining the ground state structure lies in the presence of disordered inter-layer Cu^{2+} sites, here presented with partial occupancies. The literature [160] has shown that Barlowite takes a $P6_3/mmc$ symmetry at room temperature (300 K) with dynamically disordered Cu^{2+} sites between the layers. However, as the temperature is lowered, a structural phase transition takes place and the disorder becomes static, with an overall lowering of symmetry. Different proposed structures of barlowite have been published in the low temperature regime. Smaha *et al.* [150] has shown a $P6_3/m$ space group at $T < 262$ K, $Pnma$ at $T < 265$ K and $P6_3/mmc$ at $T = 300$ K. A $Cmcm$ space group was also proposed [159] in the low temperature range, differing from the $Pnma$ by having another ordering scheme. Keeping in mind that these

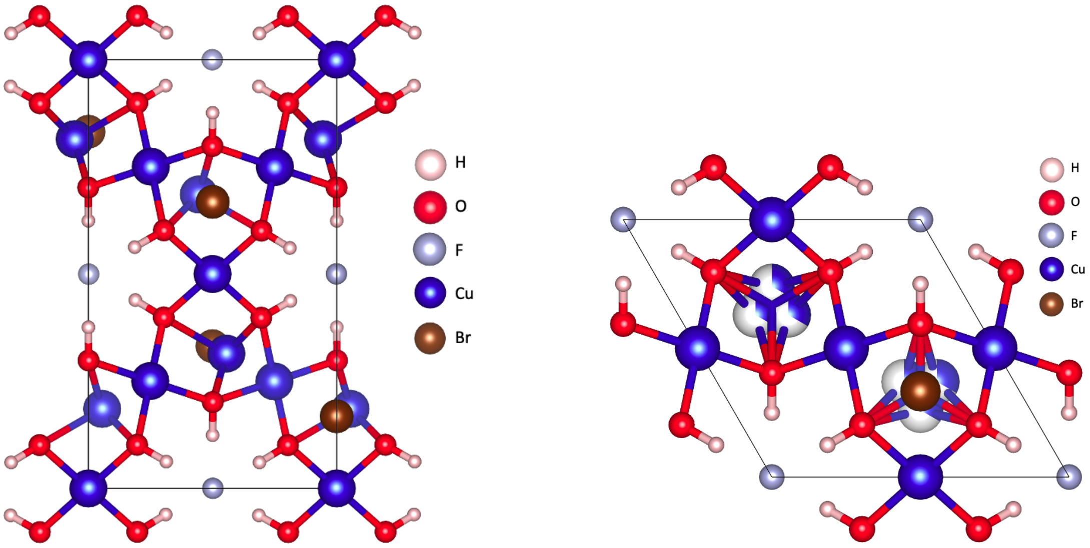

(a) *Pnma* [T=5K]   (b) $P6_3/mmc$ [T=300K]

Figure 4.2: Visualisation of the structure of barlowite $[Cu_4(OH)_6FBr]$ at different temperatures. At low temperature Barlowite is found to order in a *Pnma* space group as shown in (a), while at room temperature a $P6_3/mmc$ space group is found as shown in (b). The partially filled Cu^{2+} ions represent partial occupancies. The structures have been synthesised by experimental collaborators: Dr Lucy Clark and her research group [159].

are experimental findings, one possible reason for these different proposed structures is the use of different reagents in the hydrothermal preparation of these synthetic samples. The $P6_3/m$ sample was synthesised using $CuBr_2$ and LiF [161], while the *Cmcm* sample was made using $CuCO_3 \cdot Cu(OH)_2$, NH_4F and HBr [162].

In order to gain a better understanding of the crystal structure of barlowite and its transitions in phase and symmetry, a DFT investigation has been carried out and backed up with experimental research carried out by Dr Lucy Clark and her research group from the School of Chemistry at the University of Birmingham. Dr Clark's team combined high-resolution synchrotron X-ray and neutron powder diffraction data to examine both positional and compositional disorder within their ground-state structures. Furthermore, magnetometry, heat capacity, and high-flux powder neutron diffraction measurements were used to correlate this structural disorder with the magnetic ground state.

High-resolution neutron and X-ray powder diffraction confirmed the hexagonal space group $P6_3/mmc$ at T = 300 K [159]. As for the low temperature range, high-resolution powdered X-ray diffraction data showed Bragg peaks which can be indexed with the orthorhombic *Pnma* space group at T = 5 K. This data confirms a hexagonal to orthorhombic structural transition to take place as the temperature is decreased, and that the positional disorder is therefore driving the structural transition. In order to gain a better understanding of such transition, DFT has been used to quantify the energies associated with the disorder present in the system.

When carrying out DFT calculations on spin liquid materials, particular care must be taken. Since barlowite and other similar quantum materials exhibit traits of Mott physics, barlowite being a Mott insulator [163], a Hubbard U correction was included in our system. This is also an attempt to capture the potential superconductivity nature of barlowite later discussed in section 4.3, since DFT usually fails to predict localised polaron states [164, 165]. DFT+U calculations were carried out using the PBE exchange-correlation functional using CASTEP version 22.11. A Monkhorst-Pack k-point grid was implemented with a k-point spacing of 0.05 $2\pi/\text{Å}$. Following previous implementations of DFT+U on barlowite and similar materials [163, 166] as well as Dudarev's approach [167], a U parameter of $U_{eff} = 5\,\text{eV}$ was chosen. Although a series of U values have been tested in the 3 eV to 6 eV range, our results are not sensitive to the choice of U within the selected range.

Each disordered Cu^{2+} ion has 3 possible positions. In a unit cell, which includes 2 disordered Cu^{2+} ions, there are 6 potential Cu^{2+} sites available. Following the symmetry of the cell, 4 possible configurations can be made with 2 Cu^{2+} ions filling up the 6 possible sites. These 4 configurations are shown in 4.3.

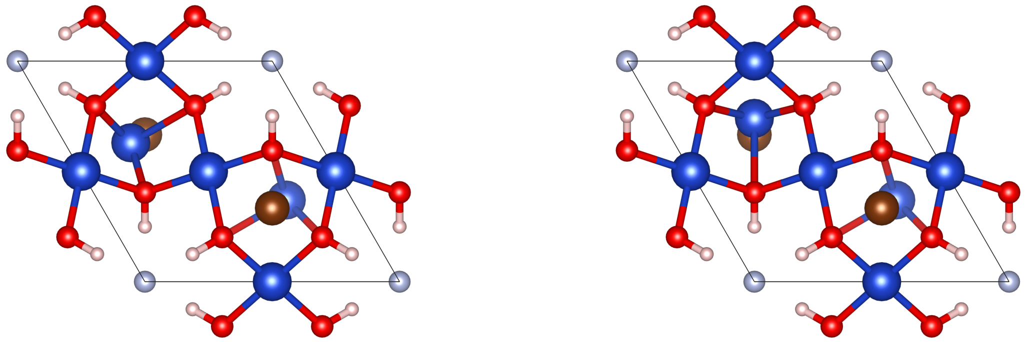

(a) Far [6.43 Å]

(b) Medium-far [6.39 Å]

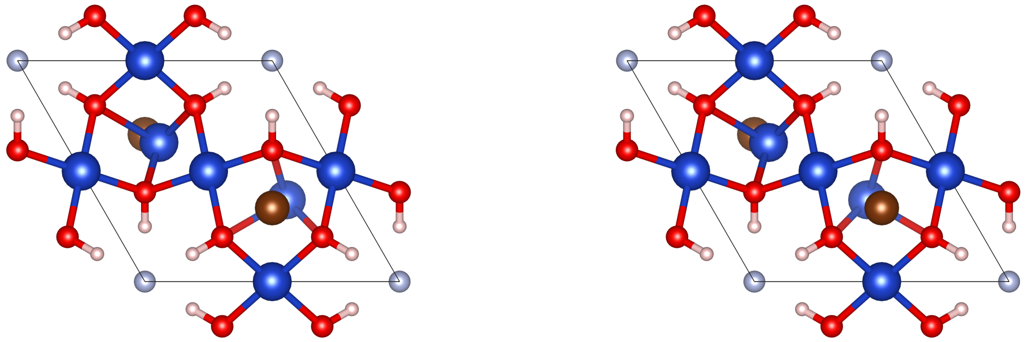

(c) Medium-close [5.94 Å]

(d) Close [5.63 Å]

Figure 4.3: Considering the high temperature unit cell and its symmetry, 4 possible configurations with respect to the disordered Cu^{2+} ions can be made with 4 distinct Cu^{2+} to Cu^{2+} distances. The distance between the disordered Cu^{2+} ions is included in the label.

In the high temperature $P6_3/mmc$ phase, there is an equal probability for these ions to be found in each of the 3 possible sites at any one time, although the presence of coupling between the sites leads the system to a dynamic low energy disposition of its disordered atoms. In other words, there is some order amongst the disorder, as there is some level of correlation between the locations of the copper ions. The four configurations shown in figure 4.3 have been geometrically optimised. The structural information of the optimised unit cells has been summarised in table 4.1.

Distance between disordered Cu^{2+} ions [Å]	Volume [$Å^3$]	Density [amu/$Å^3$]	Lattice Parameters [Å]			Cell Angles			Disordered Cu^{2+} to Central Cu^{2+} Bond Lengths [Å]	
			a	b	c	α	β	γ	Cu^{2+}-Cu^{2+} Pair 1	Cu^{2+}-Cu^{2+} Pair 2
Experimental	359.04	2.54	6.68	6.68	9.30	90.0	90.0	120.0	*Disordered*	*Disordered*
Far : 6.43	361.52	2.52	6.74	6.56	9.36	90.0	90.0	119.1	3.22	3.22
Medium-far : 6.39	361.13	2.52	6.67	6.67	9.35	90.0	90.0	119.8	3.24	3.24
Medium-close : 5.94	360.87	2.52	6.70	6.66	9.35	90.0	90.0	120.0	2.84	3.18
Close : 5.63	361.45	2.52	6.69	6.69	9.44	90.0	90.0	121.0	2.81	2.81

Table 4.1: Summary of PBE+U+MBD* geometry optimisation results with U = 5 eV. A cut-off energy of 1100 eV has been used with a k-point spacing of 0.05 2π/Å and a Gaussian smearing scheme with a 0.2 eV smearing width. The Broyden density-mixing scheme has been used throughout the optimisations.

After successful geometry optimisations, DFT was used to calculate the ground-state energy of each of the 4 configurations shown in figure 4.3, and results are presented in figure 4.4. Analysing these results, DFT calculations have been able to quantify the energy range associated to the positional disorder of the Cu^{2+} - Cu^{2+} sites, and showed that the lowest energy structure was found to be the one with the medium Cu^{2+} - Cu^{2+} displacement. This result indicates that medium distance sites are favoured due to the electrostatic and magnetic forces at play, and suggests that the many possible disordered arrangements in the kagome lattice containing medium Cu^{2+} - Cu^{2+} distances prevail on average. This is in agreement with the experimental low temperature *Pnma* structure, found to contain medium and far filled sites with a 2:1 ratio, and with no energetically unfavourable close sites filled.

The number of Cu^{2+} - Cu^{2+} distance combinations that can form in a kagome lattice increases with the size of the system under consideration, given the same symmetry constraints: the larger the system, the more combinations can exist along each of the 3 different kagome lattice directions. In larger systems, which host combinations of different filled disordered Cu^{2+} - Cu^{2+} sites, the disorder becomes more homogeneous. For instance, a larger cell made from structure 4.3c does not only contain medium-close filled sites but also medium-far ones. This

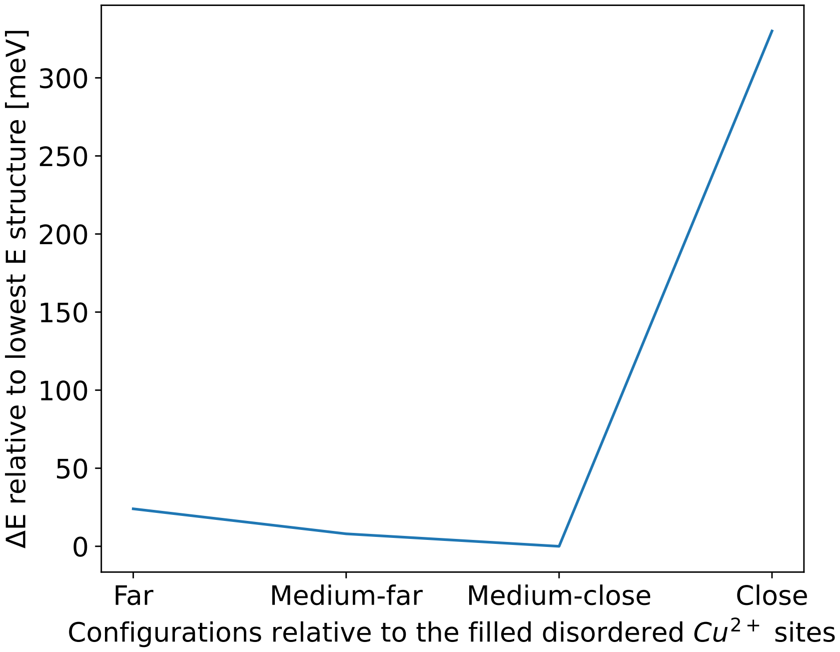

Figure 4.4: Relative energies per unit cell of the four configurations shown in figure 4.3. DFT+U ($U_{eff} = 5eV$) has been implemented with ultrasoft pseudo-potentials. The medium-close configuration is the lowest in energy out of the four structures.

has been taken into account in our results by using periodic boundary conditions. Without periodic-boundary conditions, the energy differences shown in figure 4.4 would be even more accentuated. Furthermore, temperature makes the system dynamically disordered; however, it is expected that the correlation between Cu^{2+} sites always leads the system towards a majority of medium-close filled sites. On average, which of the 3 Cu^{2+} sites is filled is equally likely due to the dynamic disorder, but the Cu^{2+} correlations bring a certain level of order within the disorder.

After having concluded that the unit-cell with lowest energy contains medium-close Cu^{2+} sites, a stable structure with no partial occupancies has been achieved. In addition, a separate geometry optimisation has been carried out for the $Pnma$ structure, resulting in a successful refinement of both of the barlowite structures shown in figure 4.2. This is an important step in order to advance in this study, as these optimised structures will be used to investigate barlowite's electronic and magnetic properties, presented in the following sections.

4.3 Electronics of barlowite and its halide analogues

Quantum spin liquids are insulating materials with preexisting electron pairs, with the potential of becoming high temperature superconductors when doped [168]. Although it is known that spins in quantum spin liquids are highly entangled, the precise nature driving unconventional superconductivity in this class of materials is still being researched, as BCS [169] theory based on Cooper-pairs is successful for explaining low-temperature conventional superconductivity, but inadequate for quantum spin liquid materials. The mechanisms for such high temperature superconductivity in quantum spin liquids is still being investigated [170].

Although evidence for this quantum spin liquid superconductivity is still scarce, Hong-Chen Jiang [171] has demonstrated that doping quantum spin liquids can naturally give rise to d-wave superconductivity. In a different study, Ya-Ting Jia *et al.* [172] reported a pressure-induced insulator to metal Mott transition followed by the emergence of superconductivity. The quantum spin liquid candidate $NaYbSe_2$ was used, which is surprising since Mott transitions are rare in quantum spin liquid systems which are, by nature, without long-range magnetic order.

It is therefore clear that quantum spin liquid candidates possess complex and sometimes unexpected electronics, and DFT has been used to explore barlowite's electronic properties. The electronic band structure and density of states have been calculated for the $Pnma$ structure. Results are shown in figure 4.5.

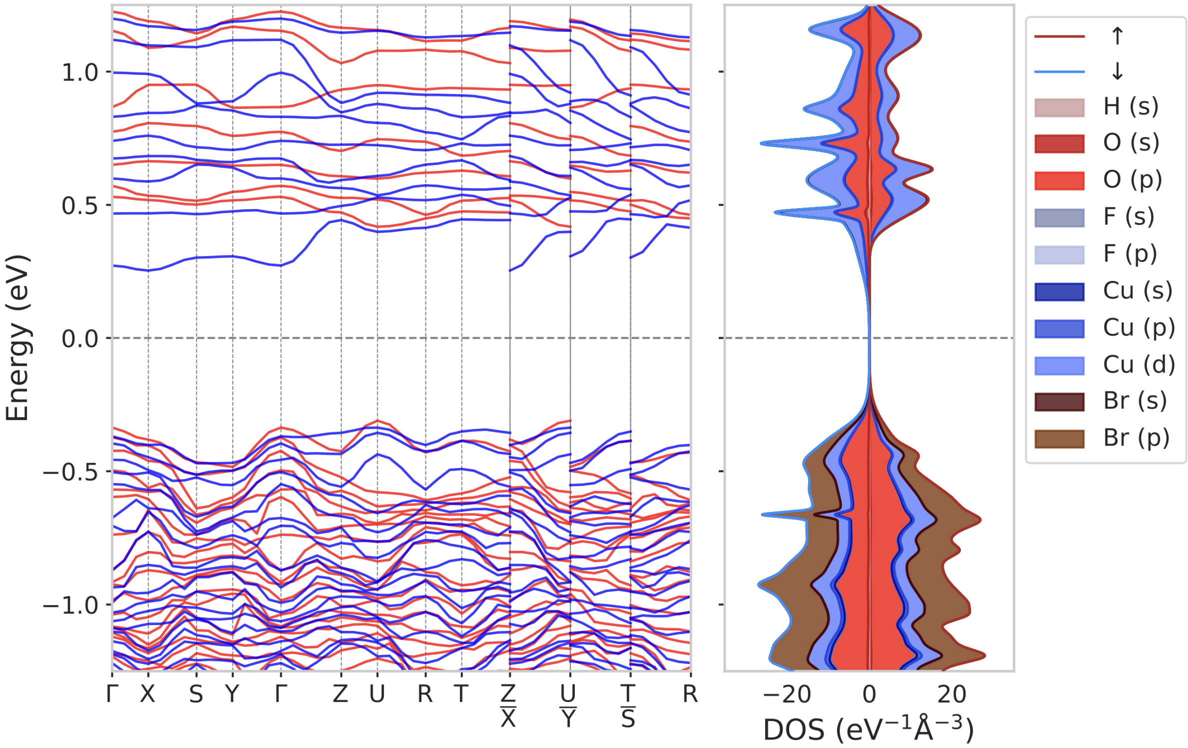

Figure 4.5: DFT+U band structure and projected density of states of barlowite *Pnma* system. The PBE exchange correlation functional was used with $U_{eff} = 5$ eV.

The band-structure shows an insulating nature of barlowite, with an indirect band-gap of 0.56 eV. This is expected for such systems, with a clear presence of Cu^{2+} states just above the Fermi energy. Dispersion is seen around the valence bands below the Fermi energy especially around the U and Γ high symmetry points. The band just above the Fermi level is of the same spin type, arbitrarily labelled as spin-down in our result, covering the entire band-structure. The highest occupied crystal orbital is expected to be around the Cu^{2+} and hydroxide, whereas the lowest unoccupied crystal orbital is mostly expected to be around just the Cu^{2+} ions.

As previously discussed, the idea of doping to alter the electronic properties of barlowite has become of popular interest [173]. It has been shown that electron doping using Zn does indeed produces localised states in the band gap [166], however, research on the effect of changing halide instead of doping with other metals is still scarce. To investigate this, the bromine halide has been exchanged with chlorine and iodine creating claringbullite $[Cu_4(OH)_6FCl]$ and iodide-substituted barlowite $[Cu_4(OH)_6FI]$ respectively. A DFT+U geometry optimisation has been carried out for these new structures, and the electronics of these systems were tested. Band-structure and density of state calculations were then carried out for both claringbullite and iodide-substituted barlowite, and results are shown in figures 4.6 and 4.7 respectively.

Similar electronic properties are seen in claringbullite and iodide-substituted barlowite with respect to barlowite. The band-structures present similar characteristics, with the main difference being in the iodide material showing a 0.34 eV band-gap, 0.22 eV smaller than barlowite's band-gap.

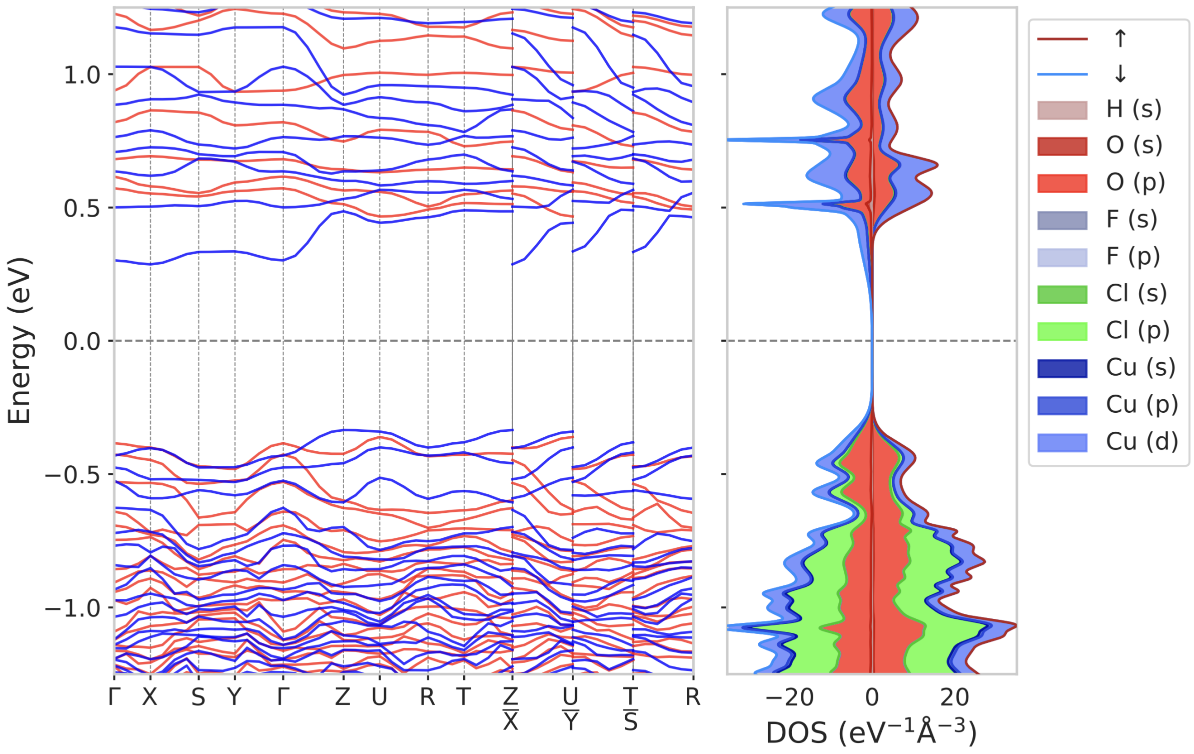

Figure 4.6: Claringbullite $[Cu_4(OH)_6FCl]$ DFT+U band structure and projected density of states. The PBE exchange correlation functional was used with $U_{eff} = 5$ eV.

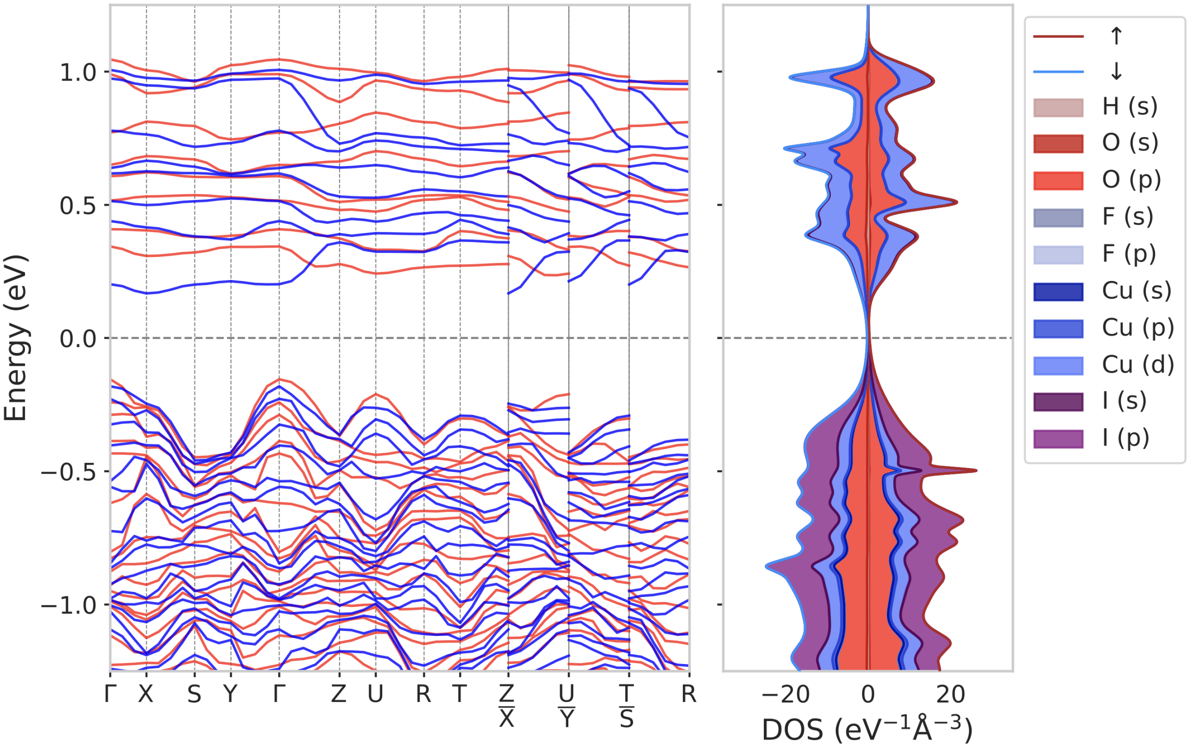

Figure 4.7: Iodide-substituted barlowite $[Cu_4(OH)_6FI]$ DFT+U band structure and projected density of states. The PBE exchange correlation functional was used with $U_{eff} = 5$ eV.

Iodine has an overall greater number of electrons than bromine, while chlorine has a smaller number than bromine, however, since the number of valence electrons is unchanged for these structures, and all the copper are expected to stay cations with a 2+ charge, no significant insulator-conductor transition is expected. By comparing the results, it appears that as we move down the halide group, the halide becomes more involved in the HOMO and valence band.

Apart from the electronic properties, the magnetic nature of barlowite also plays an important role in its properties, especially in its potential quantum spin liquid nature. In the next section, the magnetic exchange and frustrated magnetic nature of barlowite are explored.

4.4 Exploring barlowite's magnetism

The magnetic nature of frustrated magnets is hard to explore in static zero temperature plane wave DFT calculations due to the dynamic nature of the magnetic moments in such materials. The frustrated magnetic moments spatially rotate through the progression of time, which cannot be captured by DFT; however, such behaviour can be indirectly inferred by looking at the magnetic exchange. If the magnetic dipole orientation is random and equally likely for each frustrated spin, there should not be one configuration of drastically lower energy, but should all be of comparable energy. The magnetic exchange interactions have therefore been studied, with J_1 along the kagome layer and J_2 between the layers.

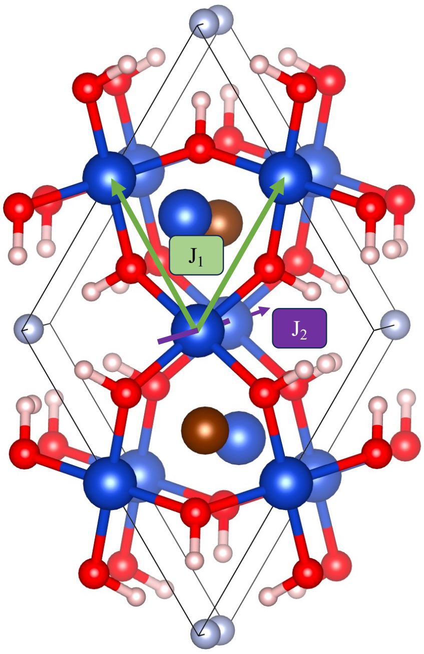

Figure 4.8: Diagram depicting the magnetic exchange interactions with $J_1 = -2.2$ meV along the kagome layer and $J_2 = -10.6$ meV between the layers. The J_1 corresponds to the nearest neighbours of the central Cu^{2+} ion, and two equidistant neighbours are present in this case. The disordered Cu^{2+} ion in the middle of the triangular motif is on a different layer.

The magnetic exchange of the system has been calculated both within the layer (J_1) and across the different layers (J_2). The magnetic exchange within the triangular motif is $J_1 = -2.2\,\mathrm{meV}$ and between the different layers $J_2 = -10.6\,\mathrm{meV}$. The disordered Cu^{2+} ion in the middle of the triangular motif is on a different layer and breaks the geometrical symmetry of the system because of its disorder. This has a very small impact on the exchange interactions within the layer. Although J_1 should take two different values along the two distinct green arrows shown on figure 4.8 because of the broken symmetry, the energy differences are less than 1 meV, too small to be accurately captured by DFT. The exchange within the layer is close to zero, which is expected for frustrated magnets, as a low exchange allows for the thermal energy to compete and keep the system in a spin liquid state.

On the other hand, J_2 is larger, giving a clear suggestion that such material is antiferromagnetic along the different layers which are stacked on top of each other. With such low J_1, it is possible for the kagome layer to enter both a ferromagnetic and antiferromagnetic nature. Beyond nearest neighbour interactions and thermal energy can have a strong impact on the magnetic configuration of the system when working with such low energies, although its negative value suggests a preference towards an antiferromagnetic arrangement. These exchange results are important in confirming the presence of frustrated magnetism, since barlowite is indeed expected to be an antiferromagnetic material with a triangular lattice [150], proving this to be a quantum-spin liquid candidate.

4.4.1 Implementing non-collinear spin-polarised DFT

The magnetic moments in frustrated magnetism can be non-collinear, since the frustrated spin dynamically changes direction in the 3D space. This means that taking an Ising ferromagnet modelling approach is inadequate and a non-collinear spin approach is required, able to include spin-orbit interactions. In general, spin-orbit coupling is a relativistic effect, which becomes important when studying systems that involve heavy elements, such as transition metals, or systems with non-conventional magnetism. In heavy elements, inner-shell electrons are pulled closer to the nucleus, causing their kinetic energy to increase and relativistic effects to become important. In these materials, the spin and orbital angular momentum of the electrons become strongly coupled, leading to significant spin-orbit interactions [174]. Neglecting spin-orbit coupling in these cases can lead to inaccurate predictions and fail to capture the true electronic structure and properties of the system.

Spin-orbit coupling has been shown to account for peculiar quantum-mechanical properties when encompassing different aspects of symmetry and topology in kagome materials. Such materials have been the recent focus in the search of topologically non-trivial ground states resulting from the opening of spin–orbit coupling gaps. These states would carry a finite spin Berry curvature and topological surface states. Over the recent months, Di Sante *et al.* [175] has used the XV_6Sn_6 kagome family (where X is a rare-earth element) to show finite spin Berry curvature contribution present at the centre of the Brillouin zone.

Non collinear relativistic DFT calculations have therefore been carried out on barlowite. The LDA exchange-correlation functional was used with fully relativistic SOC19 pseudopotentials taken from the CASTEP-23.1 pseudopotential library. Even though more advanced exchange-correlation functionals are available in non-relativistic DFT, many are missing the non-collinear physics components and therefore are not suitable to carry out non-collinear calculations [176]. The c2x [101] code has been used for post processing, representing spin as vectors which have then been visualised using VESTA with arrows.

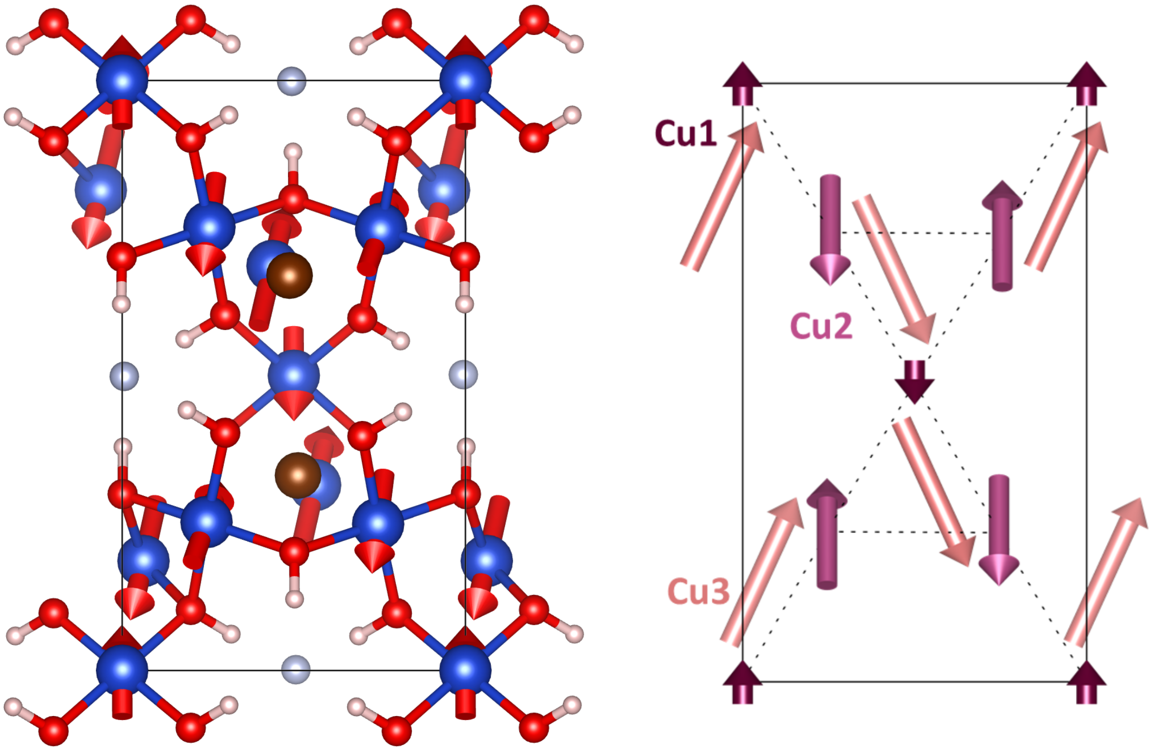

(a) DFT Results (b) Experimental Results

Figure 4.9: Barlowite *Pnma* magnetic ground state. (a) Relativistic DFT non-collinear spin results, calculated including spin-orbit coupling using CASTEP-23.1, LDA exchange correlation functional and SOC19 relativistic pseudopotentials. (b) Experimental high-flux powder neutron diffraction results, calculated using the D20 diffractometer at the Institut Laue-Langevin by Dr Clark and her research team [159].

Relativistic DFT results have been able to capture the ground-state magnetism of barlowite, overall in good conformity with experimental results. Experimental high-flux powder neutron diffraction shows an antiferromagnetic arrangement of the Cu^{2+} magnetic moments at the vertices of the triangular kagome motifs. This has also been captured by our DFT results. It is worth mentioning that non-collinearity is indeed seen, with 3 distinct planes in which the spins reside. These 3 planes can be understood from the experimental results in figure 4.9b, with each plane being along the 3 Cu atom types, labelled as Cu1, Cu2 and Cu3. This is in agreement with the DFT results.

One difference, however, corresponds to the Cu3 ions. Experiments show two different possible directions in which these moments can lie. DFT results, on the other hand, portray all Cu3 ions to point in the same direction. The DFT results present these Cu3 ions in a parallel or anti-parallel fashion, while experiment found them to be at an angle, although co-planar in both experiment and computation, However, the relative ferromagnetic or anti-ferromagnetic arrangement of these Cu3 ions matches in both experiment and simulation.

Comparing the non-collinear results to the previously calculated magnetic exchange, a good agreement is found. $J_1 =$ -2.2 meV, being negative, is in agreement with the anti-ferromagnetic arrangement found at the vertices of the kagome motifs. It is worth keeping in mind that spin is a property of the electrons, and these DFT calculations with spin-orbit coupling reproduce spin density as a vector field on a 3D grid, with the length of the arrows being proportional to the field strength. The spin density has then been integrated over a sphere centred on each Cu^{2+} ion. This is therefore only a visualisation technique, as a more physically accurate quantum-mechanical approach would require some form of projection of the wave-functions of the system onto localised atomic states.

With this said, using this visualisation technique is adequate for the type of research carried out in this study, provided that one is conscious about what the arrows are actually showing. Results are in good agreement with experiments, and the added complexity and computational cost of implementing a more physically accurate scientific technique is therefore not required.

In this new type of DFT calculation, it has been discovered that the use of symmetry in CASTEP may constrain the spin state to have the symmetry of the atomic geometry, which is not a scientifically valid constraint to be placed on the magnetics of the system. The symmetry parameter seems to impose a level of symmetry on the spin directions, preventing the non-collinear nature of the material to be captured. It is therefore important to switch off symmetry for these types of DFT calculations.

Overall, both DFT and experimental results do not suggest that barlowite is a quantum spin liquid, or, at least, not under these conditions. However, since barlowite has been shown to have different possible symmetries, one important question in the scientific community with limited published information is the interplay of the material's space group with the spin texture of the system. It has been hypothesised that the precise crystal structure adopted at low temperature has a strong impact on the magnetic properties of the material [150]. Appreciating this explains why different magnetic ground states have been reported.

In order to cast light on this topic, a non collinear DFT calculations has been executed using the high temperature structure which originated from the $P6_3/mmc$ space group.

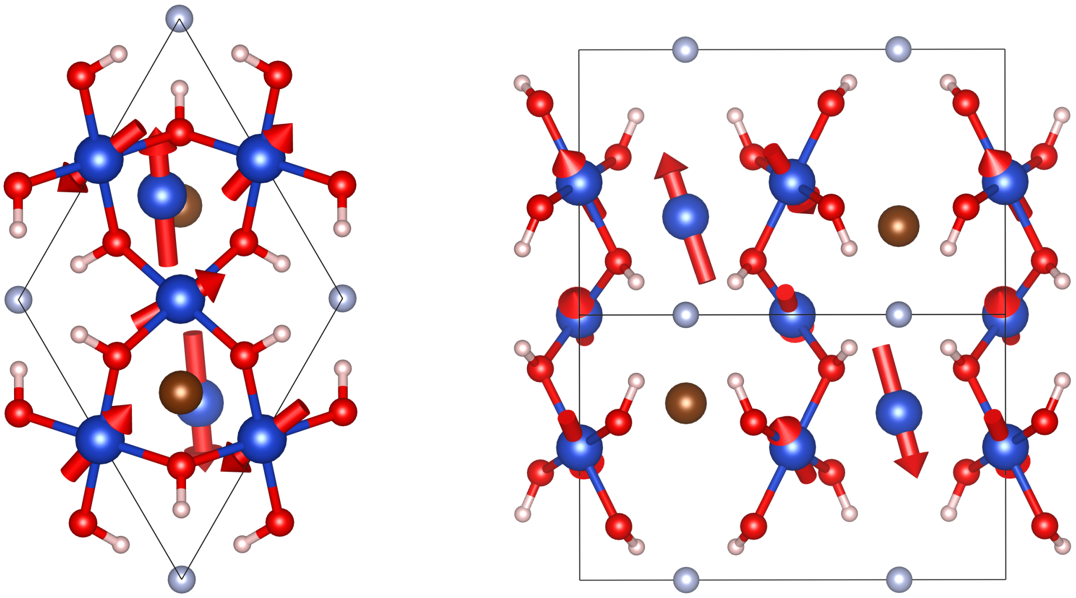

(a) Top view

(b) Side view

Figure 4.10: Barlowite magnetic ground state of the high temperature structure which originated from the $P6_3/mmc$ space group. Relativistic DFT non-collinear spin results, calculated including spin-orbit coupling using CASTEP-23.1, LDA exchange correlation functional and SOC19 relativistic pseudopotentials.

Similarities are present between the low temperature *Pnma* magnetic ground state shown in figure 4.9 and the high temperature magnetic ground state shown in figure 4.10. Analysing the top view plane, while both structures confirm an antiferromagnetic nature with respect to the vertices of the triangular kagome motifs, the magnetic moments of these vertices are more rotated with respect to each other in the high temperature structure magnetic ground state. This would suggest that the system is approaching a valence bond crystal state. Smaha *et al.* [150] has indeed predicted that the closely related barlowite space group $P6_3/m$ does indeed result in a valence bond crystal, with spins arranged in a pinwheel disposition, coherently pointing at an angle with respect to each other forming a pinwheel like pattern. In addition, it has been predicted that barlowite in the $P6_3/mmc$ space group would indeed transition into a quantum spin liquid if doped with zinc. This is an interesting result, opening different avenues for future research with different dopants and doping proportions.

Looking at both figures 4.9 and 4.10, some level of magnetic ordering is clearly present. This is most likely due to the Cu^{2+} moments between the kagome layers causing long-range magnetic order.

4.5 Conclusions

In this work, the proposed structures of the spin 1/2 kagome antiferromagnet barlowite have been assessed, with focus on the highly symmetrical high temperature $P6_3/mmc$ space group structure and the lower temperature *Pnma* structure. The structural disorder has been assessed, with each disordered Cu^{2+} ion having 3 possible occupation sites. DFT+U calculations provided an energy scale of 330 meV for this disorder, and have shown that the most energetically favourable disposition of the Cu^{2+} ions is for them to be in a medium-close arrangement.

The electronics of barlowite have been explored, and an insulator nature has been confirmed with a band gap of 0.56 eV. The effects of changing halide on the electronic properties have also been investigated: claringbullite has been found to have a band-gap of 0.04 eV more than barlowite while the iodide-substituted barlowite has been found to have a band-gap of 0.22 eV less than barlowite. The DOS of the three crystal structures shows similarities, with copper being the dominant element in the conduction band. It has been found that iodine is more strongly involved in the valence band as compared to the other halides.

Lastly, the magnetics of barlowite have been explored, and, although they do not suggest a quantum spin liquid state, non collinear spin relativistic DFT calculations with spin orbit coupling agree with experiment. The magnetic exchange parameters have also been found to be J_1 = -2.20 meV and J_2 = -10.6 meV, confirming an antiferromagnetic nature of barlowite.

In conclusion, this work has contributed in establishing the properties of barlowite, providing new data in terms of geometry, electronics and magnetism. This opens the door to further avenues of research by combining the newly investigated halide structures with appropriate dopants. If the right dopant, such as a transition metal like zinc [150] or an alkaline earth metal like magnesium [173], can be identified and implemented into barlowite, claringbullite or iodide-substituted barlowite, the long sought quantum spin liquid may be found.

Chapter Five

In the Search of New Quantum Materials

The potential that quantum materials can offer is dependent upon the set of properties each material holds, and these desirable properties drive the search for new compounds. The work carried out on metal organic magnets and frustrated magnets, specifically $CrCl_2(pym)$ and $Cu_4(OH)_6FBr$ respectively, has shown the importance of quantum spin in regards to the magnetic nature of such systems. This work has emphasised the value in harnessing the physical properties of such materials for quantum applications, such as the electronics or the magnetism of the system, which goes beyond the chemical properties often exploited in MOFs and other related materials. This knowledge paves the way for the discovery of novel structures, as the versatility of such quantum systems allows for the synthesis of a large quantity of derived materials. It is therefore promising to make use of the DFT research skill-set developed on such systems to embark in the search of new quantum materials using new metals and organic linkers.

This research spans into two diverse fields of research, the first taking its roots in the technology and IT sector with the aim of developing next generation semiconductors, while the second focusing on scientific advancements by continuing the search for the S=2 Haldane phase. The modular nature of metal organic frameworks makes them the ideal candidate for the development of new materials with a series of different applications. This study takes its foundations from the work presented in chapter 3, specifically $CrCl_2(pym)$ framework, and uses this structure as the starting point for the discovery of new ones.

Regarding the field of technology, this research aims at developing a new family of magnetic and electronic metal-organic coordination frameworks in order to design switchable and stimuli-responsive semiconductors. Existing inorganic strongly-correlated semiconductors are dense, rigid and difficult to design [177]. One of the most likely novel families offering characteristics to overcome these obstacles are strongly-correlated metal-organic coordination frameworks (SCCFs), although only a small number of such materials have so far been investigated in the literature [178–181]. It is therefore essential to gain a clear understanding of the role of the metal ions and organic linkers in such materials in order to attain the desired functional properties and gain a strong knowledge of the magnetic and structural local correlations of such structures.

In regards to this work's contribution towards scientific progress, this research aims at continuing the search for the S=2 Haldane phase started in Chapter 3. Despite not having been experimentally found for $CrCl_2(pym)$, the results collected pave the way for the search of new structures able to host this topological phase of matter. The proximity of $CrCl_2(pym)$ to the Haldane phase and the modularity inherent to metal-organic magnets suggest that optimising single ion anisotropy and superexchange interactions is a promising route to the S = 2 Haldane phase. This research therefore aims at finding new semi-1D coordination frameworks which exhibit stronger 1D character than $CrCl_2(pym)$. In other words, this research's goal is to find a material with a suitably large magnetic exchange (J_1/J_2) ratio in order to prevent the S=2 Haldane phase from being suppressed.

5.1 Discovering new structures hosting different metals

The choice of metal used in correlated materials is essential in determining the properties it exhibits, not only in terms of the number of electrons and crystal field theory, but also in terms of the structure itself. One example comes in a material similar to $CrCl_2(pyz)_2$, in which Cr has been changed with Ni and the pyrimidine linker has been exchanged with pyrazine. It has been shown that the nickel based compound has a tetragonal structure with tetragonally elongated $NiCl_2N_4$ sites [182], while the material with Cr has an orthorhombically distorted structure with an *Immm* space group [109]. This highlights the flexibility and tunability of such frameworks, and exemplifies how sensitive the intrinsic geometry of the system is to the specific metal ions or organic linkers used.

5.1.1 Investigating new transition metals (M) in $MCl_2(pym)$

Different transition metals have been investigated when acting as the central metal ion, including V, Fe, Co and Ni. To capture the strongly correlated nature of this class of materials, a Hubbard U correction was used in all calculations. In accordance with the literature [183–188] of similar DFT+U publications and Hubbard U assessments and evaluations, the following Hubbard U values were chosen: for V and Fe U = 2 eV, for Co U = 4 eV and for Ni U = 6 eV. Due to the nature of the Hubbard U correction, pinpointing a specific value is not as straightforward as one would like, however, it has been tested that varying the Hubbard U correction by ± 1 eV around the selected values only has a minimal impact on results.

In addition, MBD* dispersion correction was used to account for van der Waals forces, similar to chapter 3. After convergence testing, a cut-off energy of 1100 eV has been chosen with a k-point spacing of 0.05 $2\pi/\text{Å}$. These values match those used in chapter 3, which is not surprising due to similarities of the systems. Likewise, the same PBE exchange correlation functional with ultrasoft pseudopotentials was chosen for these calculations, as their success when applied to this class of materials has been confirmed by previous work in chapter 3.

Geometry optimisations have been carried out for each of these new structures and results are presented in table 5.1. The lowest energy spin arrangement has been selected for each structure. It has been seen that along the direction of the organic linker, V and Cr achieve a lowest energy ferromagnetic nature while Fe, Co and Ni prefer an antiferromagnetic arrangement. A magnetic trend can therefore be noticed as we move along the period of the periodic table, in which a shift from FM to AFM is present for the tested metals. Of course, more metals should be tested to draw conclusions, and a more detailed analysis of the spin arrangements with super-cells can be carried out. To find the true magnetic ground-state of each system, J_1, J_2 and J_3 need to be tested, requiring the use of super-cells. However, such high accuracy was not required for the scope of this research, as the same qualitative band-gap results were found independent of the magnetic arrangement for each of the four structures. The band structure and density of states of each of the four frameworks was calculated and shown in figure 5.1.

Metal Ion (M) in MCl_2(pym)	U Value [eV]	Volume [Å^3]	Density [amu/Å^3]	Lattice Parameters [Å]			Cell Angles		
				a	b	c	α	β	γ
V	2	313.13	1.29	3.58	12.18	7.17	90.01	90.94	90.24
Fe	2	309.28	1.34	3.57	12.28	7.05	89.87	90.06	90.24
Co	4	290.70	1.44	3.60	11.93	7.01	89.98	90.11	90.20
Ni	6	293.54	1.43	3.61	11.66	6.97	90.00	90.00	90.00

Table 5.1: $MCl_2(pym)$ geometry optimisation results. A cut-off energy of 1100 eV has been used with a k-point spacing of 0.05 2π/Å and a Gaussian smearing scheme with a 0.2 eV smearing width. The Broyden density-mixing scheme has been used throughout the optimisations.

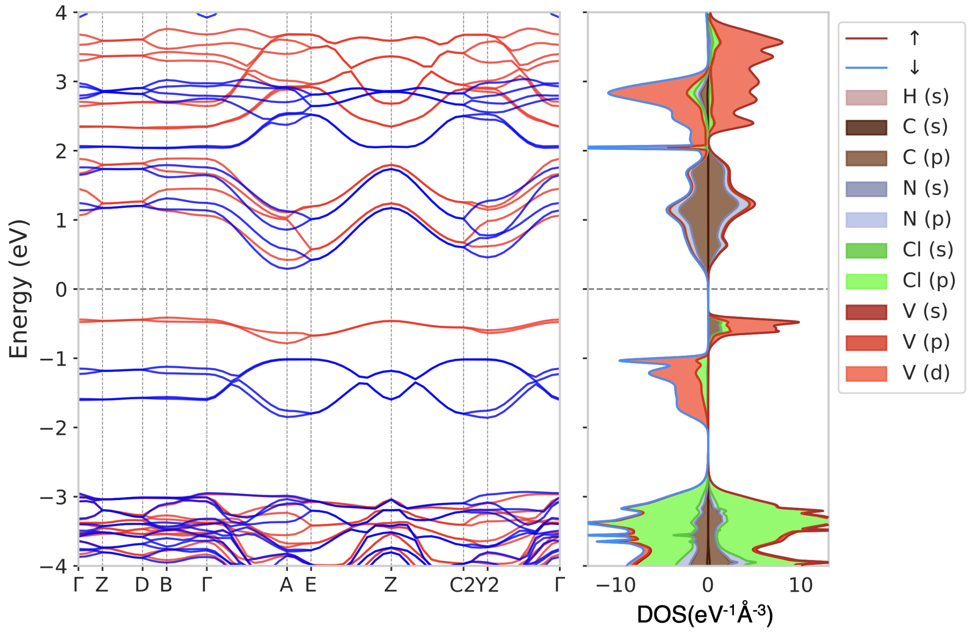

(a) Vanadium

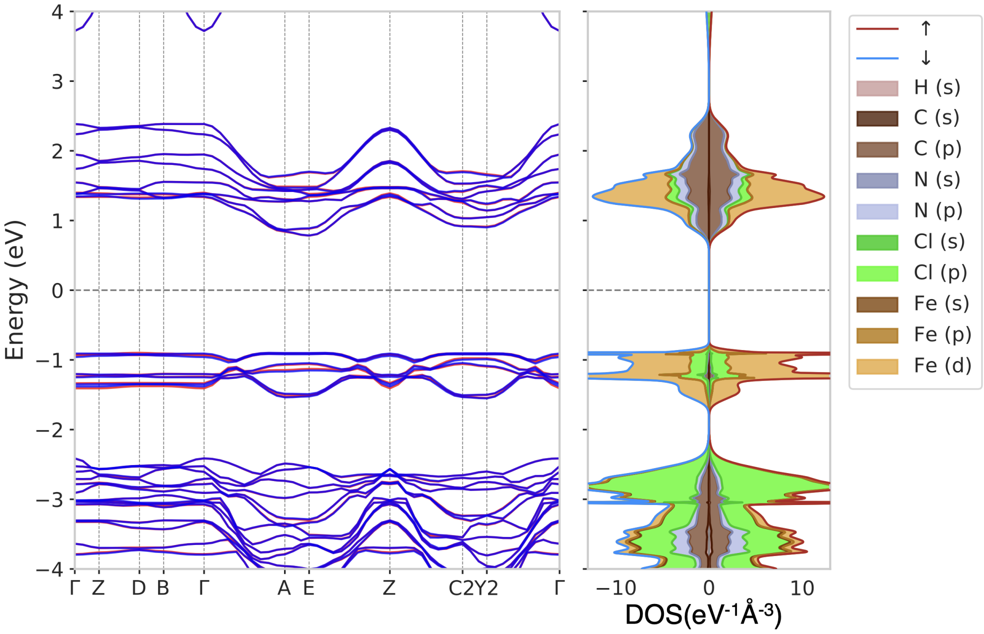

(b) Iron

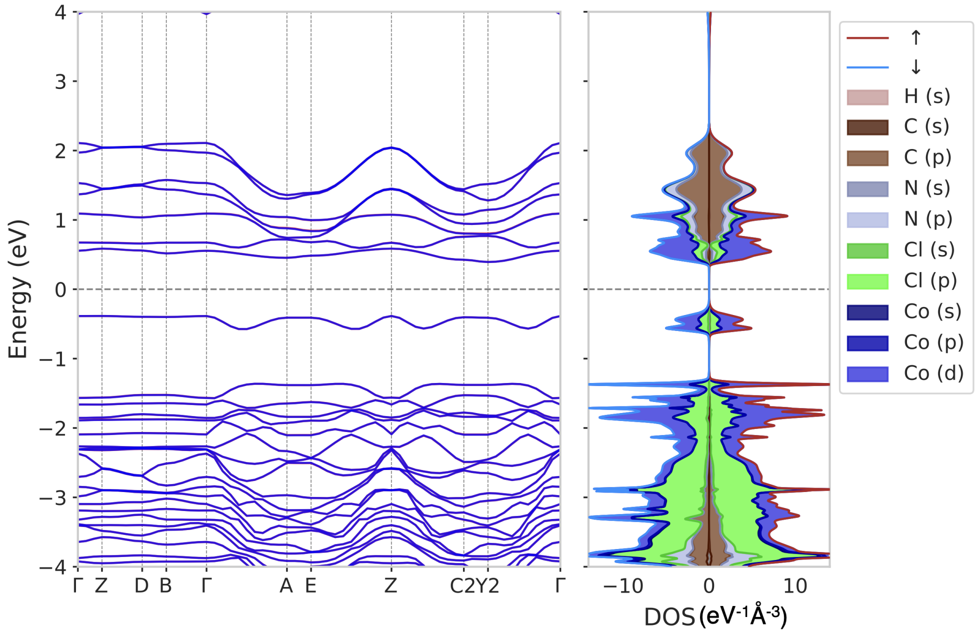

(c) Cobalt

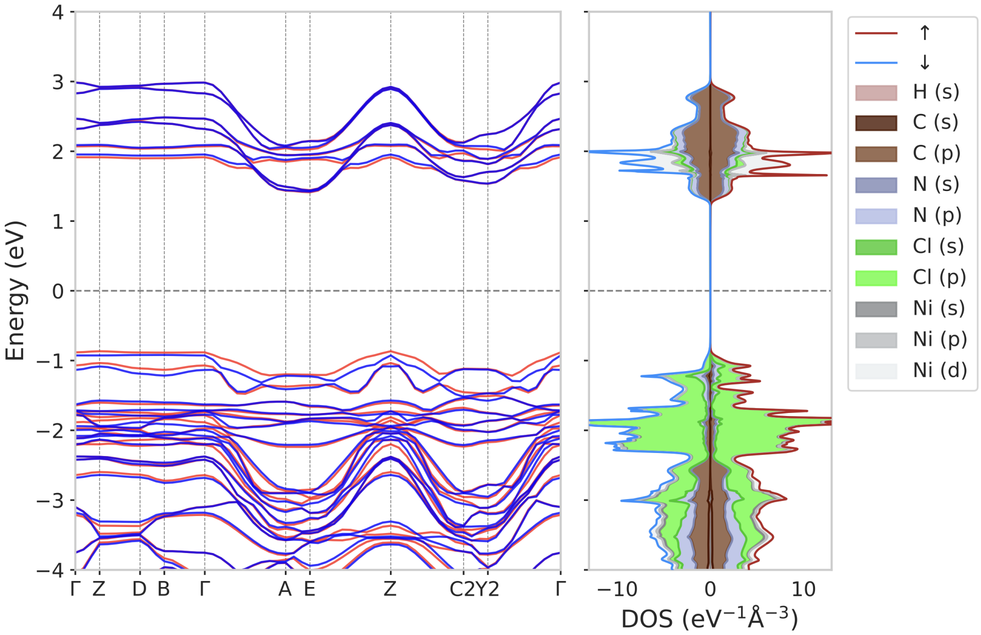

(d) Nickel

Figure 5.1: Band structure and density of states of $MCl_2(pym)$ where M = V, Fe, Co, Ni. DFT+U (U_{eff} = 2 eV for V and Fe, 4 eV for Co and 6 eV for Ni) calculated with the PBE exchange correlation functional and MBD* dispersion correction.

Similarities amongst the different metal ions are clearly noticeable. The highest occupied band near the Fermi level is primarily consisting of contributions from the metal M and Cl, while the pyrimidine structure is involved in the lowest unoccupied band right above the Fermi energy. These PDOS properties are in agreement with previous results for $CrCl2(pym)$. The band-structure results presented suggest that a similar semi-conducting nature persists amongst the structures hosting different transition metals.

The most interesting of these new metal-organic magnets is $NiCl_2(pym)$, which will be further explored. In contrast with other transition metals such as iron (II), which have a significant spin-orbit component masking finer quantum-mechanical properties, nickel based MOFs have not only sparked recent interest in the literature [189, 190], but also found various applications, such as catalysts for chemical fixation [191] or energy storage [192]. The advantages of nickel come from its high abundance, low cost and good thermal and chemical stability. One feature that makes it stand apart is its electron configuration, with Ni^{2+} having 8 d-orbital valence electrons.

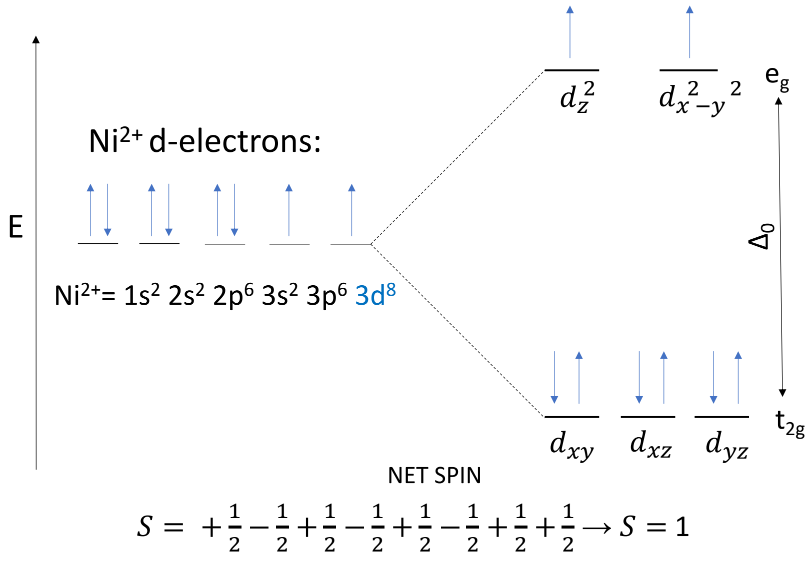

Figure 5.2: Crystal field splitting diagram of Nickel (II) in $NiCl_2(pym)$. Ni^{2+} has a net spin S = 1 without distinct high-spin versus low-spin configurations.

As shown in figure 5.2, Ni^{2+} undergoes crystal field splitting being in an octahedral complex, in which the t_{2g} energy level becomes completely filled by the 6 valence electrons with the 2 remaining electrons filling up the e_g level. Since it takes less energy for the 2 electrons to fill up the 2 available e_g states separately, this will always be the case and, unlike other transition metals explored such as Cr or Fe, no high-spin versus low-spin scenarios exist. In section 5.1.2, the electronic and magnetic properties of $NiCl_2(pym)$ will be investigated in greater detail.

5.1.2 The promising nature of $\mathbf{NiCl_2(pym)}$

The structural nature of the Ni analogue structure has been researched, especially since no experimental diffraction data is available for this novel structure. For reference, the geometrically optimised structure is shown in figure 5.3.

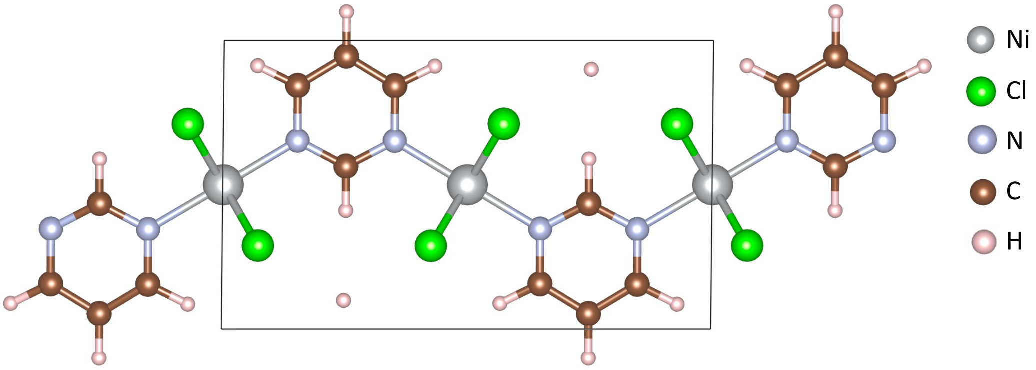

Figure 5.3: DFT + U ($U_{eff} = 6$ eV) geometry optimised structures of $NiCl_2(pym)$. MBD* dispersion correction has been implemented.

In contrast with $CrCl_2(pym)$, the nickel analogue shows no Jahn-Teller distortion. This is indeed expected, since no asymmetry is present in the d-orbital electron arrangement. Furthermore, this nickel analogue shows antiferromagnetic behaviour along the pyrimidine direction. The implication this has on the material properties is a rather complex question, which has challenged many researchers. Marcin M. Wysokiński [193] has shown that transitions between ferromagnetic and antiferromagnetic phases among some d-electron metallic magnetic compounds can be induced by altering the pressure of the system. With the power of computation, a ferromagnetic to antiferromagnetic transition has been induced in our system through the use of appropriate initial spins on the Ni atoms, which has then been relaxed throughout the DFT calculation. Figure 5.4 shows the band structure and density of states for both the ferromagnetic and anti-ferromagnetic arrangements.

When running spin polarised calculations, the DFT software package CASTEP allows to impose an initial spin on desired atoms. To achieve the results presented in figure 5.4, a spin of $\pm\frac{1}{2}$ has been imposed on each of the 2 Ni^{2+} ions, both with the same spin sign to recreate a ferromagnetic configuration and with opposite signs to recreate an anti-ferromagnetic configuration. During the DFT electronic energy minimisation process, the spin was fixed during the initial 10 SCF cycles, after which it was allowed to vary following the standard density-mixing electronic minimisation method, as previously explained in section 2.4.2. Results show that the induced ferromagnetic state is 5.44 meV higher in energy then the anti-ferromagnetic phase.

The band-gap does not change between the two distinct magnetic phases, meaning that the insulating nature is not altered. However, it is interesting to notice the change in dispersiveness of the blue band that has been arbitrarily labelled as spin down in figure 5.4. In the anti-ferromagnetic phase, the spin down valence band is dispersive around the gamma point between U2 and V2, whereas it becomes more localised in the ferromagnetic phase as its bandwidth is decreased. In either case, however, chlorine is the driving element involved in these valence bands.

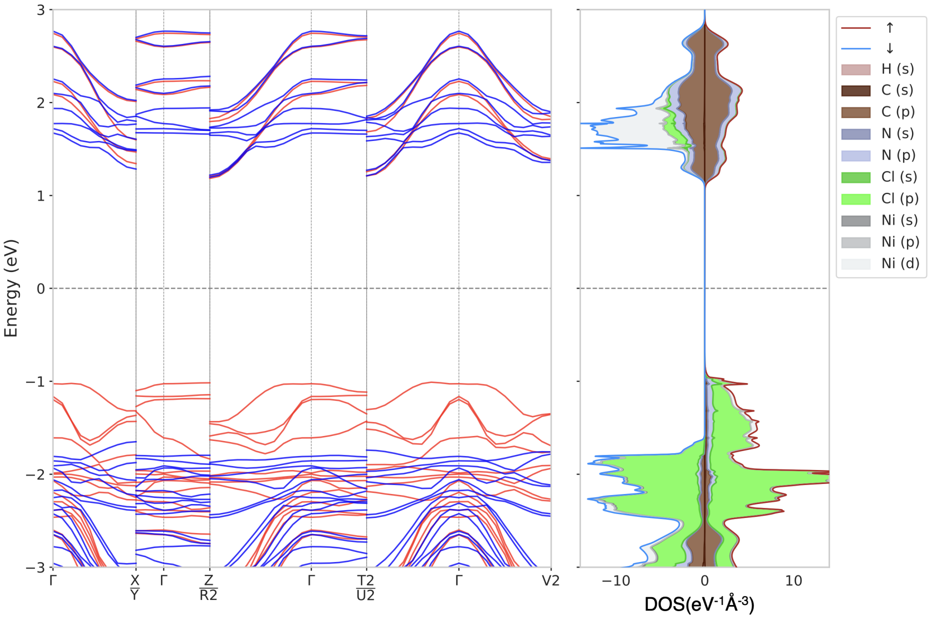

(a) FM configuration along the pyrimidine direction

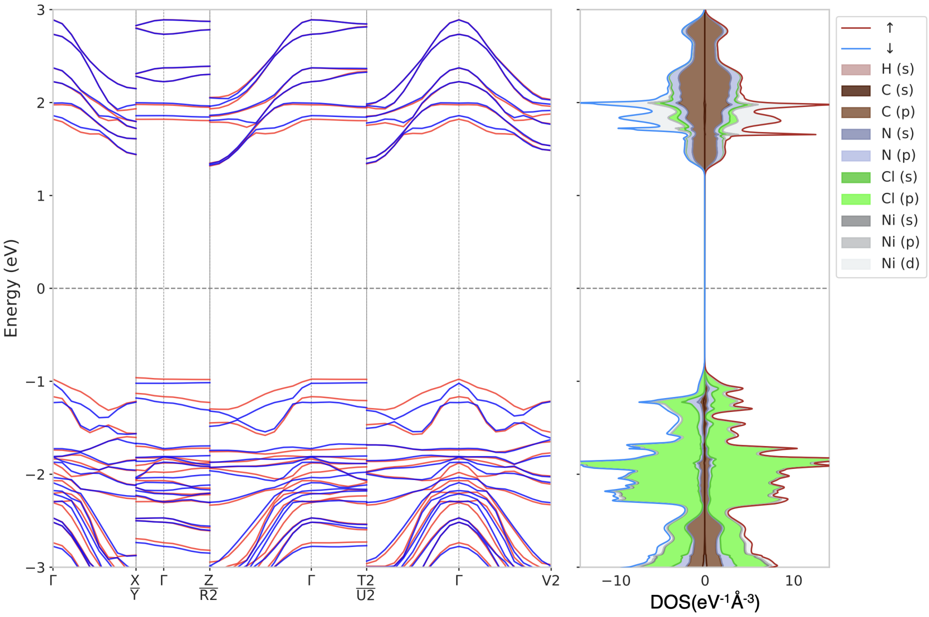

(b) AFM configuration along the pyrimidine direction

Figure 5.4: DFT+U ($U_{eff} = 6eV$) $NiCl_2(pym)$ band structure and density of states. Both the 5.44 meV slightly higher energy ferromagnetic (FM) arrangement and the anti-ferromagnetic (AFM) arrangement are shown for comparison. In these results, the same band-structure path through the Brillouin zone used for $CrCl2(pym)$ was adopted for direct comparison.

To gain a better understanding of the spin arrangement of the system, the spin density for the ground-state anti-ferromagnetic configuration has been calculated and presented in figure 5.5. The majority of the spin density is located around Ni and Cl. Since the spin density is a representation of the difference between the up and down spins, this result makes sense as the organic rings tend to have an equal number of up and down spins, whereas a transition metal such as nickel (II) with two unpaired electrons of parallel spin in the e_g will have a more significant spin density.

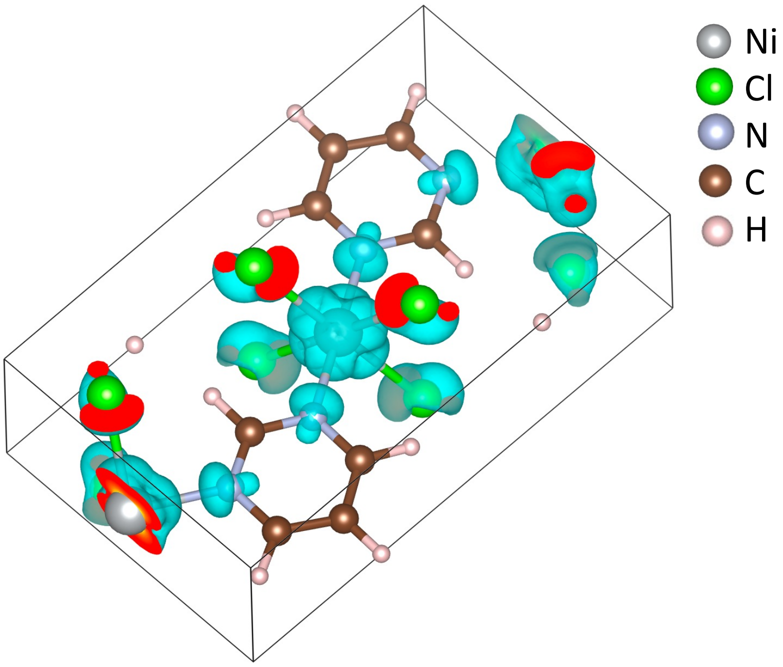

Figure 5.5: DFT+U ($U_{eff} = 6eV$) $NiCl_2(pym)$ spin density plot. The post-processing program c2x [101] has been used to generate this plot.

Although DFT+U results showed that the ferromagnetic phase is 5.44 meV higher than the anti-ferromagnetic phase, in order to analyse the strength of these magnetic properties, investigate the correlation present and explore the magnetic exchange mechanisms, a 2x2x1 supercell has been developed. The magnetic exchange results are shown in 5.6.

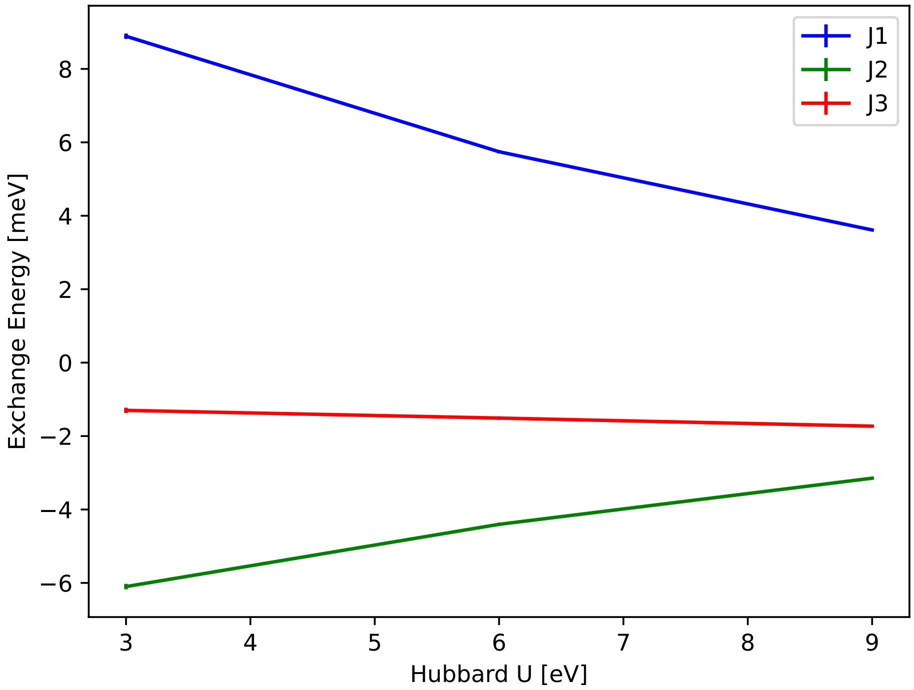

Figure 5.6: $NiCl_2(pym)$ magnetic exchange. A Hubbard U correction range between 3 eV and 9 eV has been tested. The J_1, J_2 and J_3 values are along the $NiCl_2$ chain, the bridging pyrimidine, and between adjacent layers respectively. Positive values correspond to a ferromagnetic exchange interaction, whereas negative values correspond to an anti-ferromagnetic exchange interaction.

Figure 5.6 shows that $NiCl_2(pym)$ is ferromagnetically bound along the $NiCl_2$ spin chain with $J_1 = 5.74$ meV (U = 6 eV) and anti-ferromagnetically bound along the bridging pyrimidine direction with $J_2 =$ -4.40 meV (U = 6 eV). The exchange between the layers J_3, although relatively weak compared to J_1 and J_2, favours an anti-ferromagnetic exchange with $J_3 =$ -1.51 meV (U = 6 eV). The supercell results match with the results presented in section 5.1.2, which showed that an antiferromagnetic configuration of the nickel ions along the bridging pyrimidine direction (J_2) is preferred with respect to its ferromagnetic counterpart, with an energy difference of 5.44 meV.

Looking at the x-axis of figure 5.6, as we increase Hubbard U, the exchange values decrease towards zero. This is expected, as a U correction adds a Hubbard repulsion energy term to the normal DFT energy, resulting in the localisation of the orbitals, thus decreasing the exchange interactions. The chosen $3 \leq U \leq 9$ range is appropriate as the exchange nature is consistent throughout.

Comparing results with $CrCl_2(pym)$ shown in figure 3.10 of chapter 3, a clear difference can be noticed. J_1 and J_2 are AFM and FM in the chromium analogue, the opposite of the nickel based structure. This is an interesting discovery in the MOF world with different applications, as it paves the path to the achievement desired magnetic properties. Increasing the atomic number of transition metal ions shifts the magnetics of the system towards antiferromagnetic arrangements. It is also interesting that if the material is ferromagnetic in one of the strong exchange directions (J_1 or J_2), the other exchange direction changes nature to maintain the lowest possible energy. Apart from the sign of these exchange interactions, their magnitudes agree in J_1 being larger than J_2, although they are proportionally different. $J_1/J_2 = 1.3$ for the nickel analogue and $J_1/J_2 = 8.4$ for the chromium analogue, suggesting that the chromium analogue is closer to a quasi-one-dimensional system and therefore more suited for developing low dimensional materials, such as the ones with the potential to host and test for the S=2 Haldane phase.

The effects of changing the metal ion on the electronic and magnetic properties have therefore been explored. Work carried out on tuning optical properties of MOF-based thin films by Wenchang Yin *et al.* [194] suggests that changing the ligand actually has a greater effect on MOF properties, such as conductivity, rather than changing the metal. This suggests that if one is working towards the discovery of new materials with a wide potential of new properties, one should not limit itself to only changing metals. The last part of this work attempts the discovery of new materials by changing the organic ligand.

5.2 Discovering new structures by changing organic linker

In the field of MOF research, the chemical design space is a combination of metal nodes, organic linkers, pore geometry and functional groups [195]. This final section of the research centres its focus on the organic part of MOFs. DFT is an invaluable tool in the development of new MOF structures with different organic linker, as it allows for the calculation of the electronic density of a system, which can be used to determine the spatial arrangement of atoms and predict the chemical bonds present in a material. This is particularly useful when working with new linkers as it allows researchers to predict the geometry of the new system. The power of DFT based structure prediction lies in the ability to explore the nature of complex electronic states arising form the interplay of the four fundamental degrees of freedom: charge, spin, orbit and lattice.

5.2.1 Predicting structures of novel quantum materials

Organic linkers are responsible for dictating many electronic properties of MOFs and play a major role in the discovery of new materials[196]. When exploring new organic linkers, a balance must be met between innovation and structural stability. To maintain structural stability with a similar overall topology, heterocyclic compounds should be maintained as new organic linkers in regards to our class of MOFs, and a good set of candidates consist of the diazines. The diazines are a group of organic compounds containing a benzene ring, in which two of the C-H fragments have been replaced by isolobal nitrogen. There are 3 distinct compounds belonging to this family, all with the same chemical formula $C_4H_4N_2$, which are: pyridazine, pyrimidine, pyrazine. In this final part of the research, *ab initio* crystal structure prediction has been carried out using the pyridazine (pydz) organic linker to create the new metal-organic structure $CrCl_2(pydz)$.

5.2.2 Structure prediction using the Wyckoff alignment of molecules

Structure prediction is a complex yet promising field of computational research, which has led to the discovery of many novel structures over the recent years. Carrying out *ab initio* random structure searching [197] calculations only require basic input information, namely reasonable material densities and atomic separations, from which random structures are created and then relaxed with a geometry optimisation. Since 99.5% of MOFs reported in the Cambridge Structural Database (CSD) have some level of symmetry [198], symmetry has been imposed in our structure search via the Wyckoff alignment of molecules code (WAM) [199]. WAM drastically improves the efficiency of *ab initio* random structure searching through the use of symmetry by exploiting Wyckoff sites, therefore reducing the dimension of the search space and simplifying the geometry optimisation. The code generates trial structures by randomly placing atoms or molecules on the Wyckoff sites of a random unit cell, commensurate with a random space group. Two types of Wyckoff sites exist: the general site, which has no symmetry, and special sites, which have symmetry. WAM, therefore, makes use of these special sites to generate structures with varying levels of symmetry. Once an object is placed on a Wyckoff site, that object will stay on that site when the cell is then geometrically relaxed. Further details and an outline of the WAM algorithm can be found at [199].

In this work, novel structures have been generated both computationally and in collaboration with the experimental researcher Matthew J. Cliffe from the University of Nottingham. The Wyckoff alignment of molecules approach was taken in combination with previously known structures containing pyridazine linkers. Over 1,000 structures were generated and geometry optimised. These structures have been evaluated according to their energies, from which a histogram plot has been created and presented in figure 5.7.

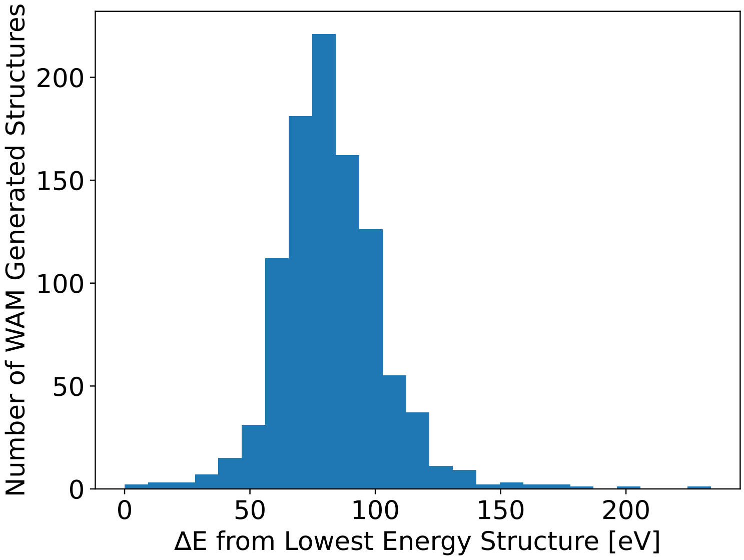

Figure 5.7: Histogram showing the number of structures generated by the WAM code as a function of their ground-state energy. The histogram implements 25 bins of width 9.35 eV.

As part of the WAM inputs, the pyridazine ring structure was defined with the position of the $C_4H_4N_2$ atoms. In the overall, multiples of 2 Cr, 4 Cl and 2 pyridazines were given as inputs, to be randomly placed following WAM's internal symmetry criteria. Almost all of the generated structures would not exist in the physical world because they are not stable structures. The 6 lowest energy optimised structures found are presented in figure 5.8.

Out of the many structures found, the structure presented in figure 5.8a follows the expected MOF chemistry with a Cr^{2+} ion surrounded by 2 Cl^{-} and 2 organic heterocyclic compounds. As often seen is such materials, a Cl ions bridge is formed. However, a slightly modified structure, shown in figure 5.8c, is lower in energy when compared to figure 5.8a's supercell containing the same number of atoms. The metal ion in such arrangement takes an octahedral molecular geometry with the surrounding Cl ions and one N from the pyridazine. Such octahedral molecular geometry is also seen in structure 5.8f, although this structure has a higher energy with respect to structure 5.8c.

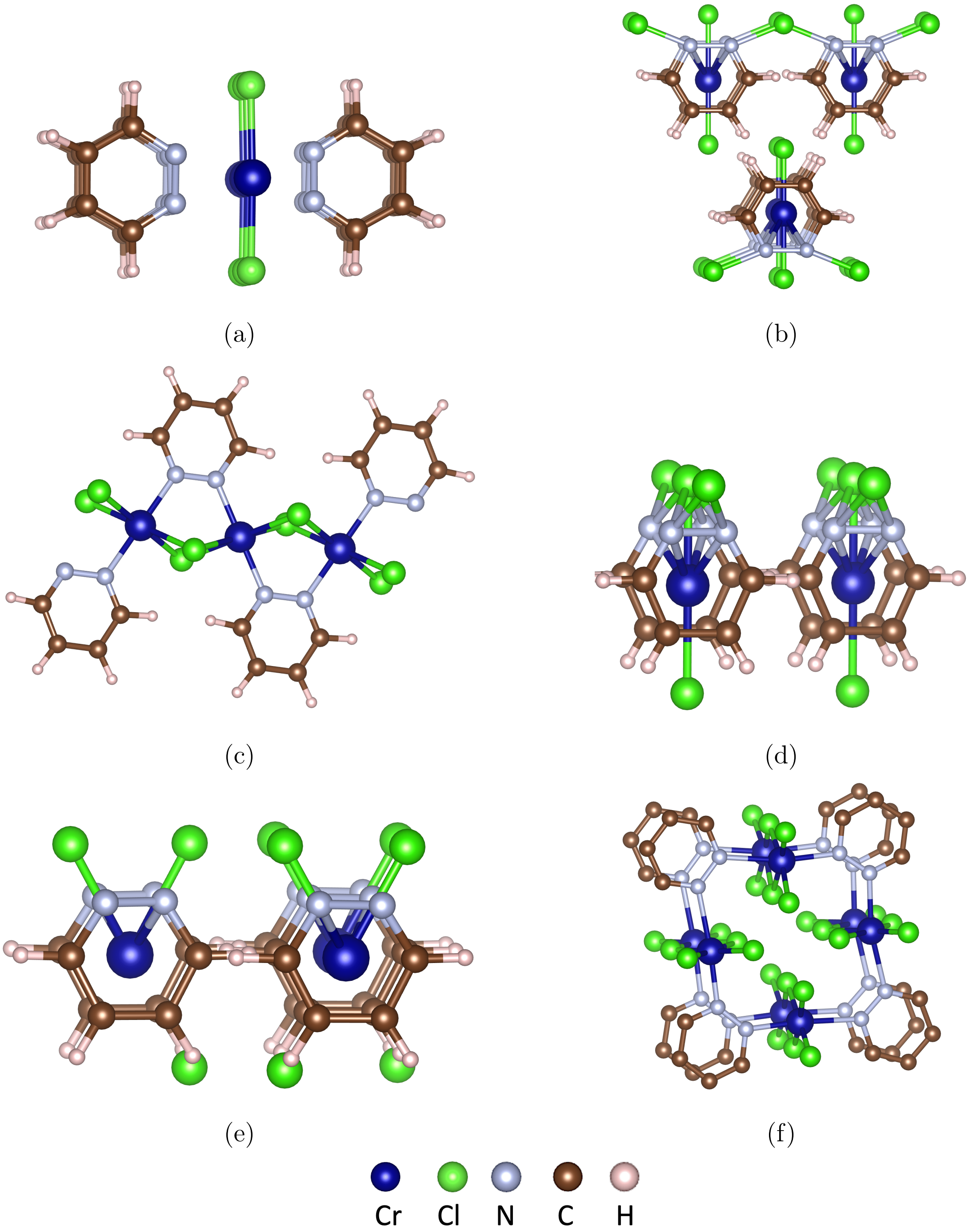

Figure 5.8: Structure searching results of $CrCl_2(pydz)$. Over 1,000 structures have been generated by WAM, and the 6 lowest energy optimised structures are presented in this figure. Structure (c) is the lowest energy structure found.

After a suitable structure has been found, a more accurate geometry optimisation has been carried out, with better k-point spacing of 0.05 $2\pi/\text{Å}$ and energy cut-off of 1100 eV, along with the inclusion of MBD* dispersion corrections. Being this a quantum material characterised by strong correlations, a Hubbard U is needed, and previous research has shown that a value of U = 3 eV is expected to be suitable for Cr^{2+} in these MOF materials under similar conditions. The geometry optimisation results for 3 Hubbard U values are shown in table 5.2.

U Value [eV]	Volume [Å^3]	Density [amu/Å^3]	Lattice Parameters [Å]			Cell Angles			Cr-Cl Bond Lengths [Å]			
			a	b	c	α	β	γ	Cr atom 1		Cr atom 2	
0	302.88	1.34	7.97	7.97	6.54	113.1	113.1	105.8	2.40	2.41	2.40	2.41
3	320.60	1.26	7.98	7.86	6.88	112.7	111.9	106.1	2.41	2.83	2.41	2.86
6	322.15	1.26	8.02	8.02	6.89	113.2	113.2	105.6	2.49	2.70	2.48	2.70

Table 5.2: Summary of PBE+U+MBD* geometry optimisation results using different Hubbard U values. Ultrasoft pseudo-potentials have been used. A Hubbard U = 3 eV is confirmed to be a suitable value, able to capture the Jahn-Teller distortion. A cut-off energy of 1100 eV has been used with a k-point spacing of 0.05 $2\pi/\text{Å}$ and a Gaussian smearing scheme with a 0.2 eV smearing width. The Broyden density-mixing scheme has been used throughout the optimisations.

It is indeed seen that with a Hubbard U = 3 eV an appropriate Jahn-Teller distortion is captured. Increasing the Hubbard U values results in an increase in volume, with a more drastic change of 17.72 Å^3 between U = 0 eV and U = 3 eV compared to a change of 1.55 Å^3 between U = 3 eV and U = 6 eV, agreeing with expectations that the U = 3 eV and U = 6 eV range is more suitable for this material. Each chain is connected with adjacent chains through van der Waals forces. The geometry optimised structure is shown in figure 5.9. One noticeable difference between this structure and its pyrimidine analogue lies in the direction of the chromium - chloride bonds. In the pyrimidine based MOF these bonds connect with other chlorides in the direction perpendicular to the organic ring structure, keeping the different layers together, whereas in the pyridazine they connect with other chlorides along the direction of the ring structures. This is caused by the difference in nitrogen locations, and might have repercussion in the stability of the material. The chromium-chloride bonds are not present in the new structure to keep the different layers together, and van der Waals forces become the dominant source of bonding.

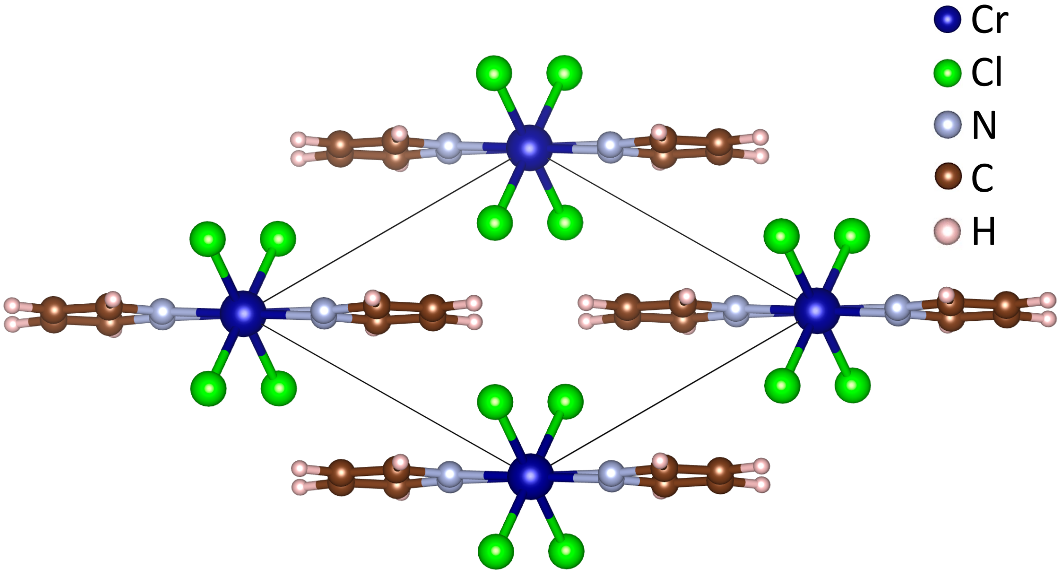

Figure 5.9: Geometry optimised $CrCl_2(pydz)$ structure. DFT+U ($U_{eff} = 3$ eV) has successfully generated a structure containing Jahn-Teller distortion.

The difference in nitrogen locations resulted in the chromium ions being closer to each other, potentially increasing the exchange interactions along the organic ring structure and decreasing them in the other directions. The new bonding arrangement might also have an impact on the overall electronics of the system. To explore these electronic and magnetic properties, band-structure and density of states calculations of this novel quantum material have been calculated and presented in the remainder of this chapter, as well as magnetic exchange calculations.

5.2.3 Electronic structure and properties

The electronic band-structure and density of states of $CrCl2(pydz)$ have been calculated using DFT+U ($U_{ff} = 3$ eV). To accurately achieve this result, both the electronic and magnetic ground states of the system have to be attained. The electronic ground state is reached via DFT's SCF cycles, whereas the magnetic ground state has been accomplished via the use of a super-cell and appropriate spin textures. Similar to the approach taken in section 5.1.2, the spin was fixed during the initial 10 SCF cycles of the electronic energy minimisation process, after which it was allowed to relax. The details of the magnetics of the system are later explained in section 5.2.4.

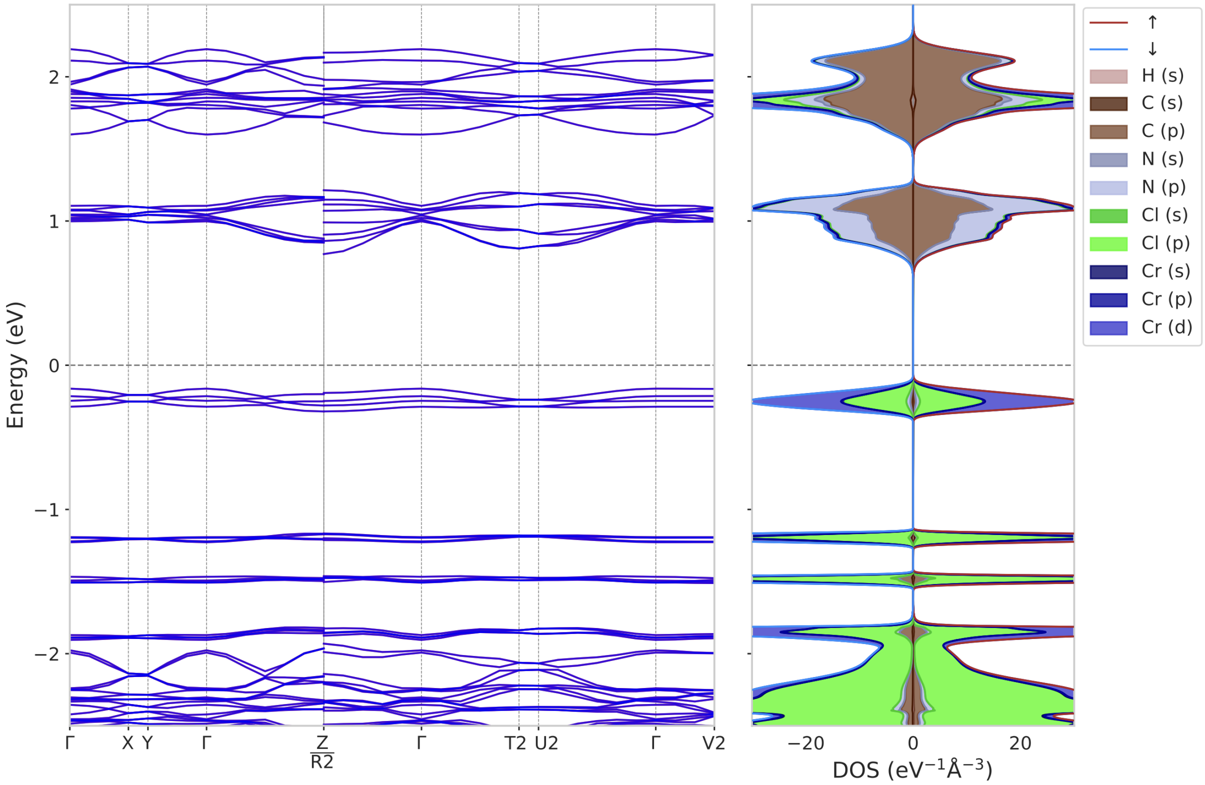

Figure 5.10: DFT+U ($U_{ff} = 3$ eV) $CrCl_2(pydz)$ band structure and density of states. A 2x1x1 super cell has been used to achieve the anti-ferromagnetic ground state.

Figure 5.10 demonstrates that the electrons in this structure are primarily localised, with 4 bands under the Fermi energy, showing very little dispersion. A set of 4 spin up and 4 spin down bands are located just below the Fermi energy. Looking at the DOS, these mostly correspond to Cr (d) states and Cl (p) states, conforming to the highest occupied crystal orbital. This is similar to the pyrimidine analogue, as shown in figure 3.11. The conduction bands, on the other hand, correspond to the pyridazine. These bands above the Fermi energy show a more dispersive behaviour, especially following the R2 - Γ - T2 path.

Being a quantum material, a Hubbard U correction of 3 eV was used to account for the strong electron correlations. This resulted in a band-gap of 0.97 eV, showing an insulating nature. This is slightly less than the 1.2 eV band gap of the pyrimidine analogue, also showing insulating properties. To visualise the electronic behaviour, the Kohn-Sham orbitals have been calculated.

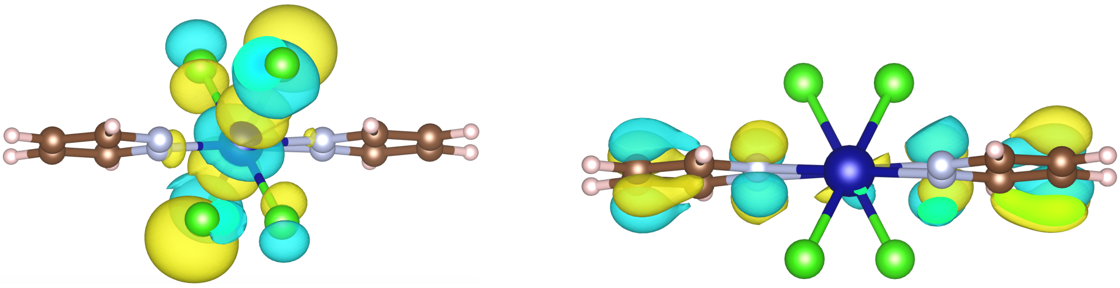

(a) Highest occupied crystal orbital (b) Lowest unoccupied crystal orbital

Figure 5.11: Kohn-Sham orbitals of $CrCl_2(pydz)$ calculated with DFT + U ($U_{eff} = 3$ eV). The orbital isosurface has been post-processed with c2x [101] and visualised with VESTA [113]. Band 232 with an occupancy of 0.90 corresponds to the highest occupied Kohn-Sham orbital, whereas band 233 with an occupancy of 0.00 corresponds to the lowest unoccupied Kohn-Sham orbital.

As expected from the band-structure and density of states analysis, the highest occupied crystal orbital is centred around the chromium and chloride ions, whereas the lowest unoccupied crystal orbital is centred around the pyridazine. This is similar to the pyrimidine analogue, as seen in figure 3.12, and confirms the validity of this novel material from a chemical point of view. In the next section, the magnetic behaviour of the system is explored.

5.2.4 Magnetic properties

In quantum materials, correlations play a major role in their properties, which are evaluated in this section. As opposed to the pyrimidine analogue with 3 J_n values, following a nearest neighbour approach we find only 2 exchange directions for $CrCl_2(pydz)$, denoted as J_1 and J_2 in figure 5.12. This is due to the symmetry of the system.

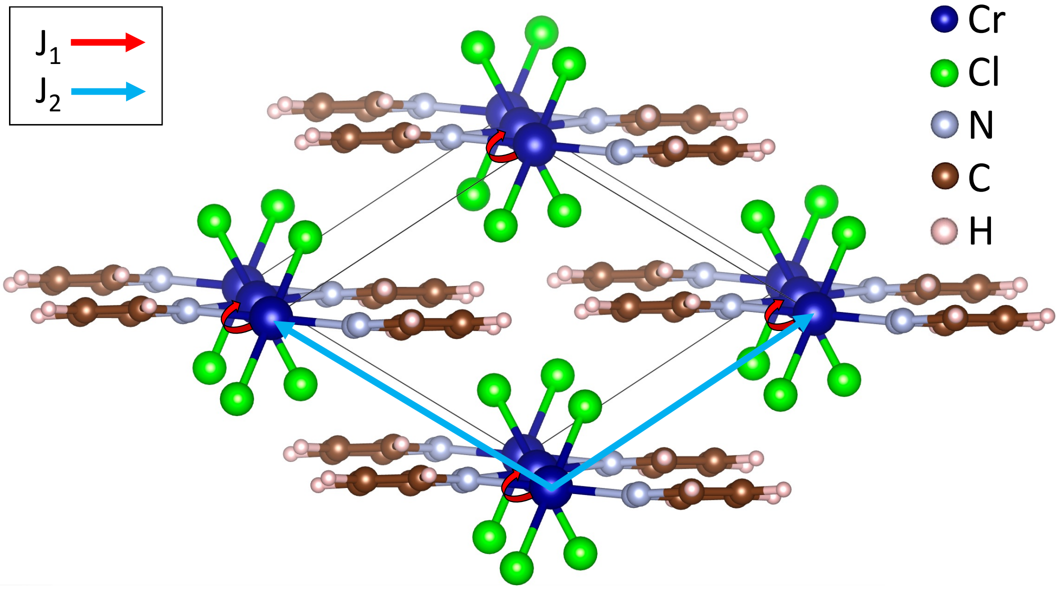

Figure 5.12: Visualisation of J_n exchange directions of $CrCl_2(pydz)$. J_1 is along the pyridazine and chromium-chloride bridge; J_2 is towards corresponding the chromium of adjacent strands, along the cell's lattice.

The exchange values have been calculated using different spin arrangements in regards to the chromium ions by making use of a $2 \times 2 \times 1$ supercell. With two J_n exchange values, 4 possible arrangements of FM or AFM combinations can be achieved. The energies have been reported in table 5.3. A Hubbard U correction has been implemented in these calculations with 3 distinct values of U.

Magnetic Exchange		Magnetic Configurations Relative Energies [meV]		
J1	J2	U = 3 eV	U = 6 eV	U = 9 eV
AFM	AFM	Magnetic ground state		
AFM	FM	6.30	6.37	6.18
FM	AFM	189.48	90.01	31.04
FM	FM	206.27	104.34	37.80

Table 5.3: DFT ground state energies for the different possible magnetic configurations. All energies are recorded with respect to the lowest energy magnetic configuration. The reported energy values are relative to the $2 \times 2 \times 1$ supercell. The ground state magnetic configuration of the system is antiferromagnetic in all directions.

Table 5.3 shows that the magnetic ground state configuration of the system is antiferromagnetic in all directions. There is a considerable difference in strength between J_1 and J_2, with J_1 being clearly dominant. There is a relatively low difference in energy between the two antiferromagnetic J_1 configurations, as seen in the first two rows of the table, since J_2 is relatively weak in comparison. This suggests that if thermal energy is induced in the system, the antiferromagnetic arrangement between different strands (along J_2) will be lost before the antiferromagnetic magnetisation within each strand (along J_1). In other words, the different strands will lose their correlation while it is maintained within each strand.

The magnitudes of the J_n values have been calculated using a linear fit to the Heisenberg Hamiltonian, similar to chapter 3. The exchange at three values of U has been investigated, with U = 3 eV, 6 eV and 9 eV. The results are shown in figure 5.13.

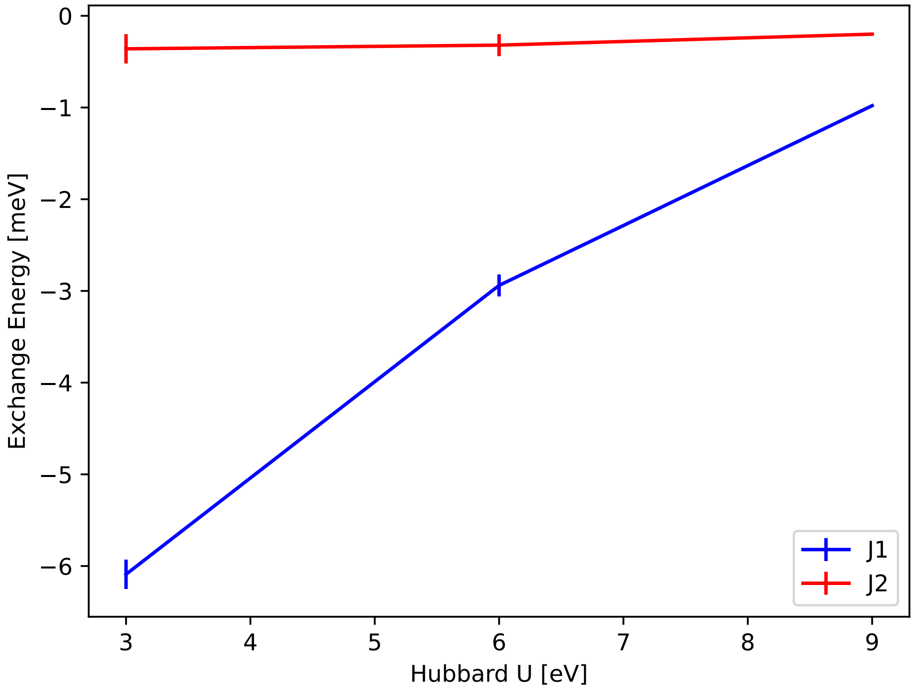

Figure 5.13: $CrCl_2(pydz)$ magnetic exchange interactions J_n with respect to Hubbard U parameter. Each of these energies were calculated using DFT+U from a set of spin configurations and a multidimensional linear regression was used to fit these values to a Heisenberg Hamiltonian.

As expected, both J_n are negative, corresponding to an antiferromagnetic configuration. This is different from the pyrimidine analogue, as shown in 3.10, in which the magnetic ground state is antiferromagnetic in two of the three directions and ferromagnetic in the other. In the pyrimidine analogue, J_2 is positive; however, it is essential to keep in mind that J_n values in the different materials correspond to different directions.

In the pyridazine analogue dealt in this chapter, the exchange along J_1 = -6.09 meV (U = 3 eV) hosts significantly stronger correlations relative to the exchange along J_2 = -0.36 meV (U = 3 eV) compared to the J_1/J_2 ratio of the pyrimidine analogue. It can be concluded that $CrCl_2(pydz)$ is indeed a quasi-one-dimensional system, with $J_1/J_2 = 16.92$, clearly over the quasi-one-dimensional conventional defining value of $J_1/J_2 \geq 10$. The cause of this lies in what contributes to the magnetic exchange. In the pyridazine analogue, both the superexchange along the pyridazine and the exchange across the chromium-chloride bridge contribute to J_1, resulting in strong correlations. These two exchange mechanisms are along different directions in the pyrimidine analogue, respectively occurring along J_2 and J_1. On the other hand, J_2 in the pyridazine analogue is significantly weaker compared to J_2 of the pyrimidine structure. In the pyridazine analogue, J_2 is along the direction of the van der Waals forces which hold the different layers together, and no magnetic exchange mediator is found between these layers, similar to J_3 in the pyrimidine structure.

These magnetic results are very promising, especially the exchange ratio $J_1/J_2 = 16.92$ which suggests the possibility for having finally found a material which can host the S = 2 Haldane phase without obscuring its existence. Unlike the pyrimidine analogue, the pyridazine framework offers a J_2 which is likely to be sufficiently small to prevent it from masking the Haldane phase. Of course, other parameters such as single ion anisotropy or Néel temperature also need to be adequate to prevent the suppression of the Haldane phase, but this is left for experimental researchers to investigate by synthesising such material and hopefully observing this unrealised topological phase of matter.

Despite having different magnetic exchange ratios, the underlying source of the magnetism does not however change, as seen in the spin density plot shown in figure 5.14. The majority of the spin density is located around the chromium (II) ion, which is expected due to its ionic charge. This is responsible for driving the overall magnetism of the system. The chlorides and nitrogen atoms also contribute in the magnetism, although to a far lesser extent.

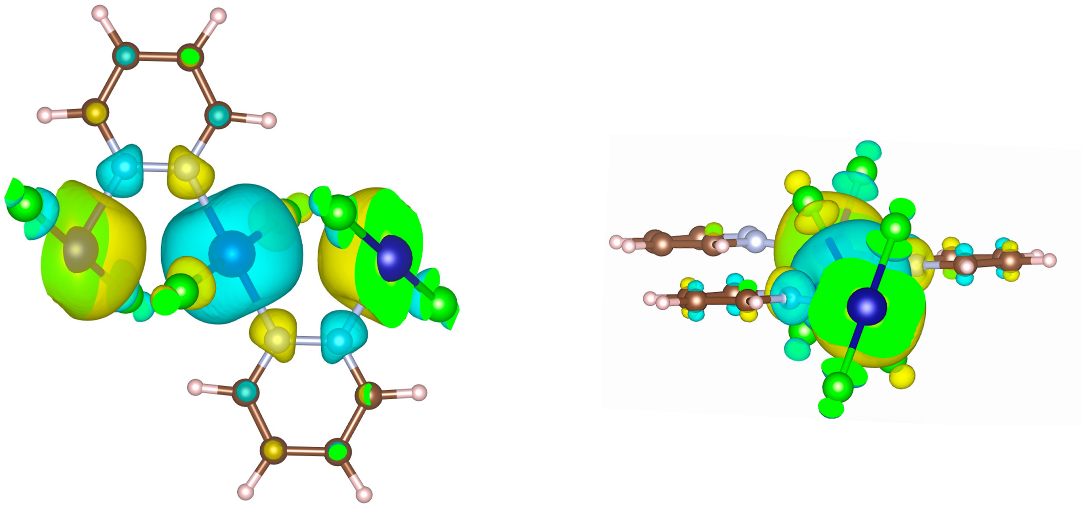
(a) Top view

(b) Side view

Figure 5.14: Visualisation of the $CrCl_2(pydz)$ spin density, both from a top and side view. The calculation was carried out with DFT + U (U_{eff} = 3 eV). The spin density has been post-processed with c2x [101] and visualised with VESTA [113].

5.3 Conclusions

The quest for new quantum materials drove the research in this chapter, and led to the discovery of new metal-organic systems. Starting from the previously studied structure in Chapter 3, $CrCl2(pym)$, a series of new transition metals have been investigated and a trend along the organic linker direction has been found: as we transition across the period of the periodic table, the systems shift from a ferromagnetic to an antiferromagnetic arrangement. Special attention has been given to $NiCl2(pym)$, showing a ferromagnetic J_1 and antiferromagnetic J_2, the opposite of its chromium analogue. The band-structure and magnetic analysis carried out on these novel structures resulted in a deeper understanding of this class of materials with great potential. With a wide application potential, from spintronics to nanotechnology [200], this class of materials is growing in popularity.

In the second part of this chapter, structure searching has been carried out using the Wyckoff alignment of molecules code (WAM) on $CrCl_2(pydz)$. Over 1,000 structures have been generated, and the most realistic one has been studied in detail. In such structure, an overall localised band-structure has been identified, with a band gap of 0.97 eV. The highest occupied crystal orbital has been found around the chromium-chloride region. The magnetism of this system has been carefully investigated, and it was discovered that this material is characterised by an antiferromagnetic arrangement in all directions. According to the magnetic exchange J_n ratios, $J_1/J_2 = 16.9$ for $U_{eff} = 3$ eV, the system is quasi one-dimensional. This promising result suggests the possibility that a material able to host the long-searched S=2 Haldane phase has finally been found.

From a broader perspective, low dimensional materials, such as the one discovered above, have a wide range of applications outside the scientific community. In the IT sector, such materials pave the way towards more energy-efficient memory devices and quantum computing [201, 202]. For instance, the manipulation of the spin texture can be used towards data storage. Provided appropriate anisotropy of the system, a small external magnetic field can be applied to bring the different adjacent strands in ferromagnetic or antiferromagnetic configurations with respect to each other, while always keeping a robust antiferromagnetic arrangement within the individual strands.

In the overall, the analysis carried out on these novel structures have shed light on the geometry that such metal-organic frameworks could take, as well as their electronic and magnetic properties. These findings provide a more comprehensive understanding of this class of quantum materials and contribute towards the future development of new ones.

Chapter Six

Conclusion and Outlook

This thesis has focused on investigating the properties of quantum materials and, specifically, materials exhibiting strong electron correlations and non-conventional magnetism. *Ab initio* plane-wave DFT calculations have driven the explorations carried out in this work, and, after appropriate integration with modelling techniques, corrections and parameters, it was found to be an effective approach in calculating the electronic and magnetic properties of these materials. The key role of d-orbital electrons and their correlations in driving the physical traits exhibited by these quantum materials has become evident throughout this study. A Hubbard U correction has been used to model the d-orbital electrons correctly and capture the driving physics behind these quantum systems. Two promising materials have gained the central focus of the research, the first being the $CrCl_2(pym)$ metal-organic magnet, a candidate structure for the S=2 Haldane phase, and the second being $Cu_4(OH)_6FBr$, a candidate structure for the quantum spin liquid phase.

Chapter 3 has focused on studying the properties of coordination frameworks. These systems have the potential of creating low-dimensional structures and act as templates to search for topological phases of matter, such as the Haldane phase in our case. In particular, the $CrCl_2(pym)$ metal-organic magnet has been selected, being a novel low dimensional

S = 2 antiferromagnetic system meeting all the criteria to recreate the Haldane phase. According to crystal field theory, when chromium (II) is placed in an octahedral complex, d-orbitals splitting between the e_g and t_{2g} bands is expected, with the presence of Jahn-Teller distortion. This distortion was met in the model by adding a Hubbard U = 3 eV correction to the geometry optimisation of the system. The band structure and density of states have been successfully calculated and show a band gap of 1.2 eV. The magnetic nature of this material was investigated, and it was discovered to be antiferromagnetically bonded through the chromium-chloride chain and ferromagnetically bonded through the pyrimidines. The exchange values were calculated and found to be $\mathrm{J}_1 = -2.53\,\mathrm{meV}$, $\mathrm{J}_2 = 0.30\,\mathrm{meV}$ and $\mathrm{J}_3 = -0.09\,\mathrm{meV}$, all in good qualitative agreement with experimental results. It was therefore concluded that J1/J2 = 8.4, suggesting that this is approaching the quasi-one-dimensional threshold of $J_1/J_2 \geq 10$, required to see the Haldane phase. This material, therefore, does not fully achieve this requirement and then the Haldane phase is suppressed. The DFT techniques developed to manipulate the spin states of this material have proved to be a powerful tool to investigate its magnetic properties and have been applied in the rest of this work.

Chapter 4 has focused on the mineral barlowite, which has been selected as a quantum spin liquid candidate, with the chemical formula $Cu_4(OH)_6FBr$. Barlowite meets all the theoretical requirements for exhibiting a quantum spin liquid nature, being a frustrated magnet with an adequately small spin of $S = \frac{1}{2}$. Barlowite contains structural disorder with different possible crystal geometries. $Pnma$ and $P6_3/mmc$ are two space groups commonly reported for this material, and DFT has successfully relaxed the system in these symmetries. In regards to the geometry of the system, it was found that the medium-close distance between disordered copper sites results in the lowest energy configuration of the system. DFT + U (U_{eff} = 5 eV) calculations found a band gap of 0.56 eV, confirming its expected insulating nature. The bromine halide has been exchanged with chlorine and iodine creating claringbullite [$Cu_4(OH)_6FCl$] and iodide-substituted barlowite [$Cu_4(OH)_6FI$] respectively and similar electronic behaviours were seen. Additionally, barlowite's magnetism was also explored and J_1 = -2.2 meV and J_2 = -10.6 meV were found. To study the frustrated magnetic nature present in this material, non collinear DFT was carried out. Spin-orbit coupling opened a new direction of research to compute spin and related magnetic properties in materials experiencing magnetic frustrations. Despite the possibility of this material entering the quantum-spin liquid phase, computational results categorised this material as a valence bond crystal. DFT spin calculations outputs are in good agreement with experimental data.

Building on the research techniques fine tuned in chapters 3 and 4, a search of novel quantum materials was carried out in chapter 5. Starting from the $CrCl_2(pym)$ metal-organic framework analysed in chapter 3, the chromium was exchanged with a series of different transition metals, including vanadium, iron, cobalt and nickel. Nickel, being the most interesting of these materials, shared many similarities with its chromium analogue, such as its insulating and strongly correlated nature. The magnetism of this nickel analogue was explored and magnetic exchange parameters showed a ratio $J_1/J_2 = 1.3$, far smaller than its chromium analogue.

On top of testing new transition metals, a new organic ligand, pyridazine, was also investigated. Structure searching using the Wyckoff alignment of molecules code was carried out. A large number of structures were generated, although almost all of them were high-energy non-stable structures. After appropriate analysis and geometry optimisations, a novel $CrCl_2(pydz)$ structure was achieved. The band-structure of this system showed a band gap of 0.97 eV, with relatively flat valence bands, corresponding to localised d-state of chromium. This new material was confirmed to be quasi-one-dimensional, with $J_1/J_2 = 16.92$. This is a promising result, suggesting that the DFT tested requirements to host the S = 2 Haldane phase are met and this structure is ready to be physically synthesised and experimentally proven.

There are a number of directions along which the research presented in this work can be extended and built upon. DFT calculations on low dimensional coordination frameworks have proven that these materials can be effective templates to search for topological phases of matter, as such materials are versatile and enable the recreation of specific desired properties. Although the S = 2 Haldane phase has still not been confirmed and experimental investigations will be required to make such discovery, DFT calculations can play a role in further validating the feasibility of this material for such objective. The non-collinear spin calculations developed to study frustrated magnetism can be extended to test for the single-ion anisotropy in the novel $CrCl_2(pydz)$ material, although the specific technique to achieve this has to be developed and tested. In addition, molecular dynamic calculations can be included in this study to investigate temperature dependent properties, important for magnetism, such as Néel temperature. On a separate note, in regards to barlowite, the structural disorder of the Cu^{2+} sites should be investigated using phonon calculations on top of energy calculations. In order to assess dynamical stability, phonon frequencies should be calculated both computationally and experimentally and results should be compared to provide a more comprehensive study of the disorder.

A number of fundamental questions deserve further investigation, such as how disorder alters quantum spin liquids, and mimic or destroy the quantum liquid state. A 2023 study [203] led by Brown University suggests that a new phase of matter may be formed, being a decorrelated version of the quantum spin liquid phase, in which smaller coherent quantum spin liquid "domains" are formed throughout the material. How such behaviour would manifest in systems like barlowite and its derivatives is not known.

Another question, this one focusing on the metal-organic coordination frameworks, is how introducing different transition metals within the same metal-organic framework, with different proportions, affects the stability, geometry, electronic and magnetic properties of the material. This is relevant to future IT, which will rely on new materials capable of switchable and stimuli-responsive behaviour. Therefore, how different combinations of metals and their interplay with the topology of the system can help to achieve these goals is a promising field, full of opportunities.

On top of the scientific advances, a series of lessons can also be learnt from the scientific journey underpinning this work. One such lesson is to be aware that, in the case of computational research, it is essential to choose an appropriate computational approach, to be commensurate with the level of science under investigation. It is often advantageous to avoid overly complex computational methods, as they frequently come with restricted applicability and high computational cost. In this research, dynamical mean-field theory was not implemented as DFT+U was adequate for calculating the electronic and magnetic results of interest, thus avoiding all the complexities of beyond-DFT methods.

The most scientifically accurate and robust models are often directly based on the fundamental laws of physics, such as quantum mechanics in the case of this research. In practice, a number of approximations or omissions often have to be made. In the case of classical DFT, temperature is not a tunable parameter, as calculations are carried out at 0 K, and the exchange-correlation functional is unknown and has to be approximated. Success has been found in taking into account temperature with the density functional theory-molecular dynamics (DFT-MD), although it neglects the explicit temperature dependence of electron-electron interactions [204]. In regard to exchange-correlation functionals, recent advances have been seen thanks to the development of exchange-correlation functionals assisted by machine learning [205]. Although promising, such an approach remains severely limited by the scarcity and heterogeneity of appropriate experimental data to “train” such machine learning algorithms [206]. A more classical strategy, common to the DFT scientific community, is to climb Jacob’s Ladder [207] of density-functional theory. On the top (fifth) rung, the information of the unoccupied Kohn–Sham orbitals is included in the exchange-correlation functional, which is expected to bring higher accuracy with a broader applicability. Two recently developed types of fifth rung density functional approximations are the random-phase approximation and the doubly-hybrid approximation [208]. These have limitations in terms of the so-called self-interaction error and non-dynamic correlation error, on top of the high computational cost. These exchange-correlation functionals have not yet been tested on the strongly correlated systems presented in this research and such an implementation deserves further investigation.

Another lesson and recurring theme present throughout this work is the essence of effective collaboration across disciplines and research approaches. Experimental research in chemistry and computational physics complement each other, as our theoretical knowledge can be exploited via computational approaches and validated through experimental results. For instance, the progress towards achieving the S=2 Haldane phase has been a direct result of effective experimental and computational collaboration.

In a broader context, it can be concluded that this work fine-tuned many of the DFT based approaches in studying quantum materials, and results brought us one step closer in understanding the nature of such materials. While the DFT+U studies presented here have deepened our understanding of the family of $MCl_2(pym)$ (where M = metal), as well as barlowite and its derivatives, there is still much room for progress in this field of research. From altering these quantum materials to meet desirable characteristics to developing new ones based on them, the coming years should see great progress in this growing field of research.

References

[1] Nicholas R. Glavin, Pulickel M. Ajayan, and Swastik Kar. “Quantum Materials Manufacturing”. *Advanced Materials* 35.27 (July 2023), p. 2109892.

[2] Charles Ahn, Andrea Cavalleri, Antoine Georges, Sohrab Ismail-Beigi, Andrew J. Millis, and Jean-Marc Triscone. “Designing and controlling the properties of transition metal oxide quantum materials”. *Nat. Mater.* 20 (Nov. 2021), pp. 1462–1468.

[3] D. N. Basov, R. D. Averitt, and D. Hsieh. “Towards properties on demand in quantum materials”. *Nature Materials* 16 (Nov. 2017), pp. 1077–1088.

[4] Yurii A. Izyumov. “Hubbard model of strong correlations”. *Physics-Uspekhi* 38.4 (Apr. 1995), p. 385.

[5] Eva Pavarini. “Solving the strong-correlation problem in materials”. *La Rivista del Nuovo Cimento* 44.11 (July 2021).

[6] K. Andres, J. E. Graebner, and H. R. Ott. “$4f$-Virtual-Bound-State Formation in $CeAl_3$ at Low Temperatures”. *Physical Review Letters* 35.26 (Dec. 1975), pp. 1779–1782.

[7] Piers Coleman. “Heavy Fermions and the Kondo Lattice: a 21st Century Perspective”. *ArXiv e-prints* (Sept. 2015).

[8] G. R. Stewart, Z. Fisk, J. O. Willis, and J. L. Smith. “Possibility of Coexistence of Bulk Superconductivity and Spin Fluctuations in UPt_3”. *Physical Review Letters* 52.8 (Feb. 1984), pp. 679–682.

[9] Emilia Morosan, Douglas Natelson, Andriy H. Nevidomskyy, and Qimiao Si. “Strongly Correlated Materials”. *ArXiv e-prints* (Sept. 2013).

[10] S. Raghu, Xiao-Liang Qi, C. Honerkamp, and Shou-Cheng Zhang. “Topological Mott Insulators”. *Physical Review Letters* 100.15 (Apr. 2008), p. 156401.

[11] Olle Gunnarsson. *Alkali-doped Fullerides: Narrow-band Solids with Unusual Properties.* Singapore: World Scientific, 2004.

[12] E. Gorelov, M. Karolak, T. O. Wehling, F. Lechermann, A. I. Lichtenstein, and E. Pavarini. “Nature of the Mott Transition in Ca_2RuO_4”. *Physical Review Letters* 104.22 (June 2010), p. 226401.

[13] A. L. Companion and M. A. Komarynsky. “Crystal field splitting diagrams”. *Journal of Chemical Education* 41.5 (May 1964), p. 257.

[14] Claris Chan. “Electron Orbitals & Orbital Shapes”. *ChemTalk* (Feb. 2022). [Online; accessed 27 March 2023] www.chemistrytalk.org.

[15] M. Atanasov, C. A. Daul, and C. Rauzy. “A DFT Based Ligand Field Theory”. *Optical Spectra and Chemical Bonding in Inorganic Compounds.* Berlin, Germany: Springer, May 2004, pp. 97–125.

[16] Kliment I. Kugel’ and D. I. Khomskiĭ. “The Jahn-Teller effect and magnetism: transition metal”. *Soviet Physics Uspekhi* 25.4 (Apr. 1982), p. 231.

[17] Ralph G. Pearson. “Concerning Jahn-Teller Effects”. *Proceedings of the National Academy of Sciences* 72.6 (June 1975), pp. 2104–2106.

[18] V. Sechovský. “Magnetism in Solids: General Introduction”. *Encyclopedia of Materials: Science and Technology.* Walthm, MA, USA: Elsevier, Jan. 2001, pp. 5018–5032.

[19] Mathias Getzlaff. *Fundamentals of Magnetism.* Berlin, Germany: Springer, 2008.

[20] C. M. Hurd. “Varieties of magnetic order in solids”. *Contemporary Physics* 23.5 (Sept. 1982), pp. 469–493.

[21] M. Georgiev and H. Chamati. “Magnetic exchange in spin clusters”. *AIP Conference Proceedings* 2075.1 (Feb. 2019).

[22] Dian-Teng Chen, Jia Chen, Xiang-Guo Li, George Christou, Stephen Hill, Xiao-Guang Zhang, and Hai-Ping Cheng. “Long-Range Magnetic Exchange Pathways in Complex Clusters from First Principles”. *Journal of Physical Chemistry C* 125.20 (May 2021), pp. 11124–11131.

[23] Antonio Sergio Teixeira Pires. “The Heisenberg model”. *Theoretical Tools for Spin Models in Magnetic Systems.* Bristol, England, UK: IOP Publishing, Apr. 2021, pp. 1–1–1–16.

[24] Jacques Curély. “Magnetic Orbitals and Mechanisms of Exchange I. Direct Exchange”. *Monatshefte für Chemie / Chemical Monthly* 136.6 (June 2005), pp. 987–1011.

[25] Gwenhaël Duplaix-Rata, Boris Le Guennic, and Grégoire David. “Revisiting magnetic exchange couplings in heterodinuclear complexes through the decomposition method in KS-DFT”. *Physical Chemistry Chemical Physics* 25.20 (May 2023), pp. 14170–14178.

[26] Philip W. Anderson. “Theory of Magnetic Exchange Interactions:Exchange in Insulators and Semiconductors”. *Solid State Physics.* Vol. 14. Cambridge, MA, USA: Academic Press, Jan. 1963, pp. 99–214.

[27] Pascal Freund, Irena Senkovska, Bin Zheng, Volodymyr Bon, Beate Krause, Guillaume Maurin, and Stefan Kaskel. “The force of MOFs: the potential of switchable metal–organic frameworks as solvent stimulated actuators”. *Chem. Commun.* 56 (2020).

[28] Yoshinori Tokura, Masashi Kawasaki, and Naoto Nagaosa. “Emergent functions of quantum materials”. *Nat. Phys.* 13 (Nov. 2017), pp. 1056–1068.

[29] Nitin Samarth. “Quantum materials discovery from a synthesis perspective”. *Nat. Mater.* 16 (Nov. 2017), pp. 1068–1076.

[30] Robert Cava, Nathalie de Leon, and Weiwei Xie. “Introduction: Quantum Materials”. *Chemical Reviews* 121.5 (Mar. 2021), pp. 2777–2779.

[31] Vitezslav Benda. “Power semiconductors - State of art and future trends”. *AIP Conf. Proc.* 1337.1 (June 2011), pp. 16–24.

[32] M.R. Ibarra and J.M. De Teresa. “Colossal magnetoresistance in manganese oxide perovskites”. *Journal of Magnetism and Magnetic Materials* 177-181 (1998), pp. 846–849.

[33] Lucy Clark and Aly H. Abdeldaim. “Quantum Spin Liquids from a Materials Perspective”. *Annual Review of Materials Research* 51.1 (2021), pp. 495–519.

[34] Michael R. Norman. “The Challenge of Unconventional Superconductivity”. *Science* 332.6026 (Apr. 2011), pp. 196–200.

[35] Ruth H. Zadik, Yasuhiro Takabayashi, Gyöngyi Klupp, Ross H. Colman, Alexey Y. Ganin, Anton Potočnik, Peter Jeglič, Denis Arčon, Péter Matus, Katalin Kamarás, Yuichi Kasahara, Yoshihiro Iwasa, Andrew N. Fitch, Yasuo Ohishi, Gaston Garbarino, Kenichi Kato, Matthew J. Rosseinsky, and Kosmas Prassides. “Optimized unconventional superconductivity in a molecular Jahn-Teller metal”. *Sci. Adv.* 1.3 (Apr. 2015).

[36] Xiaoli Yan, Xi Su, Jian Chen, Chao Jin, and Long Chen. “Two-Dimensional Metal-Organic Frameworks Towards Spintronics”. *Angewandte Chemie International Edition* (May 2023).

[37] Xiaoyu Song, Jingjuan Liu, Ting Zhang, and Long Chen. “2D conductive metal-organic frameworks for electronics and spintronics”. *Sci. China: Chem.* 63.10 (Oct. 2020), pp. 1391–1401.

[38] Steven G. Louie, Yang-Hao Chan, Felipe H. da Jornada, Zhenglu Li, and Diana Y. Qiu. “Discovering and understanding materials through computation”. *Nature Materials* 20 (June 2021), pp. 728–735.

[39] Anubhav Jain, Yongwoo Shin, and Kristin A. Persson. “Computational predictions of energy materials using density functional theory”. *Nature Reviews Materials* 1.15004 (Jan. 2016), pp. 1–13.

[40] James E. Saal, Scott Kirklin, Muratahan Aykol, Bryce Meredig, and C. Wolverton. “Materials Design and Discovery with High-Throughput Density Functional Theory: The Open Quantum Materials Database (OQMD)”. *JOM* 65.11 (Nov. 2013), pp. 1501–1509.

[41] Stewart J. Clark, Matthew D. Segall, Chris J. Pickard, Phil J. Hasnip, Matt I. J. Probert, Keith Refson, and Mike C. Payne. “First principles methods using CASTEP”. *Zeitschrift für Kristallographie - Crystalline Materials* 220.5-6 (2005), pp. 567–570.

[42] Jorge Kohanoff. *Electronic Structure Calculations for Solids and Molecules: Theory and Computational Methods.* Cambridge, England, UK: Cambridge University Press, June 2006.

[43] H. Shull and G. G. Hall. “Atomic Units”. *Nature* 184 (Nov. 1959), pp. 1559–1560.

[44] A Rauk. *Orbital Interaction Theory of Organic Chemistry - Appendix A: Derivation of Hartree–Fock Theory.* John Wiley and Sons, Inc., 2001.

[45] Richard M. Martin. *Electronic Structure: Basic Theory and Practical Methods.* Cambridge, England, UK: Cambridge University Press, Apr. 2004.

[46] Klaus Capelle. “A bird’s-eye view of density-functional theory”. *ArXiv e-prints* (Nov. 2002).

[47] P. Hohenberg and W. Kohn. “Inhomogeneous Electron Gas”. *Physical Review* 136.3B (Nov. 1964), B864–B871.

[48] W. Kohn and L. J. Sham. “Self-Consistent Equations Including Exchange and Correlation Effects”. *Physical Review* 140.4A (Nov. 1965), A1133–A1138.

[49] R. W. Godby, M. Schlüter, and L. J. Sham. “Trends in self-energy operators and their corresponding exchange-correlation potentials”. *Physical Review B* 36.12 (Oct. 1987), pp. 6497–6500.

[50] Xuejun Zhu and Steven G. Louie. “Variational quantum Monte Carlo study of two-dimensional Wigner crystals: Exchange, correlation, and magnetic-field effects”. *Physical Review B* 52.8 (Aug. 1995), pp. 5863–5884.

[51] John P. Perdew, Kieron Burke, and Matthias Ernzerhof. “Generalized Gradient Approximation Made Simple”. *Physical Review Letters* 77.18 (Oct. 1996), pp. 3865–3868.

[52] Rodney J. Bartlett, Ireneusz Grabowski, So Hirata, and Stanislav Ivanov. “The exchange-correlation potential in ab initio density functional theory”. *Journal of Chemical Physics* 122.3 (Jan. 2005).

[53] Yan Zhao, Nathan E. Schultz, and D. G. Truhlar. “Exchange-correlation functional with broad accuracy for metallic and nonmetallic compounds, kinetics, and noncovalent interactions”. *Journal of Chemical Physics* 123.16 (Oct. 2005).

[54] Eric J. Bylaska. “Plane-Wave DFT Methods for Chemistry”. *Annual Reports in Computational Chemistry.* Vol. 13. Walthm, MA, USA: Elsevier, Jan. 2017, pp. 185–228.

[55] Felix Bloch. “Über die Quantenmechanik der Elektronen in Kristallgittern”. *Zeitschrift für Physik* 52.7 (July 1929), pp. 555–600.

[56] Teguh Budi Prayitno and Fumiyuki Ishii. "Implementation of Generalized Bloch Theorem Using Linear Combination of Pseudo-Atomic Orbitals". *Journal of the Physical Society of Japan* 87.11 (Oct. 2018), p. 114709.

[57] Edvin Fako. "Pseudopotential representing the effective core charge". *Wikimedia Commons, the free media repository.* (2020). [Online; accessed 10 May 2023] www.commons.wikimedia.org/wiki/File:Pseudopotential.png.

[58] Waldemar Hujo and Stefan Grimme. "Performance of Non-Local and Atom-Pairwise Dispersion Corrections to DFT for Structural Parameters of Molecules with Noncovalent Interactions". *Journal of Chemical Theory and Computation* 9.1 (Jan. 2013), pp. 308–315.

[59] Michael E. Foster and Karl Sohlberg. "Empirically corrected DFT and semi-empirical methods for non-bonding interactions". *Physical Chemistry Chemical Physics* 12.2 (2010), pp. 307–322.

[60] Axel D. Becke and Erin R. Johnson. "Exchange-hole dipole moment and the dispersion interaction". *Journal of Chemical Physics* 122.15 (Apr. 2005), p. 154104.

[61] Tomáš Bučko, S. Lebègue, Jürgen Hafner, and J. G. Ángyán. "Tkatchenko-Scheffler van der Waals correction method with and without self-consistent screening applied to solids". *Physical Review B* 87.6 (Feb. 2013).

[62] Piyush Agrawal, Alexandre Tkatchenko, and Leeor Kronik. "Pair-Wise and Many-Body Dispersive Interactions Coupled to an Optimally Tuned Range-Separated Hybrid Functional". *Journal of Chemical Theory and Computation* 9.8 (Aug. 2013), pp. 3473–3478.

[63] Tomáš Bučko, Sébastien Lebègue, Tim Gould, and János G. Ángyán. "Many-body dispersion corrections for periodic systems: an efficient reciprocal space implementation". *Journal of Physics: Condensed Matter* 28.4 (Jan. 2016), p. 045201.

[64] Alberto Ambrosetti, Anthony M. Reilly, Robert A. DiStasio, and Alexandre Tkatchenko. "Long-range correlation energy calculated from coupled atomic response functions". *Journal of Chemical Physics* 140.18 (May 2014).

[65] Alexandre Tkatchenko, Robert A. DiStasio, Roberto Car, and Matthias Scheffler. "Accurate and Efficient Method for Many-Body van der Waals Interactions". *Physical Review Letters* 108.23 (June 2012).

[66] Alexandre Tkatchenko and Matthias Scheffler. "Accurate Molecular Van Der Waals Interactions from Ground-State Electron Density and Free-Atom Reference Data". *Physical Review Letters* 102.7 (Feb. 2009).

[67] Leeor Kronik and Alexandre Tkatchenko. "Understanding Molecular Crystals with Dispersion-Inclusive Density Functional Theory: Pairwise Corrections and Beyond". *Accounts of Chemical Research* 47.11 (Nov. 2014), pp. 3208–3216.

[68] Won June Kim, Minho Kim, Eok Kyun Lee, Sébastien Lebègue, and Hyungjun Kim. "Failure of Density Functional Dispersion Correction in Metallic Systems and Its Possible Solution Using a Modified Many-Body Dispersion Correction". *Journal of Physical Chemistry Letters* 7.16 (Aug. 2016), pp. 3278–3283.

[69] G. Kresse and J. Furthmüller. "Efficient iterative schemes for ab initio total-energy calculations using a plane-wave basis set". *Physical Review B* 54.16 (Oct. 1996), pp. 11169–11186.

[70] P. H. Dederichs and R. Zeller. "Self-consistency iterations in electronic-structure calculations". *Physical Review B* 28.10 (Nov. 1983), pp. 5462–5472.

[71] H. Akai and P. H. Dederichs. "A simple improved iteration scheme for electronic structure calculations". *Journal of Physics C: Solid State Physics* 18.12 (Apr. 1985), p. 2455.

[72] Broyden Charles. “A Class of Methods for Solving Nonlinear Simultaneous Equations”. *Mathematics of computation* 19.92 (Oct. 1965), pp. 577–593.

[73] Nicola Marzari, David Vanderbilt, and M. C. Payne. “Ensemble Density-Functional Theory for Ab Initio Molecular Dynamics of Metals and Finite-Temperature Insulators”. *Physical Review Letters* 79.7 (Aug. 1997), pp. 1337–1340.

[74] Gustavo Javier, Usama Kamran, David M. Guzman, Alejandro Strachan, Peilin Liao, and Robert Joseph Appleton. “DFT Material Properties Simulator”. *NanoHUB* (July 2015).

[75] Bernd G. Pfrommer, Michel Côté, Steven G. Louie, and Marvin L. Cohen. “Relaxation of Crystals with the Quasi-Newton Method”. *Journal of Computational Physics* 131.1 (Feb. 1997), pp. 233–240.

[76] M. I. J. Probert. “Improved algorithm for geometry optimisation using damped molecular dynamics”. *Journal of Computational Physics* 191.1 (Oct. 2003), pp. 130–146.

[77] David Packwood, James Kermode, Letif Mones, Noam Bernstein, John Woolley, Nicholas Gould, Christoph Ortner, and Gábor Csányi. “A universal preconditioner for simulating condensed phase materials”. *Journal of Chemical Physics* 144.16 (Apr. 2016).

[78] Paula Mori-Sánchez and Aron J. Cohen. “The derivative discontinuity of the exchange–correlation functional”. *Physical Chemistry Chemical Physics* 16.28 (June 2014), pp. 14378–14387.

[79] Andrew J. Morris, Rebecca J. Nicholls, Chris J. Pickard, and Jonathan R. Yates. “OptaDOS: A tool for obtaining density of states, core-level and optical spectra from electronic structure codes”. *Computer Physics Communications* 185.5 (May 2014), pp. 1477–1485.

[80] H. Eschrig, K. Koepernik, and I. Chaplygin. “Density functional application to strongly correlated electron systems”. *Journal of Solid State Chemistry* 176.2 (Dec. 2003), pp. 482–495.

[81] Daniel P. Arovas, Erez Berg, Steven A. Kivelson, and Srinivas Raghu. “The Hubbard Model”. *Annual Review of Condensed Matter Physics* 13.1 (Mar. 2022), pp. 239–274.

[82] Hal Tasaki. “The Hubbard model - an introduction and selected rigorous results”. *Journal of Physics: Condensed Matter* 10.20 (May 1998), p. 4353.

[83] Mingpu Qin, Thomas Schäfer, Sabine Andergassen, Philippe Corboz, and Emanuel Gull. “The Hubbard Model: A Computational Perspective”. *Annual Review of Condensed Matter Physics* 13.1 (Mar. 2022), pp. 275–302.

[84] J. E. Hirsch. “Two-dimensional Hubbard model: Numerical simulation study”. *Physical Review B* 31.7 (Apr. 1985), pp. 4403–4419.

[85] Eva Pavarini, Dieter Vollhardt, Erik Koch, and Alexander Lichtenstein. “The LDA+DMFT approach to strongly correlated materials”. *Forschungszenrum Jülich GmbH Zentralbibliothek, Verlag* (2011).

[86] B. H. Brandow. “Electronic structure of Mott insulators”. *Advances in Physics* (July 2006), pp. 651–808.

[87] Vladimir I. Anisimov, F. Aryasetiawan, and A. I. Lichtenstein. “First-principles calculations of the electronic structure and spectra of strongly correlated systems: the LDA+ U method”. *Journal of Physics: Condensed Matter* 9.4 (Jan. 1997), p. 767.

[88] Vladimir I. Anisimov, Jan Zaanen, and Ole K. Andersen. “Band theory and Mott insulators: Hubbard U instead of Stoner I”. *Physical Review B* 44.3 (July 1991), pp. 943–954.

[89] Volodymyr Turkowski, Alamgir Kabir, Neha Nayyar, and Talat S. Rahman. “Dynamical mean-field theory for molecules and nanostructures”. *Journal of Chemical Physics* 136.11 (Mar. 2012).

[90] Ryu Shinzaki, Joji Nasu, and Akihisa Koga. “DMFT Study for Valence Fluctuations in the Extended Periodic Anderson Model”. *Journal of Physics: Conference Series* 683.1 (Jan. 2016).

[91] Louis-François Arsenault, Alejandro Lopez-Bezanilla, O. Anatole von Lilienfeld, and Andrew J. Millis. “Machine learning for many-body physics: The case of the Anderson impurity model”. *Physical Review B* 90.15 (Oct. 2014), p. 155136.

[92] K. Held, I. A. Nekrasov, N. Blümer, V. I. Anisimov, and D. Vollhardt. “Realistic modelling of strongly correlated electron systems: an introduction to the LDA+DMFT approach”. *International Journal of Modern Physics B* 15 (Aug. 2001), pp. 2611–2625.

[93] Antoine Georges, Gabriel Kotliar, Werner Krauth, and Marcelo J. Rozenberg. “Dynamical mean-field theory of strongly correlated fermion systems and the limit of infinite dimensions”. *Reviews of Modern Physics* 68.1 (Jan. 1996), pp. 13–125.

[94] Gabriel Kotliar and Dieter Vollhardt. “Strongly Correlated Materials: Insights From Dynamical Mean-Field Theory”. *Physics Today* 57.3 (Mar. 2004), pp. 53–59.

[95] Dominika Zgid and Garnet Kin-Lic Chan. “Dynamical mean-field theory from a quantum chemical perspective”. *Journal of Chemical Physics* 134.9 (Mar. 2011).

[96] Daniel A. Rehn, John M. Wills, Torey E. Battelle, and Ann E. Mattsson. “Dirac’s equation and its implications for density functional theory based calculations of materials containing heavy elements”. *Physical Review. B* 101.8 (Feb. 2020).

[97] A. H. MacDonald and S. H. Vosko. “A relativistic density functional formalism”. *Journal of Physics C: Solid State Physics* 12.15 (Aug. 1979), p. 2977.

[98] A. K. Rajagopal. “Inhomogeneous relativistic electron gas”. *Journal of Physics C: Solid State Physics* 11.24 (Dec. 1978), p. L943.

[99] A. K. Rajagopal and J. Callaway. “Inhomogeneous Electron Gas”. *Physical Review B* 7.5 (Mar. 1973), pp. 1912–1919.

[100] Helena Reichlova, Tomas Janda, Joao Godinho, Anastasios Markou, Dominik Kriegner, Richard Schlitz, Jakub Zelezny, Zbynek Soban, Mauricio Bejarano, Helmut Schultheiss, Petr Nemec, Tomas Jungwirth, Claudia Felser, Joerg Wunderlich, and Sebastian T. B. Goennenwein. “Imaging and writing magnetic domains in the non-collinear antiferromagnet Mn3Sn”. *Nature Communications* 10.5459 (Nov. 2019), pp. 1–6.

[101] M.J. Rutter. “C2x: A tool for visualisation and input preparation for Castep and other electronic structure codes”. *Computer Physics Communications* 225 (2018), pp. 174–179.

[102] Anton Kokalj. “XCrySDen—a new program for displaying crystalline structures and electron densities”. *Journal of Molecular Graphics and Modelling* 17.3 (June 1999), pp. 176–179.

[103] S. Luther, M. von Ortenberg, J. Tuchendler, and J. P. Renard. “Magnetic resonances in the Haldane-gap materials NENP and NINO”. *Physica B: Condensed Matter* 211.1 (May 1995), pp. 213–216.

[104] Jem Pitcairn, Andrea Iliceto, Laura Cañadillas-Delgado, Oscar Fabelo, Cheng Liu, Christian Balz, Andreas Weilhard, Stephen P. Argent, Andrew J. Morris, and Matthew J. Cliffe. “Low-Dimensional Metal–Organic Magnets as a Route toward the S = 2 Haldane Phase”. *Journal of the American Chemical Society* 145.3 (Jan. 2023), pp. 1783–1792.

[105] Pimonpan Sompet, Sarah Hirthe, Dominik Bourgund, Thomas Chalopin, Julian Bibo, Joannis Koepsell, Petar Bojović, Ruben Verresen, Frank Pollmann, Guillaume Sa-

lomon, Christian Gross, Timon A. Hilker, and Immanuel Bloch. “Realizing the symmetry-protected Haldane phase in Fermi–Hubbard ladders”. *Nature* 606 (June 2022), pp. 484–488.

[106] K. V. Shanavas, Z. S. Popović, and S. Satpathy. “Theoretical model for Rashba spin-orbit interaction in d electrons”. *Physical Review B* 90.16 (Oct. 2014), p. 165108.

[107] Ryota Sakamoto, Naoya Fukui, Hiroaki Maeda, Ryojun Toyoda, Shinya Takaishi, Tappei Tanabe, Joe Komeda, Pilar Amo-Ochoa, Félix Zamora, and Hiroshi Nishihara. “Layered metal-organic frameworks and metal-organic nanosheets as functional materials”. *Coordination Chemistry Reviews* 472 (2022), p. 214787.

[108] Watcharaphol Paritmongkol. “Syntheses and Photophysical Studies of Two-Dimensional Hybrid Organic-Inorganic Semiconductors”. PhD thesis. Massachusetts Institute of Technology, Sept. 2021.

[109] Kasper S. Pedersen, Panagiota Perlepe, Michael L. Aubrey, Daniel N. Woodruff, Sebastian E. Reyes-Lillo, Anders Reinholdt, Laura Voigt, Zheshen Li, Kasper Borup, Mathieu Rouzières, Dumitru Samohvalov, Fabrice Wilhelm, Andrei Rogalev, Jeffrey B. Neaton, Jeffrey R. Long, and Rodolphe Clérac. “Formation of the layered conductive magnet CrCl2(pyrazine)2 through redox-active coordination chemistry”. *Nat. Chem.* 10 (Oct. 2018), pp. 1056–1061.

[110] Gang Xu, Teppei Yamada, Kazuya Otsubo, Shun Sakaida, and Hiroshi Kitagawa. “Facile “modular assembly” for fast construction of a highly oriented crystalline MOF nanofilm”. *Journal of the American Chemical Society* 134.40 (2012), pp. 16524–16527.

[111] Brian Andersen, Gregory Delipei, David Kropaczek, and Jason Hou. “MOF: A Modular Framework for Rapid Application of Optimization Methodologies to General Engineering Design Problems”. *arXiv* (Apr. 2022).

[112] Yifan Gu, Yi-nan Wu, Liangchun Li, Wei Chen, Fengting Li, and Susumu Kitagawa. "Controllable Modular Growth of Hierarchical MOF-on-MOF Architectures". *Angew. Chem.* 129.49 (Dec. 2017), pp. 15864–15868.

[113] K. Momma and F. Izumi. "VESTA: a three-dimensional visualization system for electronic and structural analysis". *Journal of Applied Crystallography* 41.3 (June 2008), pp. 653–658.

[114] D. R. Bowler and M. J. Gillan. "An efficient and robust technique for achieving self consistency in electronic structure calculations". *Chem. Phys. Lett.* 325.4 (July 2000), pp. 473–476.

[115] A. Stroppa and G. Kresse. "The shortcomings of semi-local and hybrid functionals: what we can learn from surface science studies". *New J. Phys.* 10.6 (June 2008).

[116] Pedro Borlido, Thorsten Aull, Ahmad W Huran, Fabien Tran, Miguel A L Marques, and Silvana Botti. "Large-Scale Benchmark of Exchange-Correlation Functionals for the Determination of Electronic Band Gaps of Solids". *Journal of chemical theory and computation* 15.9 (Sept. 2019), 5069—5079.

[117] Noemí Hernández-Haro, Joaquín Ortega-Castro, Yaroslav B. Martynov, Rashid G. Nazmitdinov, and Antonio Frontera. "DFT prediction of band gap in organic-inorganic metal halide perovskites: An exchange-correlation functional benchmark study". *Chem. Phys.* 516 (Jan. 2019), pp. 225–231.

[118] Daniel Tunega, Tomáš Bučko, and Ali Zaoui. "Assessment of ten DFT methods in predicting structures of sheet silicates: Importance of dispersion corrections". *J. Chem. Phys.* 137.11 (Sept. 2012), p. 114105.

[119] Stefan Grimme, Jens Antony, Stephan Ehrlich, and Helge Krieg. "A consistent and accurate ab initio parametrization of density functional dispersion correction (DFT-D) for the 94 elements H-Pu". *J. Chem. Phys.* 132.15 (Apr. 2010).

[120] J. Ulises Reveles and Andreas M. Köster. “Geometry optimization in density functional methods”. *J. Comput. Chem.* 25.9 (July 2004), pp. 1109–1116.

[121] M. D. Segall, Philip J. D. Lindan, M. J. Probert, C. J. Pickard, P. J. Hasnip, S. J. Clark, and M. C. Payne. “First-principles simulation: ideas, illustrations and the CASTEP code”. *J. Phys.: Condens. Matter* 14.11 (Mar. 2002), pp. 2717–2744.

[122] M. D. Sturge. “The Jahn-Teller Effect in Solids”. *Solid State Physics.* Vol. 20. Cambridge, MA, USA: Academic Press, Jan. 1968, pp. 91–211.

[123] Burak Himmetoglu, Andrea Floris, Stefano de Gironcoli, and Matteo Cococcioni. “Hubbard-corrected DFT energy functionals: The LDA+U description of correlated systems”. *Int. J. Quantum Chem.* 114.1 (Jan. 2014), pp. 14–49.

[124] Sara R. Mortensen and Kasper P. Kepp. “Spin Propensities of Octahedral Complexes From Density Functional Theory”. *J. Phys. Chem. A* 119.17 (Apr. 2015), pp. 4041–4050.

[125] Aaram J. Kim, Fedor Simkovic, and Evgeny Kozik. “Spin and Charge Correlations across the Metal-to-Insulator Crossover in the Half-Filled 2D Hubbard Model”. *Physical Review Letters* 124.11 (Mar. 2020).

[126] Rebekka Tesch and Piotr M. Kowalski. “Hubbard U parameters for transition metals from first principles”. *Phys. Rev. B* 105.19 (May 2022), p. 195153.

[127] Joo Rhee and Nirpendra Singh. “Electronic Structures and Optical Properties of Spinel ZnCr2O4”. *J. Korean Phys. Soc.* 57.5 (2010), pp. 1233–1237.

[128] Lei Wang, Thomas Maxisch, and Gerbrand Ceder. “Oxidation energies of transition metal oxides within the GGA + U framework”. *Phys. Rev. B* 73 (19 May 2006), p. 195107.

[129] John T. Vallin and George D. Watkins. “The Jahn-teller effect for Cr2+ in II–VI crystals”. *Solid State Commun.* 9.13 (July 1971), pp. 953–956.

[130] Malcolm A. Halcrow. "Jahn–Teller distortions in transition metal compounds, and their importance in functional molecular and inorganic materials". *Chem. Soc. Rev.* 42.4 (2013), pp. 1784–1795.

[131] Jonas Börgel, Michael G. Campbell, and Tobias Ritter. "Transition Metal d-Orbital Splitting Diagrams: An Updated Educational Resource for Square Planar Transition Metal Complexes". *J. Chem. Educ.* 93.1 (Jan. 2016), pp. 118–121.

[132] Mihail Atanasov, Dmitry Ganyushin, Kantharuban Sivalingam, and Frank Neese. "A Modern First-Principles View on Ligand Field Theory Through the Eyes of Correlated Multireference Wavefunctions". *Molecular Electronic Structures of Transition Metal Complexes II.* Berlin, Germany: Springer, Nov. 2011, pp. 149–220.

[133] Nick Woods, Michael Payne, and Phil Hasnip. "The Self-Consistent Field in Kohn-Sham Density Functional Theory: A Review of Methods and Algorithms". *APS March Meeting Abstracts* 2019 (2019), S18.010.

[134] Yoyo Hinuma, Giovanni Pizzi, Yu Kumagai, Fumiyasu Oba, and Isao Tanaka. "Band structure diagram paths based on crystallography". *Computational Materials Science* 128 (Feb. 2017), pp. 140–184.

[135] Aliaksandr V. Krukau, Oleg A. Vydrov, Artur F. Izmaylov, and Gustavo E. Scuseria. "Influence of the exchange screening parameter on the performance of screened hybrid functionals". *Journal of Chemical Physics* 125.22 (Dec. 2006).

[136] R. C. Albers, N. E. Christensen, and A. Svane. "Hubbard-U". *J. Phys.: Condens. Matter* 21.34 (Aug. 2009), p. 343201.

[137] V. P. Amin, Junwen Li, M. D. Stiles, and P. M. Haney. "Intrinsic spin currents in ferromagnets". *Phys. Rev. B* 99.22 (June 2019), p. 220405.

[138] Wei Han, Sadamichi Maekawa, and Xin-Cheng Xie. "Spin current as a probe of quantum materials". *Nat. Mater.* 19 (Feb. 2020), pp. 139–152.

[139] E. B. Sonin. “Spin currents and spin superfluidity”. *Adv. Phys.* 59.3 (May 2010), pp. 181–255.

[140] P. W. Anderson. “New Approach to the Theory of Superexchange Interactions”. *Phys. Rev.* 115.1 (July 1959), pp. 2–13.

[141] Junjiro Kanamori. “Superexchange interaction and symmetry properties of electron orbitals”. *J. Phys. Chem. Solids* 10.2 (July 1959), pp. 87–98.

[142] Martin Indergand and Manfred Sigrist. “Existence of Long-Range Magnetic Order in the Ground State of Two-Dimensional Spin-1/2 Heisenberg Antiferromagnets”. *Progress of Theoretical Physics* 117 (Jan. 2007), pp. 1–15.

[143] J. Zaanen and G. A. Sawatzky. “The electronic structure and superexchange interactions in transition-metal compounds”. *Can. J. Phys.* (Feb. 2011).

[144] Raymond F. Bishop, Damian J. J. Farnell, and John B. Parkinson. “Phase transitions in the spin-half$J_1 - - J_2$ Model”. *Physical Review B* 58.10 (Sept. 1998), pp. 6394–6402.

[145] Luciano Loris Viteritti, Francesco Ferrari, and Federico Becca. “Accuracy of restricted Boltzmann machines for the one-dimensional $J_1 - J_2$ Heisenberg model”. *SciPost Phys.* 12 (2022), p. 166.

[146] J. W. Moskowitz and M. P. Barnett. “Pi Electronic Structure of the Benzene Molecule”. *J. Chem. Phys.* 39.6 (Sept. 1963), pp. 1557–1560.

[147] B. Keimer and J. E. Moore. “The physics of quantum materials”. *Nat. Phys.* 13 (Nov. 2017), pp. 1045–1055.

[148] M. B. Stone, G. Ehlers, and G. E. Granroth. “$S = 2$ quasi-one-dimensional spin waves in $CrCl_2$”. *Phys. Rev. B* 88 (10 Sept. 2013), p. 104413.

[149] C. Broholm, R. J. Cava, S. A. Kivelson, D. G. Nocera, M. R. Norman, and T. Senthil. “Quantum spin liquids”. *Science* 367.6475 (Jan. 2020).

[150] Rebecca W. Smaha, Wei He, Jack Mingde Jiang, Jiajia Wen, Yi-Fan Jiang, John P. Sheckelton, Charles J. Titus, Suyin Grass Wang, Yu-Sheng Chen, Simon J. Teat, Adam A. Aczel, Yang Zhao, Guangyong Xu, Jeffrey W. Lynn, Hong-Chen Jiang, and Young S. Lee. “Materializing rival ground states in the barlowite family of kagome magnets: quantum spin liquid, spin ordered, and valence bond crystal states”. *npj Quantum Materials* 5.23 (Apr. 2020), pp. 1–11.

[151] Daniel Grohol and Daniel G. Nocera. “Magnetic Disorder in the Frustrated Antiferromagnet Jarosite Arising from the H3O+···OH- Interaction”. *Chemistry of Materials* 19.12 (June 2007), pp. 3061–3066.

[152] P. Mendels, F. Bert, M. A. de Vries, A. Olariu, A. Harrison, F. Duc, J. C. Trombe, J. S. Lord, A. Amato, and C. Baines. “Quantum Magnetism in the Paratacamite Family: Towards an Ideal Kagom\'e Lattice”. *Physical Review Letters* 98.7 (Feb. 2007).

[153] Leon Balents. “Spin liquids in frustrated magnets”. *Nature* 464 (Mar. 2010), pp. 199–208.

[154] Juan R. Chamorro, Tyrel M. McQueen, and Thao T. Tran. “Chemistry of Quantum Spin Liquids”. *Chemical Reviews* 121.5 (Mar. 2021), pp. 2898–2934.

[155] V. A. Ivanov, T. G. Aminov, V. M. Novotortsev, and V. T. Kalinnikov. “Spintronics and spintronics materials”. *Russian Chemical Bulletin* 53.11 (Nov. 2004), pp. 2357–2405.

[156] Wataru Koshibae, Yoshio Kaneko, Junichi Iwasaki, Masashi Kawasaki, Yoshinori Tokura, and Naoto Nagaosa. “Memory functions of magnetic skyrmions”. *Japanese Journal of Applied Physics* 54.5 (Apr. 2015).

[157] Rebecca W. Smaha, Jonathan Pelliciari, Ignace Jarrige, Valentina Bisogni, Aaron T. Breidenbach, Jack Mingde Jiang, Jiajia Wen, Hong-Chen Jiang, and Young S. Lee. “High-energy spin excitations in the quantum spin liquid candidate Zn-substituted

barlowite probed by resonant inelastic x-ray scattering". *Physical Review B* 107.6 (Feb. 2023), p. L060402.

[158] M. R. Norman. "Colloquium: Herbertsmithite and the search for the quantum spin liquid". *Reviews of Modern Physics* 88.4 (Dec. 2016).

[159] Katherine Tustain, Emma E. McCabe, Angel M. Arevalo-Lopez, Alexandra S. Gibbs, Stephen P. Thompson, Claire A. Murray, Clemens Ritter, and Lucy Clark. "Disorder-Induced Structural Complexity in the Barlowite Family of $S = 1/2$ Kagomé Magnets". *Chemistry of Materials* 33.24 (Dec. 2021), pp. 9638–9651.

[160] Alyssa Henderson, Lianyang Dong, Sananda Biswas, Hannah I. Revell, Yan Xin, Roser Valenti, John A. Schlueter, and Theo Siegrist. "Order–disorder transition in the $S = \frac{1}{2}$ kagome antiferromagnets claringbullite and barlowite". *Chemical Communications* 55.77 (Sept. 2019), pp. 11587–11590.

[161] Rebecca W. Smaha, Wei He, John P. Sheckelton, Jiajia Wen, and Young S. Lee. "Synthesis-dependent properties of barlowite and Zn-substituted barlowite". *Journal of Solid State Chemistry* 268 (Dec. 2018), pp. 123–129.

[162] C. M. Pasco, B. A. Trump, Thao T. Tran, Z. A. Kelly, C. Hoffmann, I. Heinmaa, R. Stern, and T. M. McQueen. "Single-crystal growth of $Cu_4(OH)_6BrF$ and universal behavior in quantum spin liquid candidates synthetic barlowite and herbertsmithite". *Physical Review Materials* 2.4 (Apr. 2018).

[163] Harald O. Jeschke, Francesc Salvat-Pujol, Elena Gati, Nguyen Hieu Hoang, Bernd Wolf, Michael Lang, John A. Schlueter, and Roser Valentí. "Barlowite as a canted antiferromagnet: Theory and experiment". *Physical Review B* 92.9 (Sept. 2015).

[164] Stephan Lany and Alex Zunger. "Polaronic hole localization and multiple hole binding of acceptors in oxide wide-gap semiconductors". *Physical Review B* 80.8 (Aug. 2009).

[165] Stefano Falletta and Alfredo Pasquarello. “Hubbard U through polaronic defect states”. *npj Computational Materials* 8.263 (Dec. 2022), pp. 1–8.

[166] Qihang Liu, Qiushi Yao, Z. A. Kelly, C. M. Pasco, T. M. McQueen, S. Lany, and Alex Zunger. “Electron Doping of Proposed Kagome Quantum Spin Liquid Produces Localized States in the Band Gap”. *Physical Review Letters* 121.18 (Oct. 2018).

[167] S. L. Dudarev, G. A. Botton, S. Y. Savrasov, C. J. Humphreys, and A. P. Sutton. “Electron-energy-loss spectra and the structural stability of nickel oxide: An LSDA+U study”. *Physical Review B* 57.3 (Jan. 1998), pp. 1505–1509.

[168] Patrick A. Lee. “From high temperature supercondutivity to quantum spin liquid: progress in strong correlation physics”. *ArXiv e-prints* (Aug. 2007).

[169] J. Bardeen, L. N. Cooper, and J. R. Schrieffer. “Theory of Superconductivity”. *Physical Review* 108.5 (Dec. 1957), pp. 1175–1204.

[170] Xingjiang Zhou, Wei-Sheng Lee, Masatoshi Imada, Nandini Trivedi, Philip Phillips, Hae-Young Kee, Päivi Törmä, and Mikhail Eremets. “High-temperature superconductivity”. *Nature Reviews Physics* 3 (July 2021), pp. 462–465.

[171] Hong-Chen Jiang. “Superconductivity in the doped quantum spin liquid on the triangular lattice”. *npj Quantum Materials* 6.71 (Aug. 2021), pp. 1–7.

[172] Ya-Ting Jia, Chun-Sheng Gong, Yi-Xuan Liu, Jian-Fa Zhao, Cheng Dong, Guang-Yang Dai, Xiao-Dong Li, He-Chang Lei, Run-Ze Yu, Guang-Ming Zhang, and Chang-Qing Jin. “Mott Transition and Superconductivity in Quantum Spin Liquid Candidate NaYbSe2”. *Chinese Physics Letters* 37.9 (Sept. 2020).

[173] Zheng Liu, Xiaolong Zou, Jia-Wei Mei, and Feng Liu. “Selective doping Barlowite for quantum spin liquid: a first-principles study”. *ArXiv e-prints* (Apr. 2015).

[174] William P. Huhn and Volker Blum. “One-hundred-three compound band-structure benchmark of post-self-consistent spin-orbit coupling treatments in density functional theory”. *Physical Review Materials* 1.3 (Aug. 2017).

[175] Domenico Di Sante, Chiara Bigi, Philipp Eck, Stefan Enzner, Armando Consiglio, Ganesh Pokharel, Pietro Carrara, Pasquale Orgiani, Vincent Polewczyk, Jun Fujii, Phil D. C. King, Ivana Vobornik, Giorgio Rossi, Ilija Zeljkovic, Stephen D. Wilson, Ronny Thomale, Giorgio Sangiovanni, Giancarlo Panaccione, and Federico Mazzola. “Flat band separation and robust spin Berry curvature in bilayer kagome metals”. *Nature Physics* (May 2023), pp. 1–8.

[176] Robert A. Lawrence, Scott J. Donaldson, and Matt I. J. Probert. “Magnetic Transition State Searching: Beyond the Static Ion Approximation”. *Magnetochemistry* 9.2 (Jan. 2023), p. 42.

[177] Galo A. Torres Sevilla and Muhammad M. Hussain. “Printed Organic and Inorganic Electronics: Devices To Systems”. *IEEE Journal on Emerging and Selected Topics in Circuits and Systems* 7.1 (2017), pp. 147–160.

[178] Uxua Huizi Rayo. “Design, synthesis and characterization of multifuncional MOFs. From gas absorption and photocatalysis to ciss effect and spin-currents.” PhD thesis. Massachusetts Institute of Technology, Dec. 2020.

[179] Hitoshi Miyasaka. “Charge Manipulation in Metal–Organic Frameworks: Toward Designer Functional Molecular Materials”. *Bull. Chem. Soc. Jpn.* (Sept. 2021).

[180] Marius Fuchs, Peitao Liu, Tilman Schwemmer, Giorgio Sangiovanni, Ronny Thomale, Cesare Franchini, and Domenico Di Sante. “Kagome metal-organic frameworks as a platform for strongly correlated electrons”. *Journal of Physics: Materials* 3.2 (Feb. 2020).

[181] Claire Ashworth. “Metal–organic frameworks: Molten MOFs”. *Nat. Rev. Mater.* 2.17074 (Oct. 2017), p. 1.

[182] Wen-Xia Fang, Shu-Hua Ma, Hui Dong, Xiao-Wei Jin, Ya-Chen Zou, Ke-Xin Xu, Lan Zhang, and Yang-Hui Luo. “Squarelike AgCl Nanoparticles Grown Using NiCl2(Pyz)2-Based Metal–Organic Framework Nanosheet Templates for Antibacterial Applications”. *ACS Appl. Nano Mater.* 4.5 (May 2021), pp. 5541–5547.

[183] Gregory W. Mann, Kyuho Lee, Matteo Cococcioni, Berend Smit, and Jeffrey B. Neaton. “First-principles Hubbard U approach for small molecule binding in metal-organic frameworks”. *Journal of Chemical Physics* 144.17 (May 2016).

[184] Sarah A. Tolba, Kareem M. Gameel, Basant A. Ali, A. Hossam, and Nageh K. Allam. “The DFT+U: Approaches, Accuracy, and Applications”. *Density Functional Calculations - Recent Progresses of Theory and Application.* IntechOpen, May 2018.

[185] Heather J. Kulik, Matteo Cococcioni, Damian A. Scherlis, and Nicola Marzari. “Density Functional Theory in Transition-Metal Chemistry: A Self-Consistent Hubbard U Approach”. *Physical Review Letters* 97.10 (Sept. 2006).

[186] Archa Gulati and Rita Kakkar. “DFT studies on storage and adsorption capacities of gases on MOFs”. *Physical Sciences Reviews* 3.8 (Aug. 2018).

[187] Nicole E. Kirchner-Hall, Wayne Zhao, Yihuang Xiong, Iurii Timrov, and Ismaila Dabo. “Extensive Benchmarking of DFT+U Calculations for Predicting Band Gaps”. *Applied Sciences* 11.5 (Mar. 2021), p. 2395.

[188] Heather J. Kulik. “Perspective: Treating electron over-delocalization with the DFT+U method”. *Journal of Chemical Physics* 142.24 (June 2015).

[189] Aasif Helal, Syed Shaheen Shah, Muhammad Usman, Mohd Yusuf Khan, Md. Abdul Aziz, and Mohammad Mizanur Rahman. “Potential Applications of Nickel-Based Metal-Organic Frameworks and their Derivatives”. *Chemical Record* 22.7 (July 2022).

[190] Xiaoyang Xuan, Min Qian, Likun Pan, Ting Lu, Lu Han, Huangze Yu, Lijia Wan, Yueping Niu, and Shangqing Gong. “A longitudinally expanded Ni-based metal–organic framework with enhanced double nickel cation catalysis reaction channels for a non-enzymatic sweat glucose biosensor”. *Journal of Materials Chemistry B* 8.39 (Oct. 2020), pp. 9094–9109.

[191] Aasif Helal, Mohammed Fettouhi, Md. Eyasin Arafat, Mohd Yusuf Khan, and Mohammed Ahmed Sanhoob. “Nickel based metal-organic framework as catalyst for chemical fixation of CO2 in oxazolidinone synthesis”. *Journal of CO2 Utilization* 50 (Aug. 2021), p. 101603.

[192] Zhao Qin, Yanqin Xu, Lin Liu, Min Liu, Hanjun Zhou, Liyue Xiao, Yuan Cao, and Changguo Chen. “Ni-MOF composite polypyrrole applied to supercapacitor energy storage”. *RSC Advances* 12.45 (Oct. 2022), pp. 29177–29186.

[193] Marcin M. Wysokiński. “Mechanism for transitions between ferromagnetic and antiferromagnetic orders in d-electron metallic magnets”. *Scientific Reports* 9.19461 (Dec. 2019), pp. 1–8.

[194] Wenchang Yin, Cheng-an Tao, Fang Wang, Jian Huang, Tianliang Qu, and Jianfang Wang. “Tuning optical properties of MOF-based thin films by changing the ligands of MOFs”. *Science China Materials* 61.3 (2018).

[195] Seyed Mohamad Moosavi, Aditya Nandy, Kevin Maik Jablonka, Daniele Ongari, Jon Paul Janet, Peter G. Boyd, Yongjin Lee, Berend Smit, and Heather J. Kulik. “Understanding the diversity of the metal-organic framework ecosystem”. *Nature Communications* 11.4068 (Aug. 2020), pp. 1–10.

[196] Jie Li and Ruqian Wu. “Metal–organic frameworks: possible new two-dimensional magnetic and topological materials”. *Nanoscale* 12.46 (Dec. 2020), pp. 23620–23625.

[197] Chris J. Pickard and R. J. Needs. “Ab initio random structure searching”. *Journal of Physics: Condensed Matter* 23.5 (Jan. 2011).

[198] C. R. Groom, I. J. Bruno, M. P. Lightfoot, and S. C. Ward. “The Cambridge Structural Database”. *Acta Crystallographica Section B: Structural Science, Crystal Engineering and Materials* 72.2 (Apr. 2016), pp. 171–179.

[199] James P. Darby, Mihails Arhangelskis, Athanassios D. Katsenis, Joseph M. Marrett, Tomislav Friščić, and Andrew J. Morris. “Ab Initio Prediction of Metal-Organic Framework Structures”. *Chemistry of Materials* 32.13 (July 2020), pp. 5835–5844.

[200] Wenxian Liu, Ruilian Yin, Xilian Xu, Lin Zhang, Wenhui Shi, and Xiehong Cao. “Structural Engineering of Low-Dimensional Metal–Organic Frameworks: Synthesis, Properties, and Applications”. *Advanced Science* 6.12 (June 2019), p. 1802373.

[201] Kebin Li, Yihong Wu, Zaibing Guo, Yuankai Zheng, Guchang Han, Jinjun Qiu, Ping Luo, Lihua An, and Tiejun Zhou. “Exchange Coupling and Its Applications in Magnetic Data Storage”. *ChemInform* 38.35 (Aug. 2007).

[202] Qin Yu and Dong Wang. “Room-temperature magnetism in two-dimensional metal–organic frameworks enabled by electrostatic gating”. *Journal of Materials Chemistry A* 11.11 (Mar. 2023), pp. 5548–5558.

[203] A. de la Torre, B. Zager, F. Bahrami, M. H. Upton, J. Kim, G. Fabbris, G.-H. Lee, W. Yang, D. Haskel, F. Tafti, and K. W. Plumb. “Momentum-independent magnetic excitation continuum in the honeycomb iridate H3LiIr2O6”. *Nature Communications* 14.5018 (Aug. 2023), pp. 1–8.

[204] Aurora Pribram-Jones. “Thermal Density Functional Theory, Ensemble Density Functional Theory, and Potential Functional Theory for Warm Dense Matter”. *UC Irvine* (2015).

[205] Ryo Nagai and Ryosuke Akashi. “Development of exchange-correlation functionals assisted by machine learning”. *ArXiv e-prints* (June 2022).

[206] M. F. Kasim and S. M. Vinko. “Learning the Exchange-Correlation Functional from Nature with Fully Differentiable Density Functional Theory”. *Physical Review Letters* 127.12 (Sept. 2021), p. 126403.

[207] John P. Perdew and Karla Schmidt. “Jacob’s ladder of density functional approximations for the exchange-correlation energy”. *AIP Conference Proceedings* 577.1 (July 2001), pp. 1–20.

[208] Igor Ying Zhang and Xin Xu. “On the top rung of Jacob’s ladder of density functional theory: Toward resolving the dilemma of SIE and NCE”. *Wiley Interdisciplinary Reviews: Computational Molecular Science* 11.1 (June 2020), e1490.

[209] Wahyu Setyawan and Stefano Curtarolo. “High-throughput electronic band structure calculations: Challenges and tools”. *Comput. Mater. Sci.* 49.2 (Aug. 2010), pp. 299–312.

[210] Juan E. Peralta, Jochen Heyd, Gustavo E. Scuseria, and Richard L. Martin. “Spin-orbit splittings and energy band gaps calculated with the Heyd-Scuseria-Ernzerhof screened hybrid functional”. *Phys. Rev. B* 74.7 (Aug. 2006).

[211] Vinod Ashokan, B. D. Indu, and A. Kr. Dimri. “Signature of electron-phonon interaction in high temperature superconductors”. *AIP Adv.* 1.3 (Sept. 2011).

[212] Jiaji Ma, Ruihan Yang, and Hanghui Chen. “A large modulation of electron-phonon coupling and an emergent superconducting dome in doped strong ferroelectrics”. *Nat. Commun.* 12.2314 (Apr. 2021), pp. 1–9.

[213] R. E. Cohen. “Electrons, Phonons, and Electron-Phonon Interactions in High-Temperature Superconductors”. *Comput. Phys.* 8.1 (Jan. 1994), pp. 34–44.

[214] Dirk van Delft and Peter Kes. “The discovery of superconductivity”. *Phys. Today* 63.9 (Sept. 2010), p. 38.

[215] M. C. Payne, M. P. Teter, D. C. Allan, T. A. Arias, and J. D. Joannopoulos. “Iterative minimization techniques for ab initio total-energy calculations: molecular dynamics and conjugate gradients”. *Reviews of Modern Physics* 64.4 (Oct. 1992), pp. 1045–1097.

[216] Riccardo De Gennaro, Nicola Colonna, Edward Linscott, and Nicola Marzari. “Bloch’s theorem in orbital-density-dependent functionals: Band structures from Koopmans spectral functionals”. *Physical Review B* 106.3 (July 2022).

[217] Amartya S. Banerjee, Phanish Suryanarayana, and John E. Pask. “Periodic Pulay method for robust and efficient convergence acceleration of self-consistent field iterations”. *Chemical Physics Letters* 647 (Mar. 2016), pp. 31–35.